九州大学学術情報リポジトリ
Kyushu University Institutional Repository

Characteristic radius of circumplanetary disk and its dependence on planetary mass

波々伯部, 広隆

https://doi.org/10.15017/1931714

出版情報：九州大学, 2017, 博士（理学）, 課程博士
バージョン：
権利関係：

Characteristic radius of circumplanetary disk and its dependence on planetary mass

Hirotaka Hohokabe

Department of Earth and Planetary Sciences,
Graduate School of Science, Kyushu University

March 2018

Abstract

Circumplanetary disks around forming gas-giant planets are plausible and possible targets of future observations, and can unveil the formation of planets and their satellites. Three-dimensional hydrodynamic simulations with high spatial resolution are performed to investigate the spatial scale of the disks and the mass transfer near the forming planets. The numerical model has the following three assumptions: hydrostatic equilibrium in the vertical direction of a protoplanetary disk, isothermal equation of state, and the Keplerian rotation around the protostar. This model has only one parameter $\hat{r}_{\rm H}$, the non dimensional Hill radius, defined as the Hill radius divided by the scale height. A new sink method is implemented in a nested grid code, in which the mass at the center is removed in each time-step and the removed mass is determined in an analytical way. After the convergence of physical quantities is confirmed, a calculation is executed until the circumplanetary disk achieves a steady state. With many calculations, the radius of circumplanetary disks is precisely determined. I propose a fitting formula of the circumplanetary disk radius, which is approximately proportional to $\hat{r}_{\rm H}^{2.4}$. Turbulent motion dominates the rotational motion outside the region where the gas rotation velocity is less than 60 percent of the Keplerian velocity of the protoplanet. In addition, the physical quantities highly oscillate with time in such a turbulent region. Thus, the simulations imply the existence of a critical radius which corresponds to the boundary between a stable disk and a turbulent region. Adopting a standard protoplanetary disk model, I translate the non-dimensional quantities used in simulations into the dimensional quantities and compare them with observations.

Contents

Chapter 1

Introduction

It is crucially important to understand the formation of various planets such as gas giant, earth-like rocky and icy giant planets seen in the solar system. Since the first discovery of exo-planet (Mayor & Queloz 1995), over 3000 exo-planets were already found, including gas-giant, earth-like and icy giant planets. Thus, the planetary systems are considered to exist ubiquitously in the neighborhood of the solar system (or in our galaxy). Before the discovery of the first exo-planet, the planet formation scenario had been constructed based only on the solar system. However, now, we may able to elucidate the origin and evolution of the solar system composed of giant and earth-like planets referring to the exo-planets and exo-planetary systems, and construct the general formation scenario of planetary systems and various planets.

The planets and plenary systems are a byproduct of the star formation. Stars form in molecular cloud cores with a size of $L \sim 10^4$ AU. About $t \sim 10^6$ years after the molecular cloud begins to collapse, the protostar with a size of 0.01 AU forms in the central region of the gravitationally collapsing molecular cloud core. Then, the circumstellar disk appears around the protostar and grows in $t \sim 10^7$ years, during which various planets are expected to form in the disk. Very recent theoretical studies claimed that a gas-giant planet first forms in the circumstellar disk. In such studies, the rocky (or earth-like) planets and other giant or icy planets are considered to form after the first gas-giant planet formation. Thus, firstly, we need to study the formation process of the gas-giant planet in the circumstellar disk.

Recent ALMA (Atacama Large Millimeter/submillimeter Array) observations identified possible sites of planet formation. The ring-like structure, gap and density hole

(gas or dust hole) are frequently observed in the protoplanetary disk around the protostar, and they are considered to be made by protoplanets or forming planets. However, so far, researchers could not identify the existence of the proto- (or forming-) planet itself in the circumstellar disk, because the size of gas-giant planet is about 5×10^{-5} AU which is much smaller than the minimum spatial resolution of telescopes. When the ALMA capability of 0.01" is assumed, the spatial resolution of nearby star-forming regions (e.g., Taurus star forming region) is ~ 1 AU. Note that the spatial resolution of telescope is determined by both the size of the telescope and the distance from the sun. On the other hand, the size of the Hill radius, which roughly corresponds to the gravitational sphere of each planet in a planetary system, is about 0.3 AU at Jovian orbit (5.2 AU) when the Jovian mass is adopted in the solar system. In addition, the Hill radius becomes large with the increment of the orbital radius of the planet.

The gas-giant planet forms in the protoplanetary disk, in which the rocky core having about ten-times earth mass acquires the gas component from the protoplanetary disk. Since the accreting gas has an angular moment, the rotationally supported disk naturally forms around the gas-giant planet during its formation stage. In general, the gas disk around a protoplanet is called the circumplanetary disk (CPD). The circumplanetary disk forms in the Hill sphere, because the accreting matter is gravitationally bound only in it. Note that the circumplanetary disk is mainly supported by the centrifugal force against the gravity of the (gas-giant) planet and the accreted matter is supplied only from the protoplanetary disk. Although the circumplanetary disks are expected to be smaller than or comparable to the Hill radius, they can be directly observed in near future observations.

Since the existence of the circumplanetary disks is a direct proof of the planet formation, we can acquire a plenty of useful information about the formation of planets and planet-satellite systems when CPDs are observed. In this thesis, I investigate properties of the circumplanetary disk using a three-dimensional nested grid method with an extremely high-spatial resolution and show that the circumplanetary disk located about ~ 10 AU away from the central star is possible, which suggests that it can be observed even with the current instrument of telescopes. I also discuss the observational possibility of the circumplanetary disks depending on the planetary orbit and the mass of the protoplanet, and comment on the implication of the for-

mation process of protoplanet and planet-satellite system from the view point of the circumplanetary disk.

1.1 Recent observations

Firstly, the current status of recent observations is reviewed. In 1990's, since the ability of telescopes was not sufficient, researchers observed the star forming regions or the region near protostars by radio wavelengths and made a spectral energy distribution (SED) of each protostar candidate. The SEDs around very young protostar showed a clear excess in the long wave length, and researchers did not fit a single (or simple) black-body radiation. Then, the researchers interpreted the excess as the disk component associated with protostars. Thus, many researchers believed that the circumstellar (or protoplanetary) disk exists around protostar without the direct observations at those days. Theoretically, the circumstellar disk is expected to be formed because the molecular cloud core has an angular momentum (Caselli et al., 2002). Since the angular momentum is conserved, it is considered that the rotationally supported disk naturally appears in the star formation process. Since the late 1990's, the circumstellar disks were directly observed by large telescopes, such as Subaru telescope, and we could confirm the images of them.

In early 2000's, Subaru telescope implemented Coronagraphic Imager with Adaptive Optics (CIAO), which veils the central bright object (i.e., protostar) and can highlight the structure around the protostar (or circumstellar disk). However, since the researchers only observed the scattered light from the surface of the disk, they could not understand the detailed the properties of circumstellar disks. This is because the protoplanetary disk has a large optical depth in the near-infrared wavelength (Subaru Telescope). Figure 1.1 shows the observation of the circumstellar structure around AB Aur (Fukagawa et al., 2004). Similar observations were done in some other protostars and the researchers directly confirmed the disk-like structure. Therefore, from these observations, we can confidently say that the protostars really possess the protoplanetary disk.

The ALMA telescope is completed at 2012. Then, recent ALMA observations have showed surprising images of protoplanetary disks. The most striking observation is the existence of several rings in the protoplanetary disk around HL Tau (Figure 1.2).

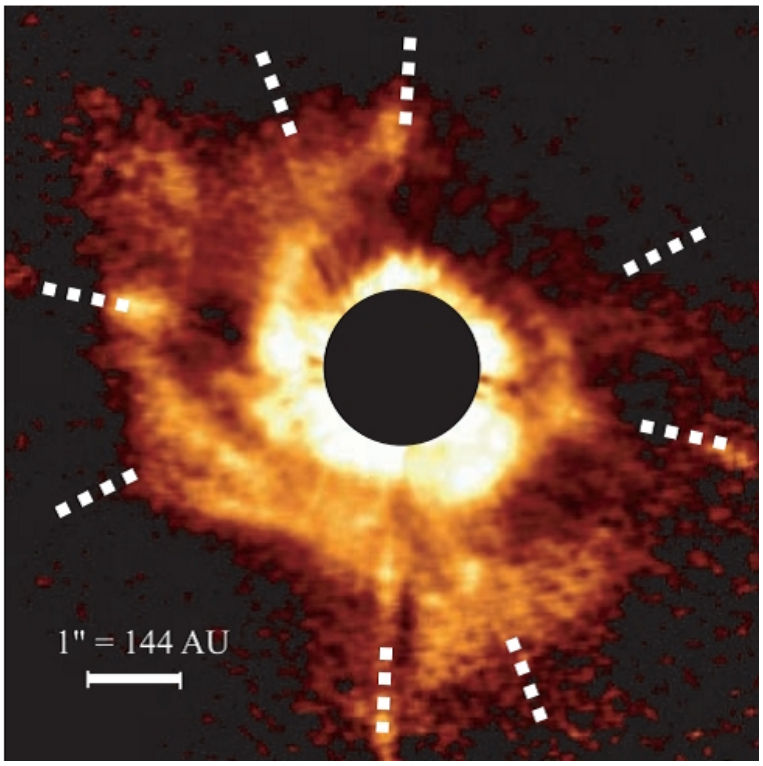

Figure 1.1. Subaru Observation of the circumplanetary disk around AB Aur (Fukagawa et al. 2004. Credit: ALMA ESO/NAOJ/NRAO). Central black circle is CHAO which masks the bright central star. Orange region corresponds to the protoplanetary disk.

Although there are many explanation and scenario of the origin of the gaps and the rings seen in Figure 1.2, the most plausible explanation is the existence of (proto or forming) planets. When a protoplanet exists in a protoplanetary disk, the planet can scatter gas particles around the protoplanetary orbit (although part of the gas is absorbed by the protoplanet). Thus, it is considered that the ring naturally appears in the circumstellar disk when the protoplanet exists. Therefore, the several rings may be a proof of the existence of the several protoplanets. In summary, now, we may just observe the stage of planet formation.

Also, a gap and a stream were observed in the protoplanetary disk around HD142527 using ALMA telescope (Fig. 1.3, Casassus et al. 2015). We can see a clear gap around

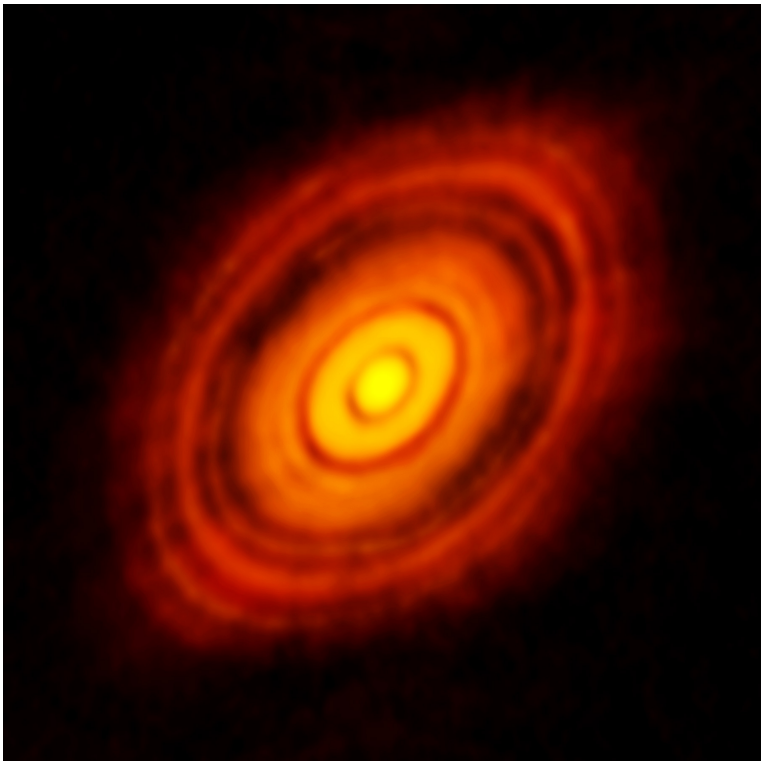

Figure 1.2. Circumstellar disk around protostar HLTau. Several gaps and rings are clearly seen. (Credit: ALMA ESO/NAOJ/NRAO)

the central bright object and the bridge between the central object and the outer disk-like structure. Although the origin of the gap and the stream have not been identified by the observation, some studies predicted that the protoplanet can create the gap or hole around the central protostar. In addition, the outer disk continues to supply the gas to the protoplanet through the stream seen in the gap.

More recently, several rings and two streams were observed using ALMA telescope (TW Hydrae; Figure 1.4). In Figure 1.4, we can see several rings in a large scale, while the gap and stream can be seen in a small scale (the inset of Fig. 1.4). Thus, TW Hydrae also may show the planet formation stage.

Some protoplanetary disks show the gap and spiral structure (SEEDS project). These disks were called the transitional disk just after its discovery, because it is considered that they are the disks during the gas depletion phase. However, recent

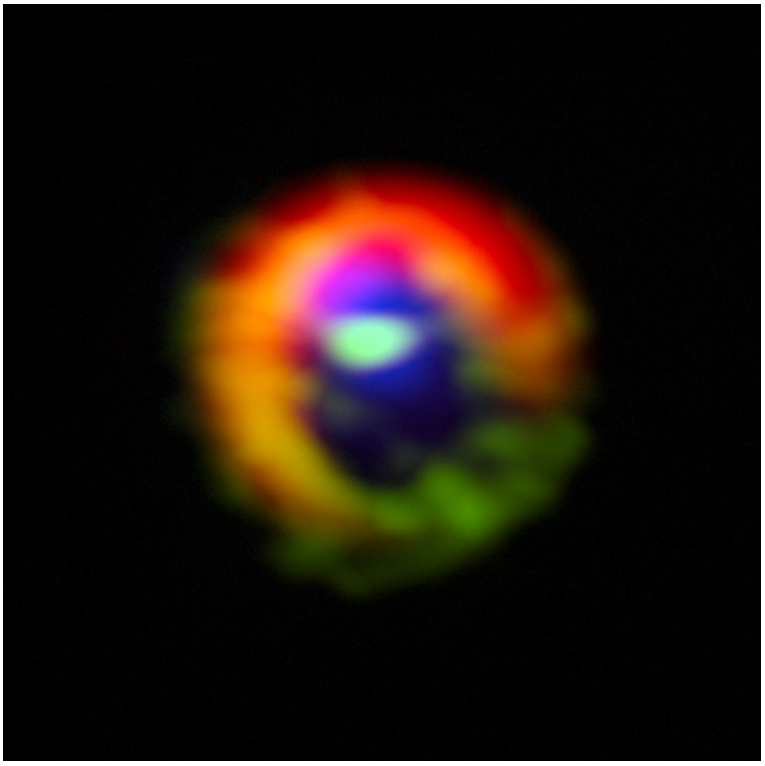

Figure 1.3. The distribution of gas and dust around protostar HD142527. Two disks are clearly seen the outer and inner disks. The gas streams also can be seen between the outer and the inner disks. The gap (the region between the inner and outer disks) may be formed by the protoplanet. The protoplanet is expected to be located in the gas stream. Credit: ALMA (ESO/NAOJ/NRAO), S. Casassus et al.

observations and theoretical studies imply that the protoplanet can produce the gap and spiral structure during its formation stage.

An exo-planet was found with the radial velocity method at 1995 for the first time as mentioned above. Then, three exoplanets were directly observed at 2008. Figure 1.5 shows an example of the direct observation of exo-planet. In the figure, the exo-planet is oriented toward the north west side.

So far, some exo-planets were confirmed by direct imaging observations (http://exoplanet.eu/). However, we have not observed the forming planets yet. To establish the planet formation scenario or planet formation process, we

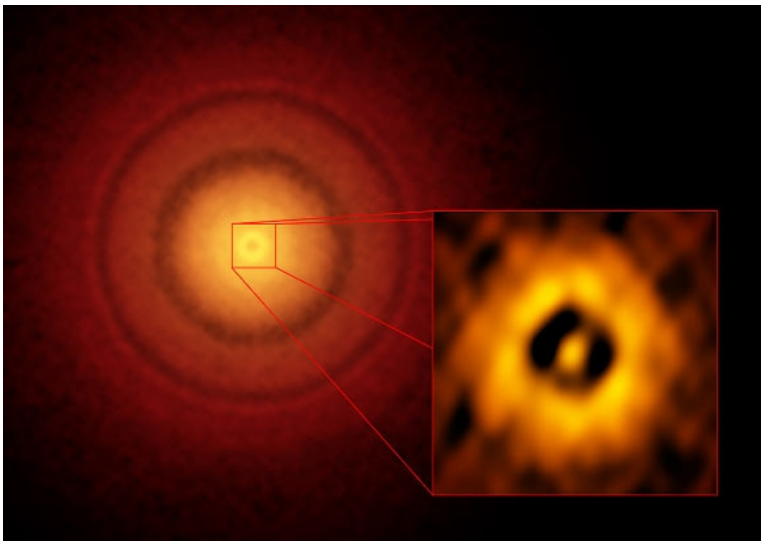

Figure 1.4. The protoplanetary disk around TW Hydrae. Zoomed image are inset. In a large scale, several rings exist. In a very small scale, the gap and gas flow (streams) are confirmed, and they are considered to be formed by the gas-giant planets. (ALMA / ESO / NAOJ / NRAO)

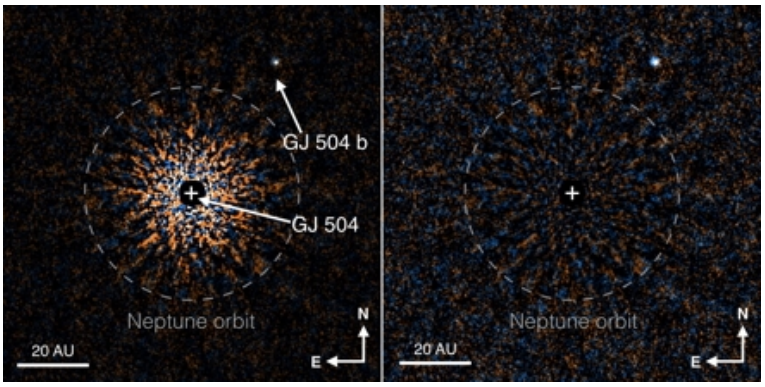

Figure 1.5. Direct observation of Planet orbiting GJ504 (Crejit:NAOJ)

inevitably need to confirm forming planets or circumplanetary disks. Sallum et al. (2015) found that Hα emission in a protoplanetary disk (LKCa 15). Without considering the protoplanet and circumplanetary disk, it is difficult to emit such a line in the protoplanetary disk. Thus, it is interpreted as a proof of the accretion luminosity onto the protoplanet or circumplanetary disk.

Thus, although there are some indirect proofs of the forming planet in the circumstellar disk, we have no observation of direct proof on it. As described above, the protoplanet is too small to be directly observed even in near future observations. Instead, we may able to observe the circumplanetary disks formed around protoplanet by current telescopes. However, we do not know the properties of the circumplanetary disk. Thus, we need to predict it in theoretical or numerical studies.

1.2 Theoretical works

There exist some star forming regions near the sun. Several hundreds of stars are born in each star forming region and the star forming condition have been clearly observed by radio telescopes. Observations indicate that stars form in the molecular cloud core which typically has a size of $\sim 10^4\,\mathrm{AU}$ and $\sim 1\,M_\odot$. In molecular cloud cores, since the gravitational energy dominates the thermal, rotational and magnetic energies, the gravitational collapse occurs to form a protostar. After the cloud collapse begins, the cloud isothermally contracts. Then, the dust thermal emission becomes optically thick and the collapsing gas behaves adiabatically and the first adiabatic core forms. Since the first core slowly contracts and the collapsing timescale becomes shorter than the rotation timescale, the magnetic field lines are strongly twisted and the outflow appears from the first core. In addition, the magnetic braking effectively transfers the angular momentum outward. On the other hand, the magnetic field dissipates inside the first core, because the ionization degree becomes extremely low and Ohmic dissipation becomes effective in a dense gas region. Therefore, both Lorentz and centrifugal forces weaken and further contraction is promoted.

When the number density of the collapsing cloud (or the contracting first core) exceeds $n > 10^{15}\,\mathrm{cm}^{-3}$, the molecular hydrogens are dissociated and the second collapse occurs. After the dissociation of molecular hydrogen is completed, the gas behaves adiabatically again. Then, the gas contraction stops and the protostar appears (Lar-

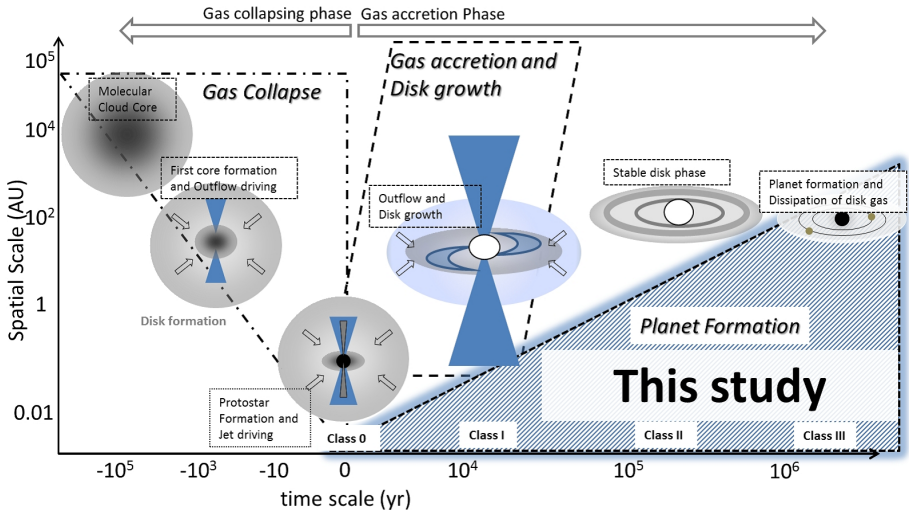

Figure 1.6. Schematic view of star formation in collapsing cloud. The gas accretion and circumstellar disk formation stage are also presented.

son 1969, Masunaga & Inutsuka 2000). The remnant of the first core remains even after protostar formation, and it evolves into the circumstellar disk (Bate, 1998). After protostar formation (gas collapsing phase), the lump of gas firstly accretes onto the circumstellar disk. Then, although a part of the gas is ejected by the protostellar outflows and jets, the remainder gradually moves toward the central protostar in the circumstellar disk. The star formation scenario expected by recent theoretical studies is summarized in Figure 1.6.

As seen in Figure 1.6, the circumstellar (or protoplanetary) disk is gravitationally unstable in the early phase of the star formation. However, as the protostellar mass increases, the disk becomes stable against the gravitational instability (Toomre, 1964). The planet formation is expected to occur in such a stable disk.

The standard scenario of planet formation is schematically presented in Figure 1.6. As seen in the figure, the protoplanetary disk is composed of gas and solid components (dusts). The dusts settle into the equatorial plane and planetesimals form. The planetesimals grow by collision and the earth-like (rocky or icy) protoplanets form. After the mass of protoplanet exceeds about 10 earth mass, the protoplanet cannot maintain its massive gas envelope due to strong gravity of protoplanet and the runaway

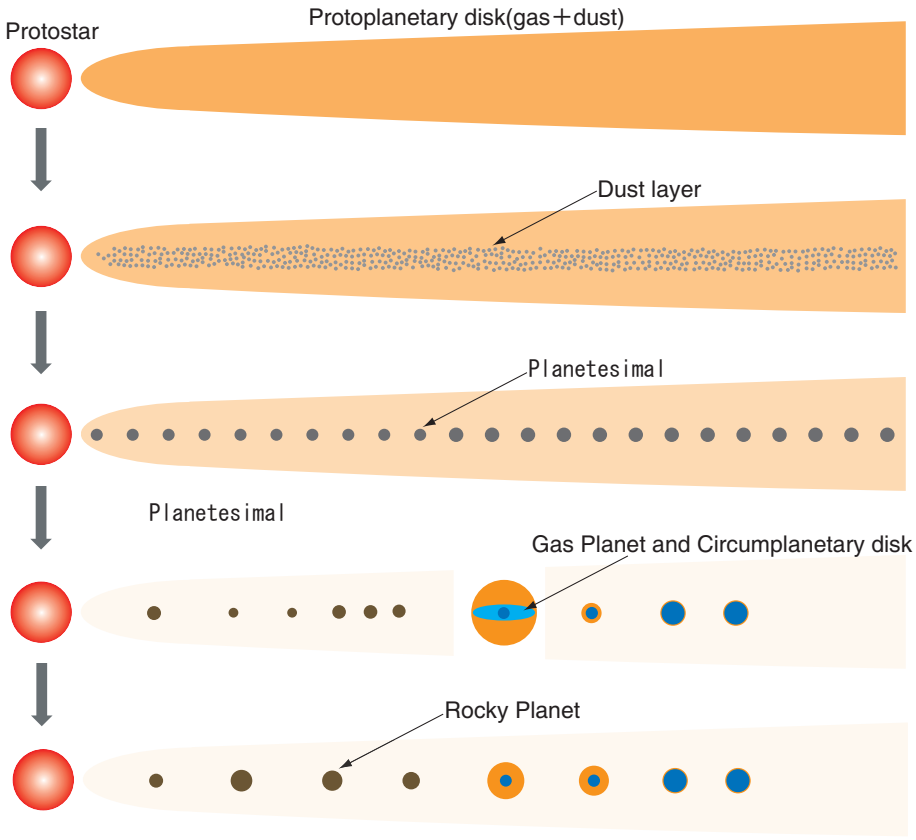

Figure 1.7. Schematic view of planet formation.

gas collapse begins (Mizuno et al. 1978, Mizuno 1980, Ikoma et al. 2000). In the runaway gas collapsing phase, the circumplanetary disk is expected to be formed because the accreting gas has an angular momentum. Thus, multi-dimensional simulations are necessary to investigate the gas-giant planet formation. Using multi-dimensional simulations, the gas-planet formation was studied (Miyoshi et al. 1999, Lubow et al. 1999, Kley et al. 2001, D'Angelo et al. 2003, Tanigawa & Watanabe 2002). As described above, we need to understand the properties of circumplanetary disk in order to identify the forming planet (or protoplanet) in observations. However, the circumplanetary disk was not fully resolved in two (Tanigawa & Watanabe, 2002) and three (D'Angelo et al., 2003) dimensional simulations due to limitation of the CPU performance at those days. Using three-dimensional simulations, Machida (2009), Machida et al. (2008, 2010), Ayliffe & Bate (2009) managed to resolve the circumplanetary disk.

However, since their studies focused on the Jovian or Saturn orbit in our solar system, it is difficult to apply their results to other planetary systems. Recently, Gressel et al. (2013) studied the gas-giant planet formation with the state-of-art simulations, in which the magnetic field and its dissipation process were considered. However, they also assumed the Jovian orbit to apply the gas opacity and magnetic resistivity of the protoplanetary disk. Thus, their results are not applicable to other orbits or other planetary systems.

1.3 Aim of this study

Recent observations imply the planet formation in the protoplanetary disk, while yet we have no smoking gun of the planet formation or forming planet even in protoplanetary disks observed by the newest telescopes. The protoplanet cannot be spatially resolved by current and future telescopes, while the circumstellar disks are able to resolve in near future (or current) observations. Thus, we need to theoretically understand the properties of the circumstellar disks in various planetary systems before the observations. However, so far, only a few studies focused on the formation and evolution of the circumplanetary disk. In addition, these studies limited the giant planet formation to Jovian or Saturn orbit in our solar system. Thus, when the general properties of circumplanetary disks are identified from a theoretical study, we can compare them taken from the theoretical study with observations. Therefore, I would unveil the planet formation in various planetary systems.

Chapter 2

Model for Numerical Simulation

In this chapter, after describing the basic equations used in simulations, I transform it into the non-dimensional form. We cannot calculate the entire protoplanetary disk and time evolution of the protoplanet because we need to spatially resolve the protoplanetary disk, circumstellar disk, and protoplanet. The spatial scale of the protoplanetary disk, circumstellar disk and protoplanet is $\sim 100\,\mathrm{AU}$, $\sim 0.1\,\mathrm{AU}$ and $\sim 10^{-4}\,\mathrm{AU}$, respectively. Thus, difference in spatial scale between protoplanetary disk and protoplanet is about 10^7. In addition, the timescale among them is considerably different. Thus, I use the local Hill coordinate, in which only a local region around the protoplanet is calculated using the Hill approximation as mentioned below, and a quasi-steady solution is calculated. I assume a standard model of the protoplanetary disk and the Keplerian motion of the protoplanet. In the Hill approximation, the Hill radius controls the mass and orbit of the protoplanet.

2.1 Fluid motion around a planet embedded in a protoplanetary disk

Let us consider a inviscid isothermal fluid around a protoplanet embedded in a protoplanetary disk. I define a local Cartesian coordinate with the origin at the planet, which rotates in circular orbit around a central protostar with the Keplerian velocity on the equatorial plane of the protoplanetary disk. In the coordinate, the x-, y-, and z-axis corresponds to the radial, azimuthal, and vertical direction of the protoplanetary disk, respectively. The basic equations in the coordinate are described

as

$$\frac{\partial \boldsymbol{v}}{\partial t} + (\boldsymbol{v} \cdot \nabla)\boldsymbol{v} = -\frac{\nabla P}{\rho} - \nabla \varphi_{\rm eff} - 2\Omega_{\rm p}\, \mathbf{e}_z \times \boldsymbol{v}, \tag{2.1}$$

$$\frac{\partial \rho}{\partial t} + \nabla \cdot (\rho \boldsymbol{v}) = 0, \tag{2.2}$$

where ρ, t, $\boldsymbol{v}$, p, $\varphi_{\rm eff}$, and $\mathbf{e}_z$ are the gas density, gas velocity, gas pressure, effective potential, and the unit vector in the z-axis, respectively. The gas self-gravity is ignored in this study, because the gravity of protostar and protoplanet dominate the gas-selfgravity. The Keplerian angular velocity of the protoplanet $\Omega_{\rm p}$ is given by

$$\Omega_{\rm p} = \sqrt{\frac{GM_{\rm c}}{r_{\rm p}^3}}, \tag{2.3}$$

where G is the gravitational constant, $M_{\rm c}$ is a stellar mass, and $r_{\rm p}$ is the distance of a protoplanet from the central star. I adopt an isothermal equation of state

$$P = c_{\rm s}^2 \rho, \tag{2.4}$$

where $c_{\rm s}$ is a constant sound speed, and I assume an optically thin disk.

The effective potential $\varphi_{\rm eff}$ is given by

$$\varphi_{\rm eff} = \varphi_{\rm c} + \varphi_{\rm rot} + \varphi_{\rm p}, \tag{2.5}$$

where $\varphi_{\rm c}$, $\varphi_{\rm rot}$, and $\varphi_{\rm p}$ are the gravitational potential of the central star, the orbital centrifugal potential, and the gravitational potential of protoplanet respectively. These potentials are defined by,

$$\varphi_{\rm c} = \frac{-\Omega_{\rm p}^2 r_{\rm p}^3}{\sqrt{(r_{\rm p}+x)^2 + z^2}}, \tag{2.6}$$

$$\varphi_{\rm rot} = -\Omega_{\rm p}^2 \left(\frac{x^2}{2} + r_{\rm p} x \right), \tag{2.7}$$

$$\varphi_{\rm p} = \frac{-GM_{\rm p}}{\sqrt{x^2 + y^2 + z^2}}, \tag{2.8}$$

in which the curvature of the protoplanetary disk is neglected. I expand $\varphi_{\rm c}$ around the origin and ignore the third and the higher-order terms. Adding $\varphi_{\rm rot}$ to $\varphi_{\rm c}$, I can obtain

$$\varphi_{\rm c} + \varphi_{\rm rot} = -\Omega_{\rm p}^2 \left(r_{\rm p}^2 + \frac{3x^2}{2} - \frac{z^2}{2} \right). \tag{2.9}$$

The first term of the right-hand side can be neglected because it is constant. Note that I set the origin as the position of the protoplanet (i.e., $r_{\rm p} = 0$). Substituting equation (2.9) into equation (2.5), I can obtain an approximate expression of the effective potential $\varphi_{\rm eff}$ as

$$\varphi_{\rm eff} = -\frac{\Omega_{\rm p}^2}{2}(3x^2 - z^2) + \varphi_{\rm p}. \tag{2.10}$$

2.2 Unperturbed state of the protoplanetary disk

As an unperturbed disk state, I assume a disk without protoplanet. The disk rotates with the Keplerian motion and is in a hydrostatic equilibrium in the vertical direction. I use this unperturbed disk model as the initial condition. In the local Cartesian coordinate, the fluid velocity of the unperturbed disk can be described as

$$\boldsymbol{v}_0 = \left(0, -\frac{3}{2}\Omega_{\rm p}\, x, 0\right), \tag{2.11}$$

in which the y-direction of the velocity originates from the Keplerian rotation of the protoplanetary disk. The equation of motion in the z-direction can be written as

$$\frac{c_{\rm s}^2}{\rho_0}\frac{\partial \rho_0}{\partial z} = -GM_{\rm c}\, z \left[(r_{\rm p} + x)^2 + z^2\right]^{-3/2}, \tag{2.12}$$

where ρ_0 is the gas density of the protoplanetary disk. Integrating this equation, I have the density distribution in the vertical direction

$$\rho_0 = \frac{\Sigma_0}{\sqrt{2\pi}{\rm H}} \exp\left(-\frac{z^2}{2{\rm H}^2}\right), \tag{2.13}$$

where Σ_0 is the surface density of the protoplanetary disk and defined by

$$\Sigma_0 \equiv \int_{-\infty}^{\infty} \rho_0 \; dz, \tag{2.14}$$

and H is the scale height of the protoplanetary disk [*1] , and defined as

$${\rm H} = \frac{c_{\rm s}}{\Omega_p}. \tag{2.15}$$

[*1] This definition of the scale height is $\sqrt{2}$ times smaller than the standard value, but this form is often used in non-dimensionalization for convenience.

The sound speed of gas is given by

$$c_{\rm s} = \sqrt{\frac{k_{\rm B}T}{\mu m_{\rm H}}}, \tag{2.16}$$

where $k_{\rm B}$, T, μ, and $m_{\rm H}$ are Boltzmann constant, the temperature, the mean molecular weight, and the mass of a hydrogen atom, respectively. Assuming the thermal equilibrium between the disk gas and the dust, I have

$$T = 280 \left(\frac{L}{L_\odot}\right)^{1/4} \left(\frac{r_{\rm p}}{1\ [\rm AU]}\right)^{-1/2}\ [\rm K], \tag{2.17}$$

where L and $L_\odot$ are the protostellar and solar luminosities.

2.3 Non-dimensionalization

In order to transform the equations described in section 2.1 into a dimensionless form, we scale the length by H, the time by $\Omega_{\rm p}^{-1}$, and the density by $\Sigma_0/r_{\rm H}$, where $r_{\rm H}$ is the Hill radius given by

$$r_{\rm H} = r_{\rm p}\left(\frac{M_{\rm p}}{3M_{\rm c}}\right)^{1/3}. \tag{2.18}$$

Thus, the basic equations of (2.1), (2.2), (2.4), (2.8), and (2.10) are rewritten as

$$\frac{\partial \hat{\boldsymbol{v}}}{\partial \hat{t}} + (\hat{\boldsymbol{v}}\cdot\hat{\nabla})\hat{\boldsymbol{v}} = \frac{-1}{\hat{\rho}}\hat{\nabla}\hat{P} - \hat{\nabla}\hat{\varphi}_{\rm eff} - 2\hat{\boldsymbol{z}}\times\hat{\boldsymbol{v}}, \tag{2.19}$$

$$\frac{\partial \hat{\rho}}{\partial \hat{t}} + \hat{\nabla}\cdot(\hat{\rho}\hat{\boldsymbol{v}}) = 0, \tag{2.20}$$

$$\hat{P} = \hat{\rho} \tag{2.21}$$

$$\hat{\varphi}_p = \frac{-3\hat{r}_{\rm H}^3}{\sqrt{\hat{x}^2+\hat{y}^2+\hat{z}^2}}, \tag{2.22}$$

$$\hat{\varphi}_{\rm eff} = \frac{-1}{2}(3\hat{x}^2 - \hat{z}^2) + \hat{\varphi}_{\rm p}, \tag{2.23}$$

where the circumflex denotes nondimensional variables. The relations between Hill radius and the planetary mass are shown in figure 2.1. The gravity of the planet dominates that of the protostar inside the radius $r_{\rm H}$. The unperturbed nondimensional

velocity and density are described as

$$\hat{\boldsymbol{v}}_0 = \left(0, -\frac{3}{2}\hat{x}, 0\right), \tag{2.24}$$

and

$$\hat{\rho}_0 = \frac{1}{\sqrt{2\pi}} \exp\left(-\frac{\hat{z}^2}{2}\right). \tag{2.25}$$

As a result, three parameters $M_{\rm p}$, $M_{\rm c}$, and $r_{\rm p}$ can be removed from the original equations, and I can characterize the models using only one parameter $\hat{r}_{\rm H}$. Note that a dimensional sound speed is required to convert a non-dimensional length into dimensional one. In addition, dimensional surface density has to be defined as a model of protoplanetary disk when we discuss about a value related to the dimensional density.

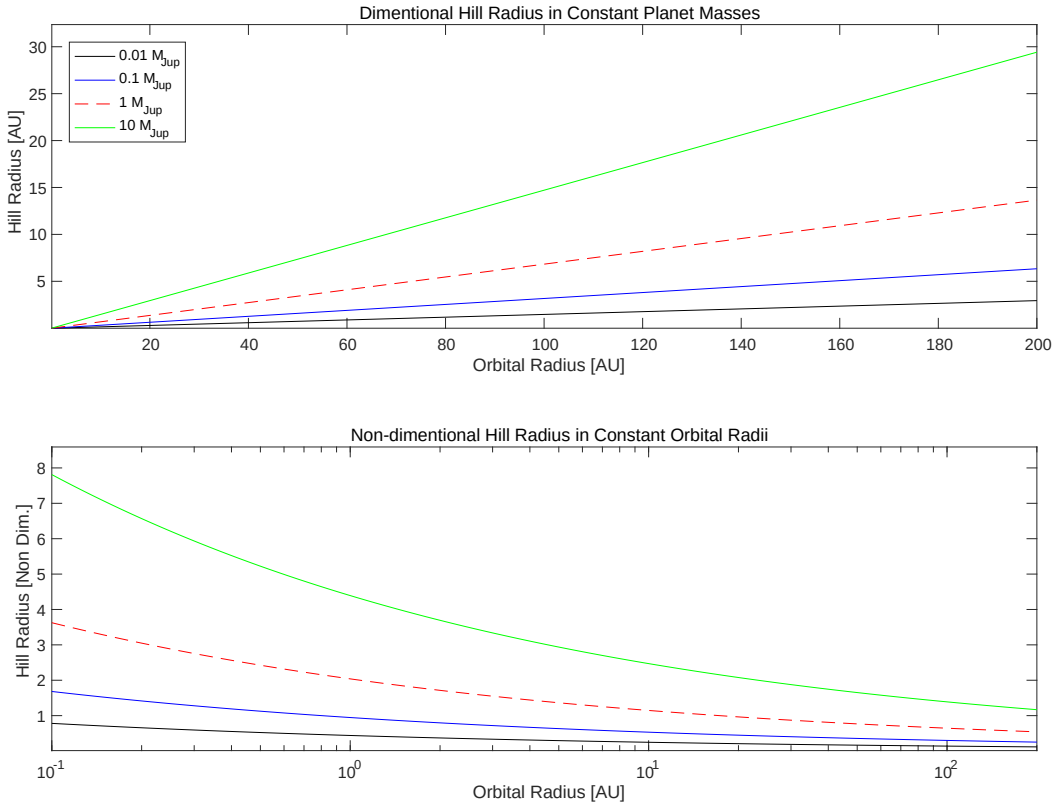

Figure 2.1. Relations between Hill radius and the planetary mass. Dimensional and non-dimensional values are plotted in the top and bottom panel. When the planet mass is fixed, the non-dimensional Hill radius increases as the orbital radius increases.

Chapter 3

Numerical Method

A circumplanetary disk is expected to be significantly smaller than the Hill radius of its own host planet. Thus, we need a very huge telescope to observe the protoplanet or length scale comparable to the planetary radius. On the other hand, in simulations, we need to resolve a few period of the spiral density waves in the circumplanetary disk, which is induced by the interaction between the protoplanetary disk and the protoplanet. Then, we also need a high spatial resolution even in numerical simulations. To realize the high spatial resolution around the protoplanet, I use the nested grid method (e.g. Machida et al. 2008, Matsumoto & Hanawa 2003).

3.1 Initial condition

The initial density profile is adopted as

$$\hat{\rho}(\hat{z}) = \hat{\rho}_{\rm init}(\hat{z}) = \max(\hat{\rho}_{\rm sky}, \hat{\rho}_0(\hat{z})), \tag{3.1}$$

where $\hat{\rho}_{\rm sky}$ is a cutoff density and is set as $\hat{\rho}_{\rm sky} = 1.5 \times 10^{-6}$ which corresponds to the value of ρ_0 at $\hat{z} = 5$. The limitation is required to avoid an unusual low density in a high altitude. Note that the disk density exponentially decreases as the distance from the equatorial plane increases (eq. 2.25). The limitation is a bit artificial. However, this limitation is realistic because the protoplanetary disk is enclosed by the infalling envelope which has a relatively high density.

For the initial velocity profile, I adopt the unperturbed disk velocity $(v_x, v_y, v_z) = (0, -3x/2, 0)$. As described below, the initial velocity is described by the non-

dimensional form.

3.2 Boundary conditions

Considering the symmetry of the equations (2.19), (2.20), (2.21), and (2.23) in the x- and y-axis, I adopt the rotational symmetry in the density and velocities as

$$\begin{aligned}
\hat{\rho}(\hat{x},\hat{y},\hat{z}) &= \hat{\rho}(-\hat{x},-\hat{y},\hat{z}),\\
\hat{v}_x(\hat{x},\hat{y},\hat{z}) &= -\hat{v}_x(-\hat{x},-\hat{y},\hat{z}),\\
\hat{v}_y(\hat{x},\hat{y},\hat{z}) &= -\hat{v}_y(-\hat{x},-\hat{y},\hat{z}),\\
\hat{v}_z(\hat{x},\hat{y},\hat{z}) &= \hat{v}_z(-\hat{x},-\hat{y},\hat{z}),
\end{aligned} \tag{3.2}$$

and the mirror symmetry at the velocity in the z direction as

$$\hat{v}_z(\hat{x},\hat{y},\hat{z}) = -\hat{v}_z(\hat{x},\hat{y},-\hat{z}), \tag{3.3}$$

where $\hat{v}_x$, $\hat{v}_y$, and $\hat{v}_z$ are $\hat{x}$-, $\hat{y}$-, and $\hat{z}$-component of gas velocity. With these boundary conditions, my computations are executed only in the region of

$$0 \le \hat{x} \le \hat{L}_x, \tag{3.4}$$

$$-\hat{L}_y/2 \le \hat{y} \le \hat{L}_y/2, \tag{3.5}$$

$$0 \le \hat{z} \le \hat{L_z}, \tag{3.6}$$

where the $\hat{L}_x$, $\hat{L}_y$, and $\hat{L}_z$ are the length of the computational domain in $\hat{x}$-, $\hat{y}$-, and $\hat{z}$-axis, respectively. I impose the computational boundary at $\hat{x} = 0$ and $\hat{z} = 0$ considering the symmetry described above.

The boundary conditions of the density and velocity are $\hat{\rho} = \hat{\rho}_{\rm init}$ and $\hat{\boldsymbol{v}} = \hat{\boldsymbol{v}}_0$ at $x = L_x$ and $z = L_z$. The periodic boundary condition is imposed in the y direction as $\hat{\rho}(\hat{x},\hat{L}_y/2,\hat{z}) = \hat{\rho}(\hat{x},-\hat{L}_y/2,\hat{z})$ and $\hat{\boldsymbol{v}}(\hat{x},\hat{L}_y/2,\hat{z}) = \hat{\boldsymbol{v}}(\hat{x},-\hat{L}_y/2,\hat{z})$.

3.3 Simulation code

In order to obtain the required spatial resolution near the protoplanet, I use the nested grid method. This method can yield a high spatial resolution, locally generating multiple nested grids. Except for the innermost grid, each grid contains a high-resolution grid, in which the spatial resolution is doubled with the increment of the grid level. In the original nested grid code, each grid has the same number

Table 3.1. Number of cells in each axis and the boundary positions of the nested regions

level	imax	jmax	kmax	xmax	ymin	ymax	zmax
1	128	1024	24	30.00	-120.00	120.00	5.63
2	256	512	48	30.00	-30.00	30.00	5.63
3	256	512	48	15.00	-15.00	15.00	2.81
4	256	512	48	7.50	-7.50	7.50	1.41
5	256	512	48	3.75	-3.75	3.75	0.70
6	256	512	48	1.88	-1.88	1.88	0.35
7	256	512	48	0.94	-0.94	0.94	0.18
8	256	512	48	0.47	-0.47	0.47	0.09
9	256	512	48	0.23	-0.23	0.23	0.04

of computational cells and the same rectangular shape. To optimize this study, I improved the code, in which a different aspect ratio of each cell and each grid is allowed. The first grid level (i.e. root grid, $l = 1$) has the cells of $(128 \times 1024 \times 24)$ in the x-, y-, and z-directions, respectively. On the other hand, the second and higher level of grids ($l \geq 2$) have cells of $(256 \times 512 \times 48)$. The grid level, the number of cells and non-dimensional length scales in each direction used in the simulations are summarized in Table 3.1.

The Roe numerical solver (Roe, 1981) is used for the time integration of equations of hydrodynamics and an adaptive time step method is used. In this method, a time step is individually determined in each grid level. Hence, the finer grid requires a large number of integrations because of the Courant-Friedrichs-Lewy (CFL) condition.

3.4 Model parameters

Model parameters are summarized in table 3.2 which lists the model name, non-dimensional Hill radius, maximum grid level, planet mass at 5.2 AU, non-dimensional and dimensional minimum spatial resolutions and elapsed time until the end of the calculation. The model name is composed of two parts: the Hill radius and maximum

grid level. Among the models, the models containing T are the standard model that have a maximum grid level $l_{\max} = 6-9$. On the other hand, models H064R7 ($l_{\max} = 7$) and H064R9 ($l_{\max} = 9$) are made by checking the results with different resolutions. The dimensional planet masses shown in the table are derived from equations (2.15), (2.16), (2.17), and (**??**), assuming $M_{\rm c} = M_{\odot}$, $L = L_{\odot}$, and $\mu = 2.34$.

Table 3.2. Model Parameters

Model name	$\hat{r}_{\rm H}$	$l_{\max}$	$M_{\rm p}/M_{\rm Jup}(5.2{\rm AU})$	$\Delta\hat{x}(l_{\max})$	$\Delta x/r_{\rm Jup}$	Time $[\Omega^{-1}]$
H135T6	1.35	6	1.00	7.3×10^{-3}	4.1	163.47
H115T7	1.15	7	0.62	3.7×10^{-3}	2.1	40.29
H100T7	1.00	7	0.41	3.7×10^{-3}	2.1	43.01
H087T7	0.87	7	0.27	3.7×10^{-3}	2.1	87.69
H077T8	0.77	8	0.19	1.8×10^{-3}	1.0	31.68
H070T8	0.70	8	0.14	1.8×10^{-3}	1.0	26.99
H064T8	0.64	8	0.11	1.8×10^{-3}	1.0	45.09
H054T8	0.54	8	0.06	1.8×10^{-3}	1.0	35.94
H036T9	0.36	9	0.02	9.2×10^{-4}	0.5	24.56
H064R7	0.64	7	0.11	3.7×10^{-3}	2.1	21.64
H064R9	0.64	9	0.11	9.2×10^{-4}	0.5	24.09

3.5 Sink cell method

In simulations, since the protoplanet is located at the origin, the gravity of cells around the origin is extremely strong. Thus, the calculation is often broken or the long-term time integration does not work well. To avoid such situations, in various studies, a softening parameter ε, which 'softens' the gravity in the vicinity of the protoplanet, is adopted to the gravitational potential as

$$\varphi'_{\rm p} = \frac{-GM_{\rm p}}{\sqrt{x^2 + y^2 + z^2 + \varepsilon^2}}. \tag{3.7}$$

However, this technique is not sufficiently justified and causes unrealistic results near the protoplanet. Thus, the more plausible way to avoid the singularity is required to

precisely calculate the circumplanetary disk.

The most straightforward way is to resolve the surface of a protoplanet with a sufficiently high spatial resolution and remove the gas accreted on the surface every time step. However, this treatment is wasteful for my purpose. Machida et al. (2008, 2010) already mentioned this problem, and they determined the sink radius, in which the gas inside the sink radius is removed from the computational domain. This is an appropriate way for my purpose. However, since they did not discuss the amount of mass to be removed, we cannot evaluate the validity of their method. The amount of removing mass would significantly influence the structure of circumplanetary disk because the balance among the accretion flow and the outflow determines the structure in the vicinity of the protoplanet. Therefore, the correct estimation of the amount of the removed mass is crucially important.

In the simulation with the sink method, the removed gas should be determined by the pressure gradient force because I do not change the gravity of the protoplanet with a softening parameter. Thus, I need to appropriately treat the gas pressure (or pressure gradient force) when the sink method is implemented. In addition, I also need to pay attention to the gas flow in the vicinity of the protoplanet or around the sink. Obviously, the gas density and pressure are the highest at the origin (i.e., at the position of the protoplanet). Thus, the region around protoplanet (or around the origin) would have a positive pressure gradient force in the radial direction. However, from the simulation, I cannot confidently determine the gas density (and the gas pressure) at the origin because the spatial resolution is not sufficient to resolve the protoplanet. Thus, instead of adopting the density derived from the simulations, I extrapolate the density (or the pressure) at the origin using the density in the vicinity of the cell as

$$\begin{aligned}\hat{\rho}_{s:i,j} = [&6\hat{\rho}_{i+1,j} - 4\hat{\rho}_{i+2,j} + \hat{\rho}_{i+3,j} \\ &+ 6\hat{\rho}_{i,j+1} - 4\hat{\rho}_{i+1,j+1} + \hat{\rho}_{i+2,j+1} \\ &- 4\hat{\rho}_{i,j+2} + \hat{\rho}_{i+1,j+2} \\ &+ \hat{\rho}_{i,j+3}]/4,\end{aligned} \tag{3.8}$$

where i and j are the identified numbers of the sink cells located at $(\hat{x}, \hat{y}, \hat{z}) = (\Delta x/2, \Delta y/2, \Delta z/2)$. In this interpolation, density distribution in the vertical (or z) direction is neglected, because I confirmed the steeper gradient of $d\hat{\rho}/d\hat{z}$ in the vertical direction than that in the x and y direction on the equatorial plane.

There is an another sink cell at $(\hat{x}, \hat{y}, \hat{z}) = (\Delta x/2, -\Delta y/2, \Delta z/2)$, and the treatment is the same but the position rotates 90 degree with respect to the origin. At every time step of the simulations, I replace the density derived from the simulation into that is extrapolated by the cells around the protoplanet as

$$\hat{\rho}' = \min\left(\hat{\rho}, (\hat{\rho}_s + \hat{\rho})/2\right). \tag{3.9}$$

If a steady state exists, the density of sink cell would converge to a constant value with time. Note that without the averaging of right hand side of equation (3.9), I confirmed that the computation has crushed.

Chapter 4

Convergence Analysis of the Simulations

The simulation or the time-integration can continue until the simulation has crashed. Thus, I need to determine the epoch at which the simulation stops. The criterion of stopping the simulation differs from one study to another. For example, Tanigawa et al. (2012) stopped their computation when the accretion flow onto the circumplanetary disk comes to a nearly steady state. On the other hand, Szulágyi (2017) continued to run the computations until the planetary gap profile comes to a steady state. To evaluate the structure of the circumplanetary disk, I need to execute the computation until the disk becomes a steady state. However, previous studies could not show a steady state of the circumplanetary disk. This is because in such studies the simulations were performed with a softening parameter ε or smoothing length, as mentioned above.

The softening or smoothing length enables to avoid singularity of the planet' s gravitational potential at the origin and can yield realistic flow in a large scale formed by gravitational interaction, but accumulates a mass infinitely around the planet. Consequently simulations cannot be reached steady state and we would extremely overestimate the accreted mass and the size of circumplanetary disk

In this thesis, I developed a new sink method and confirmed a steady state of circumplanetary disk and convergence of physical quantities. I remove the mass of the cells every time steps in the finest grid, in which an amount of the removed gas is dynamically determined in the simulation. When the circumplanetary disk achieves

a steady state, the removed mass is equal to the mass captured by the protoplanet in the protoplanetary disk. Then, the physical quantities of the circumplanetary disk are converged. In this chapter, I show the results of the convergence test and discuss the validity of the steady state derived from my sink method.

4.1 Overview of mass distributions on the equatorial plane

Figure 4.1 shows the density distribution at the end of the simulation (the epoch is listed in Table 3.2) on the mid-plane for each model which has a different parameter of the Hill radius. As the Hill radius decreases, the radius of dense gas region, which corresponds to a circumplanetary disk, rapidly decreases. This figure also shows two pairs of spiral arms which can be observed for models with the Hill radius larger than $\hat{r}_{\rm H} \geq 0.77$ (Figs. 4.1[a]–[e]). The density of the spiral arms is higher than that of the other regions. However, for models with smaller Hill radii ($\hat{r}_{\rm H} < 0.77$), the spiral arms are not clear compared with models with larger $\hat{r}_{\rm H}$. In addition, the root of arms are away from the origin or apart from each other.

Figure 4.2 shows the surface density distributions for each model, which is calculated as

$$\Sigma(x, y) = \int_{-H}^{H} \rho(x, y, z)\, dz. \tag{4.1}$$

The area of dense region (the region with yellow color in Fig. 4.1) decreases as the Hill radius decreases. Although this tendency is similar to the density distribution on the equatorial plane, the dense spiral arms seen in the density distribution in models with $\hat{r}_{\rm H} = 0.87$ and 0.77 (Fig. 4.1[d] and [e]) do not appear in Figure 4.2(d) and (e). Thus, the dense arms are considered to be induced only near the mid-plane, while weak spiral arms are expected to appear in the region above the mid-plane. Note that although the Hill radius for models in Figure 4.2(a) is larger than that for model with Figure 4.2(b), the maximum density in the larger Hill radius model is lower than that in the higher Hill radius model. This implies that the spatial resolution affects the density distribution. This kind of the resolution dependency was reported in some previous studies (e.g. Morbidelli et al. 2014).

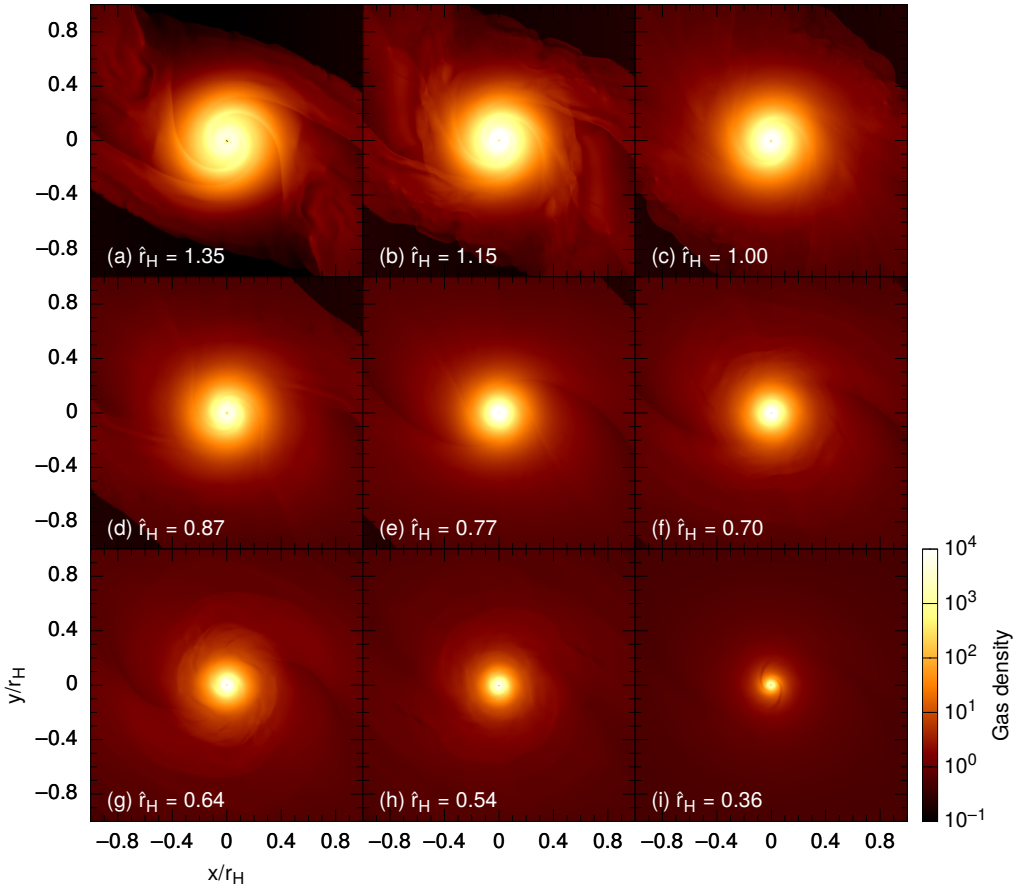

Figure 4.1. Gas density (color) on the equatorial plane around the protoplanet at the end of the simulations. Parameter $\hat{r}_{\rm H}$ differs in each panel.

4.2 Convergence of cumulative mass

In order to evaluate convergence of the calculations, the time sequence of the mass distribution is examined. Figure 4.3 shows time evolution of the cumulative mass within a radius R and scale height H for model with $\hat{r}_{\rm H} = 0.64$. The cumulative mass is calculated as

$$M_{cd}(R) = \int_0^R \int_0^{2\pi} \int_{-\rm H}^{\rm H} \rho(x, y, z)\, dz d\theta dr, \tag{4.2}$$

where r is defined as $r = \sqrt{x^2 + y^2}$, and θ is the azimuthal angle measured from the x-axis. In this figure, the cumulative masses at four different radii $R = r_{\rm H}/100$,

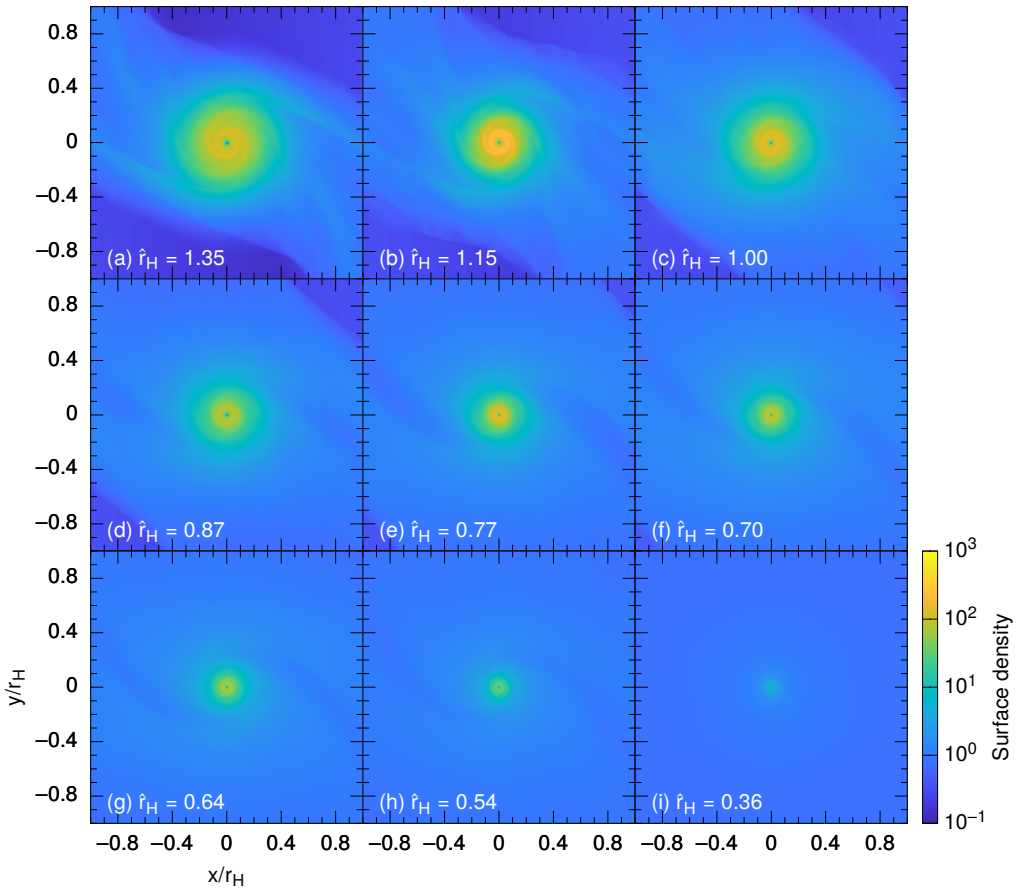

Figure 4.2. Surface density $\hat{\Sigma}$ distribution near the protoplanet at the end of the calculation for each model.

$r_H/10$, $r_H/2$ and r_H are plotted by the solid, dashed, dotted, and dash-dotted line, respectively.

After the calculation starts, the cumulative masses steeply increase and show a weak peak. Then, they converge to a constant value within an orbital period ($<2\pi\Omega^{-1}$). The time to converge the cumulative mass is sufficiently shorter than the growth timescale of the planet. This indicates that the density enhancement due to the growth of the protoplanet greatly affects the structure of the circumplanetary disk. In addition, the density distribution of the circumplanetary disk changes in a short time compared with the Keplerian timescale. Since the growth timescale of the protoplanet is much longer than the Keplerian timescale, this simulation can be regarded as a snapshot of the accreting circumplanetary disks.

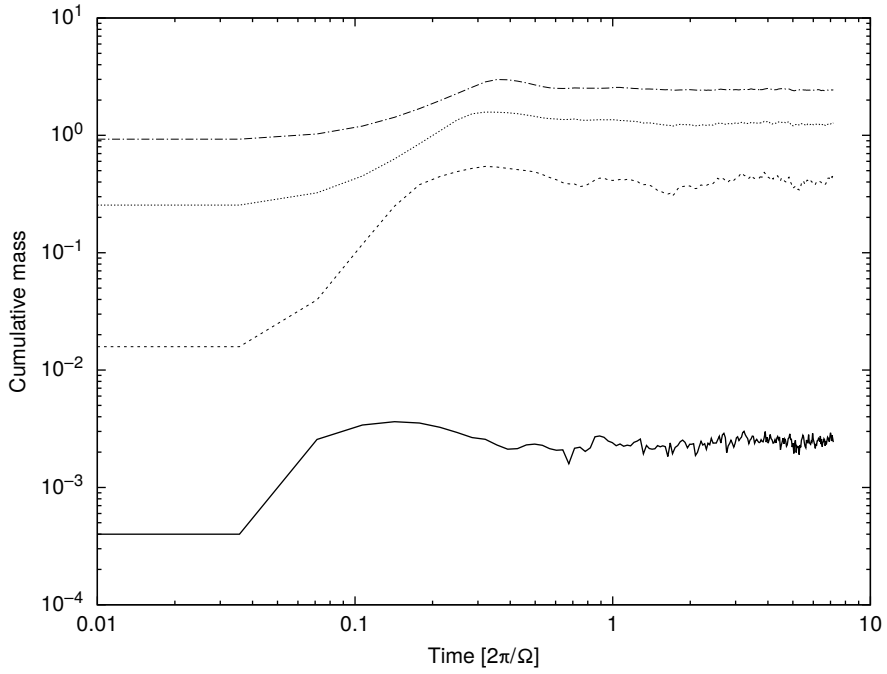

Figure 4.3. Time evolution of the accreted mass within a radius $\hat{R}$ and scale height H for model with $\hat{r}_{\rm H} = 0.64$. The solid, dashed, dotted, and dash-dotted line represents the non-dimensional mass within $\hat{R} = \hat{r}_{\rm H}/100$, $\hat{r}_{\rm H}/10$, $\hat{r}_{\rm H}/2$, and $\hat{r}_{\rm H}$, respectively. The elapsed time is normalized by the orbital period.

Figure 4.4 is the same plot as in Figure 4.3 but for model with $\hat{r}_{\rm H} = 0.36$ which has the smallest Hill radius in this study. The figure shows that cumulative masses have weak (overshooting) peaks before they converge to a constant value. The time scale for the convergence in this model is shorter than that for model with $r_{\rm H} = 0.64$. This implies that a smaller protoplanet quickly changes its surrounding structure. Thus, even for the models with a smaller Hill radius, I can regard it as a snapshot around a growing planet. However, for model with $\hat{r}_{\rm H} = 1.35$ (Fig. 4.5) which has the largest Hill radius among the models, I cannot confirm a clear convergence of the cumulative masses within the computation time. In Figure 4.5, although top three lines, which corresponds to $R \geq r_{\rm H}/10$, show a peak, they continue to decrease. On the other hand, the cumulative mass for $R = r_{\rm H}/100$ (the bottom line) also show a peak, while it keeps an almost constant value. This indicate that the radius $R = r_{\rm H}/100$ is located within the inner edge of circumplanetary disk. Although the cumulative masses seen

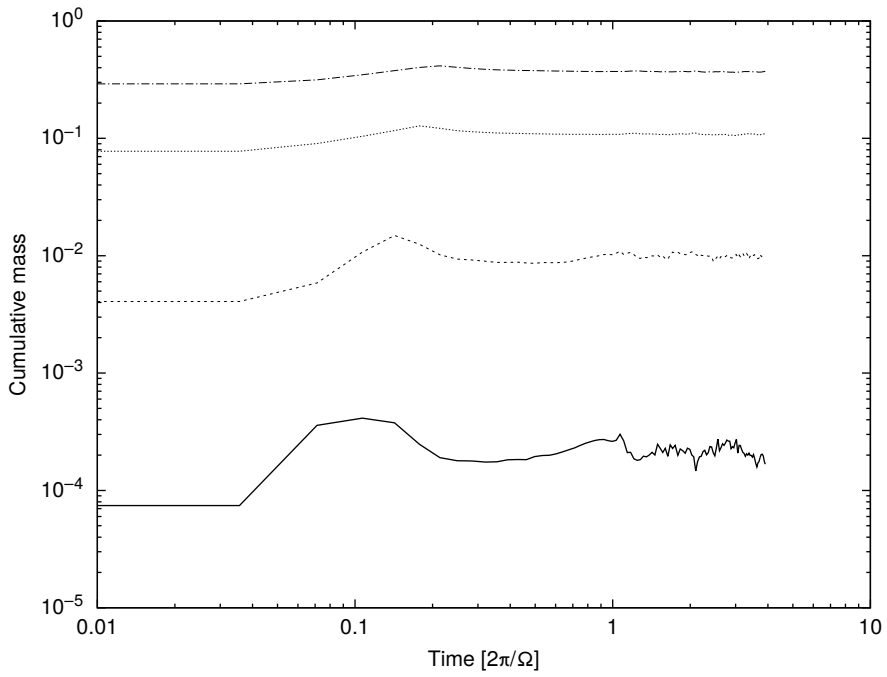

Figure 4.4. Time evolution of the accreted mass within a radius R and scale height H for model with $\hat{r}_{\rm H} = 0.36$. The solid, dashed, dotted, and dash-dotted line represents the non-dimensional mass within $\hat{R} = \hat{r}_{\rm H}/100$, $\hat{r}_{\rm H}/10$, $\hat{r}_{\rm H}/2$, and $\hat{r}_{\rm H}$, respectively. The elapsed time is normalized by the orbital period.

in Figure 4.6 also have not been completely converged, the mass within $R < r_{\rm H}/100$ keeps a constant value for $\hat{t} \gtrsim 0.2$. Thus, a steady state is expected to be achieved around the protoplanet (or inside the circumplanetary disk).

4.3 Overview of azimuthal velocity distribution on the equatorial plane

Figure 4.7 shows the azimuthal velocity distribution on the equatorial plane normalized by the local Keplerian angular velocity of the protoplanet, which is given by

$$\hat{v}_{\rm Kep} = \sqrt{3\hat{r}_{\rm H}^3 \hat{r}}, \tag{4.3}$$

for each model at the end of the calculation. The figure shows that the normalized azimuthal velocities are constant near the protoplanet, which indicates that the gas

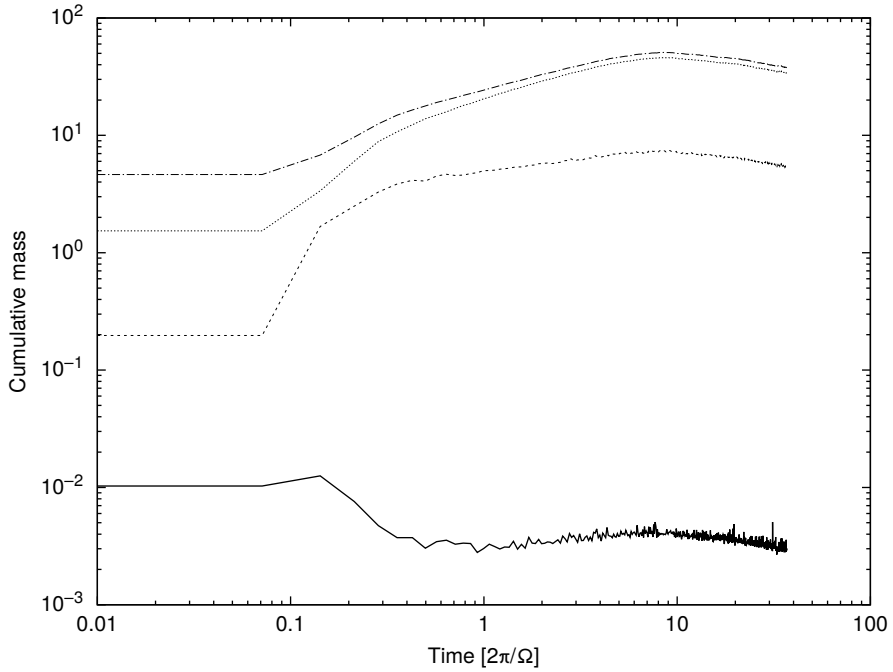

Figure 4.5. Time evolution of the accreted mass within a radius R and scale height H for model with $\hat{r}_{\rm H} = 1.35$. The solid, dashed, dotted, and dash-dotted line represents the non-dimensional mass within $\hat{R} = \hat{r}_{\rm H}/100$, $\hat{r}_{\rm H}/10$, $\hat{r}_{\rm H}/2$, and $\hat{r}_{\rm H}$, respectively. The elapsed time is normalized by the orbital period.

fluid around the protoplanet moves according to the Keplerian motion. Outside a critical radius, which is defined as the boundary between the circumplanetary disk and the protoplanetary disk, the normalized velocities are still positive, while fluid shows a turbulent motion. This feature indicates that the angular momentum transfer occurs around the critical radius. Also, the critical radii normalized by the Hill radius increase as the Hill radii increase for models.

The azimuthally averaged azimuthal velocity is calculated by

$$\bar{v}_\theta(\hat{r}) = \frac{\int_{\hat{r}-\Delta\hat{r}}^{\hat{r}+\Delta\hat{r}} \int_0^{2\pi} \hat{L}_z \, d\theta d\hat{r}}{\int_{\hat{r}-\Delta\hat{r}}^{\hat{r}+\Delta\hat{r}} \int_0^{2\pi} \hat{r}\hat{\rho} \, d\theta d\hat{r}}, \tag{4.4}$$

and is shown in Figure 4.8 for models with $\hat{r}_{\rm H} = 0.36$, 0.64, 1.00, and 1.35, in which the velocity is normalized by the Keplerian angular velocity. For each model, the region near the protoplanet has almost the Keplerian velocity, while the normalized velocity steeply decreases in the region far from the protoplanet. Gressel et al. (2013)

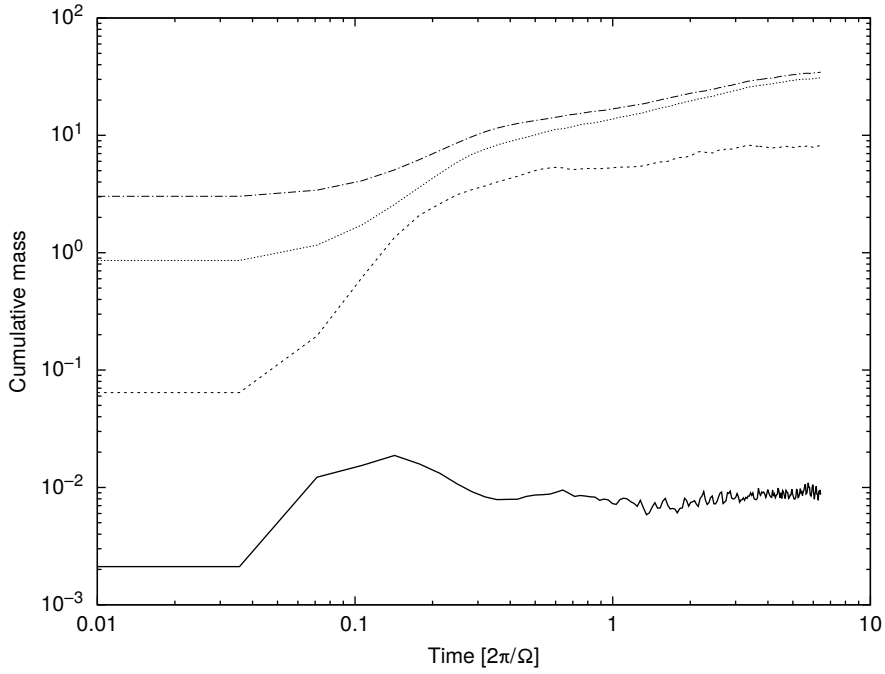

Figure 4.6. Time evolution of the accreted mass within a radius R and scale height H for model with $\hat{r}_{\rm H} = 1.15$. The solid, dashed, dotted, and dash-dotted line represents the non-dimensional mass within $\hat{R} = \hat{r}_{\rm H}/100$, $\hat{r}_{\rm H}/10$, $\hat{r}_{\rm H}/2$, and $\hat{r}_{\rm H}$, respectively. The elapsed time is normalized by the orbital period.

defined the inflection point of the radial profile using the time averaged specific angular momentum and reported that the circumplanetary disk has a radius of $0.5\hat{r}_{\rm H}$. Although the tendency seen in Figure 4.7 is similar to their result, the decreasing point of the normalized velocity (or the size of the circumplanetary disk) clearly depends on the Hill radius (or the normalized Hill parameter). Therefore, my results implies that the outer edge of circumplanetary disk has a similar dynamical structure for models with different Hill radii.

4.4 Convergence of azimuthal velocity

Convergence of the azimuthal velocity is also investigated. Figures 4.9 and 4.10 shows the time sequences of the normalized azimuthal velocity at four different radii for models with $\hat{r}_{\rm H} = 0.36$, and 1.35. The azimuthal velocity converges near the

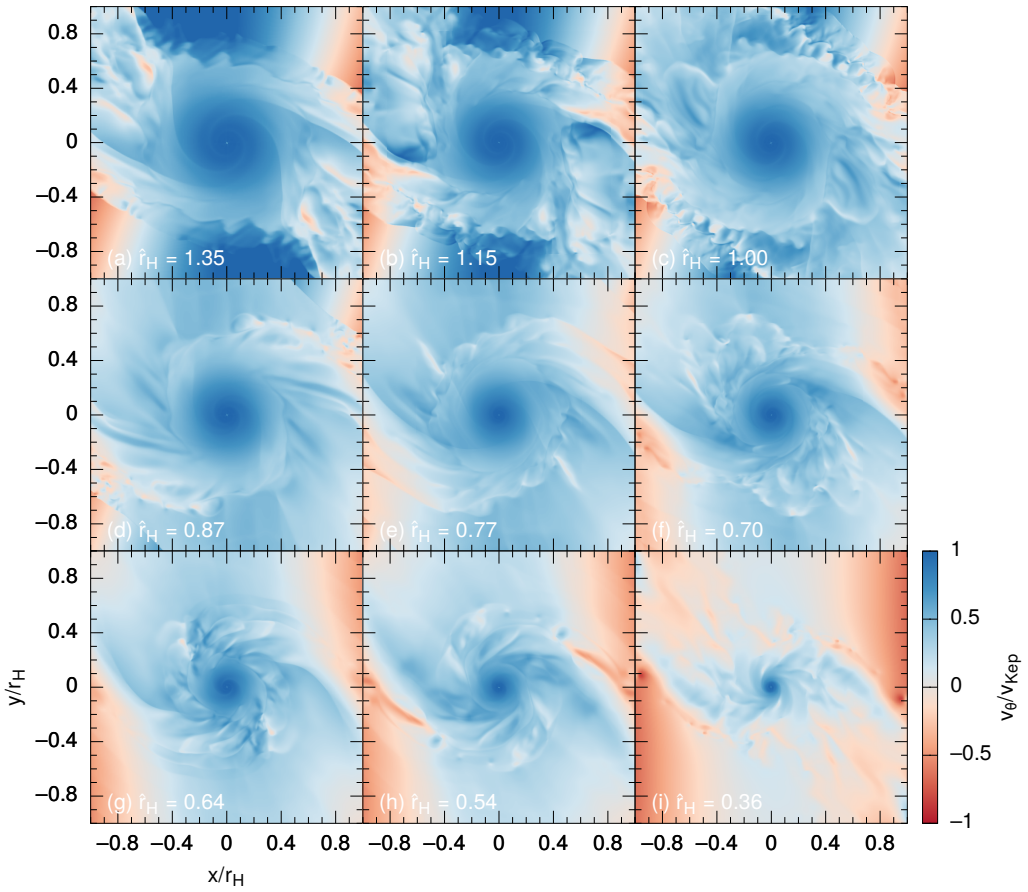

Figure 4.7. Normalized azimuthal velocity distribution for each model at the end of the calculation. The coordinate is scaled by $\hat{r}_{\rm H}$.

protoplanet, while it oscillates the region far from the protoplanet. Nevertheless, the amplitudes in the oscillation are not very large, which implies that the azimuthal velocity roughly converges in all the radii. The region showing almost constant azimuthal velocity in Figure 4.9 is located inside the critical radius, as seen in Figure 4.7(i).

4.5 Summary

In this chapter, I showed the convergence of cumulative mass and azimuthal velocity, i.e. specific angular momentum. Cumulative masses show convergence except for model with $\hat{r}_{\rm H} = 1.35$. In addition, all the azimuthal velocities profiles are con-

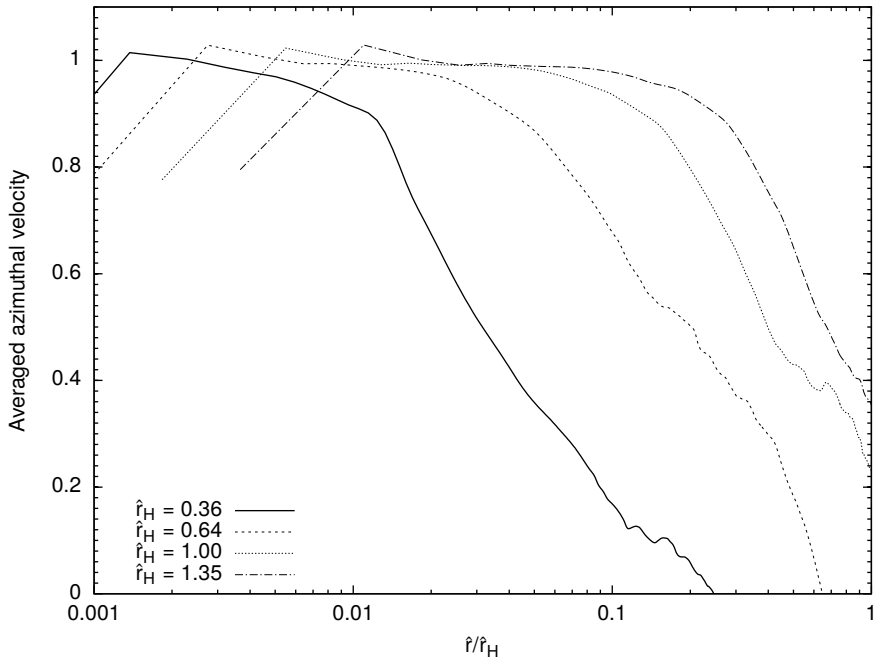

Figure 4.8. Radial profiles of the averaged azimuthal velocity on the equatorial plane. The velocity is normalized by the Keplerian velocity. Radial distances are also normalized by the Hill radius.

verged. Thus, I can check the validity of the simulation and confidently analysis the circumplanetary disk in the subsequent chapters.

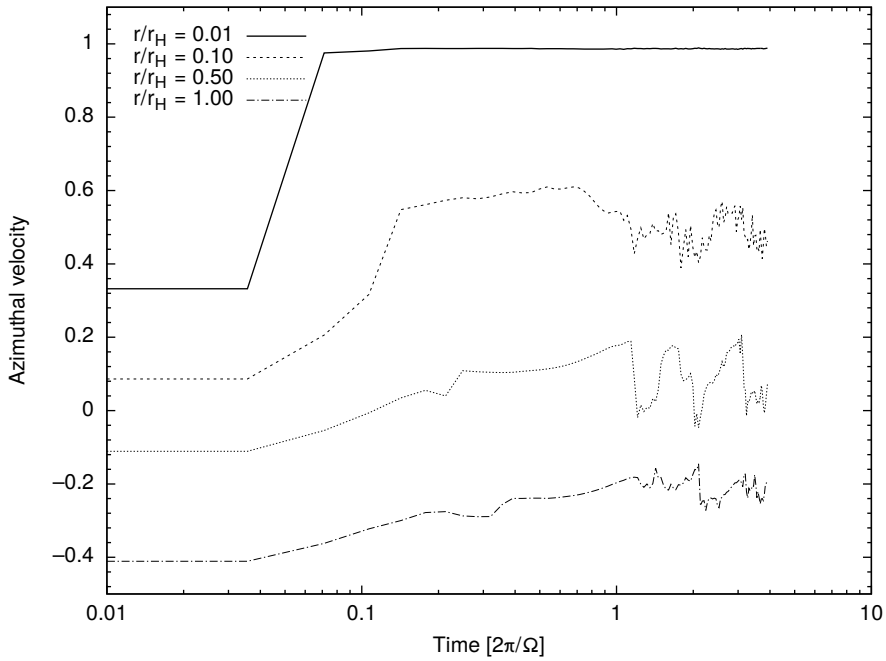

Figure 4.9. Time sequences of the azimuthal velocity on the mid-plane for model with $\hat{r}_{\rm H} = 0.36$ at different radii. The velocities and radial distances are normalized by each Keplerian velocity and the Hill radius, respectively.

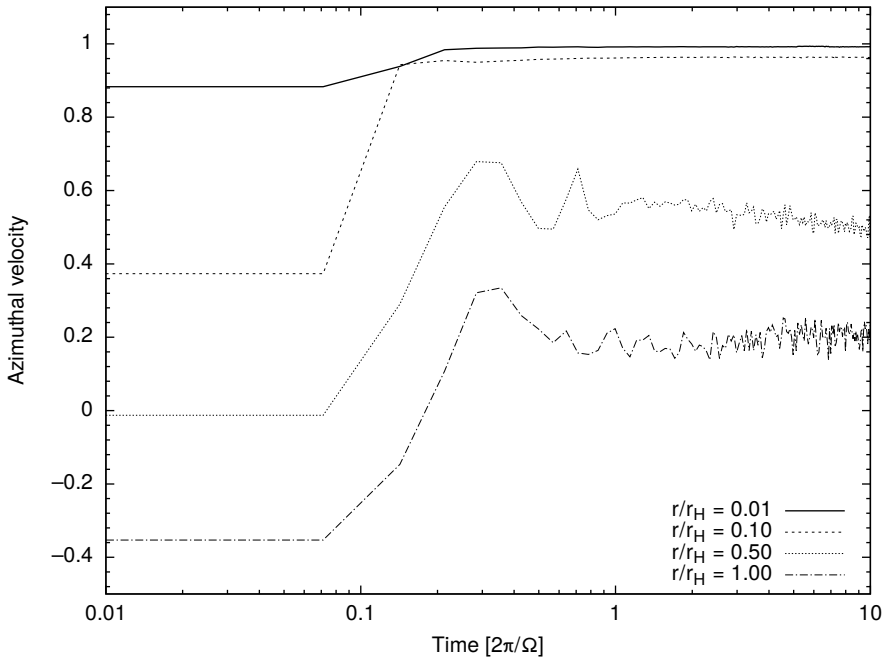

Figure 4.10. Time sequences of the azimuthal velocity on mid-plane for model with $\hat{r}_{\rm H} = 1.35$ at different radii. The velocities and radial distances are normalized by each Keplerian velocity and the Hill radius, respectively.

Chapter 5

Results and Discussions

In this chapter, I determine the spatial scale of circumplanetary disk relative to the Hill radius. Circumplanetary disks are formed in each model (see Figure 4.1 and 4.2), but the outer edges of the disk are still unclear. Azimuthally averaged radial profiles of some physical quantities which allocate the region adjacent to the midplane are evaluated. To be precise, I estimated such physical quantities on the plane of $z = \Delta z(\mathrm{lmax})/2$, which corresponds to the lowest point in the z-direction in the computational domain.

5.1 Radial profile of physical quantities

Figure 4.7 suggests the existence of a qualitative boundary between stable disk region and outer turbulent region. Thus let us determine the outer edge of the circumplanetary disk from azimuthally averaged quantities.

5.1.1 Angular momentum

Figures 5.1 to 5.9 show the radial profiles of the averaged angular momentum, which is calculated as

$$\bar{\hat{L}}(\hat{r}) = \frac{\int_{-\pi}^{\pi}\int_{0}^{\Delta z}\int_{r-\Delta r/2}^{r+\Delta r/2}\hat{r}\hat{\rho}\hat{v}_{\theta}drdzd\theta}{\int_{-\pi}^{\pi}\int_{0}^{\Delta z}\int_{r-\Delta r/2}^{r+\Delta r/2}drdzd\theta} \tag{5.1}$$

and the radial gradient. The quantities are averaged during one orbital period after the steady state is realized. The maxima and minima for each model during the

period are also plotted. The dotted line represents the Keplarian angular momentum for corresponding model (or each $\hat{r}_{\rm H}$).

In each model, the angular momentum increases with the distance from the origin according to the Keperian profile (dotted line) near the protoplanet. Then, the angular momentum is detached from the Keplerian profile after it reaches a peak value. This peak radius, where $\partial L/\partial r = 0$, is shown by the vertical dotted line in each panel. Thus, the gas motion is almost the Keplerian near the protoplanet. In model with $\hat{r}_{\rm H} = 0.36$ (Figure 5.1), a clear peak is confirmed. After the peak potision, the gradient of angular momentum becomes slightly negative and the fluctuation spreads continuously. However in model with $\hat{r}_{\rm H} = 0.54$, $\hat{r}_{\rm H} = 0.64$ and $\hat{r}_{\rm H} = 0.70$ (Figs. 5.2, 5.3 and 5.4), angular momentum stays nearly constant after the peak for a while, and then it sharply decreases in the outer region. The range between maxima and minima in the outer region is larger than that in the inner regions (before the peaks). In model with $\hat{r}_{\rm H} \leq 0.77$ (Fig. 5.5 to 5.9), the second peak exists before the sharp decrease. The fluctuation gradually increases between two peaks.

The gas in the accretion disk is supported by centrifugal and radial pressure gradient forces againt the gravity of the protoplanet. Thus the angular momentum should be redistributed by gravitational and pressure torques, and the gradient in the angular momentum smoothly changes in the inner region. On the contrary, in the outer region having a constant angular momentum, the angular momentum may not be redistributed, while the angular momentum in the infalling gas directly transports outward.

5.1.2 Radial velocity and radial mass flux

Figures 5.10 to 5.18 show the averaged radial velocity given by

$$\bar{\hat{v}}_r(\hat{r}) = \frac{\int_{-\pi}^{\pi}\int_{0}^{\Delta z}\int_{r-\Delta r/2}^{r+\Delta r/2}\hat{\rho}\hat{v}_r dr dz d\theta}{\int_{-\pi}^{\pi}\int_{0}^{\Delta z}\int_{r-\Delta r/2}^{r+\Delta r/2}\hat{\rho} dr dz d\theta}, \tag{5.2}$$

and the radial mass flux given by

$$\bar{\hat{F}}_r = \frac{\int_{-\pi}^{\pi}\int_{0}^{\Delta z}\int_{r-\Delta r/2}^{r+\Delta r/2}\hat{\rho}\hat{v}_r dr dz d\theta}{\Delta r \Delta z}. \tag{5.3}$$

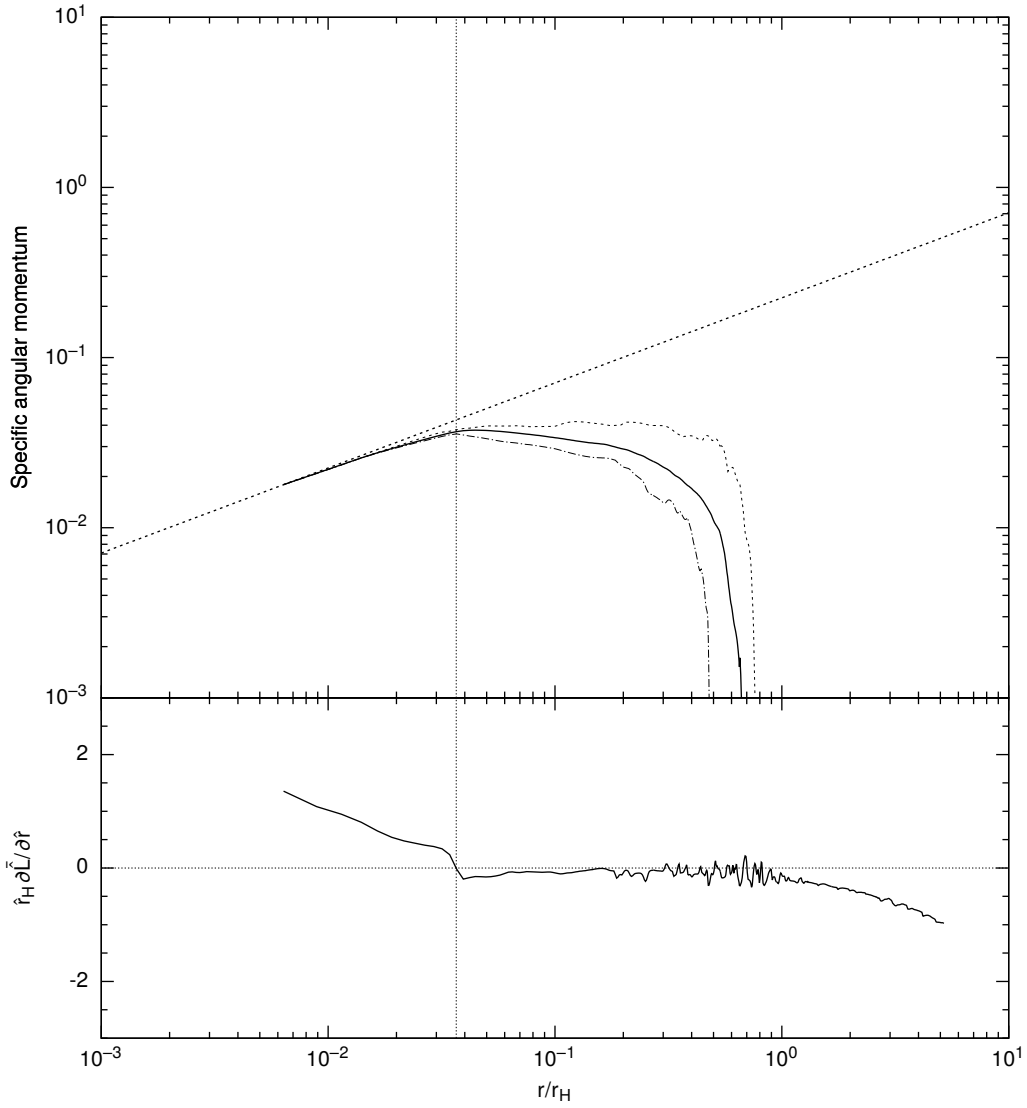

Figure 5.1. Azimuthally averaged non-dimensional angular momentum (top panel) and gradient of it (bottom panel) for model with $\hat{r}_{\rm H} = 0.36$. The solid, dashed, and dash-dotted line show the time averaged, maximum and minimum value, respectively. The dotted line on the top panel denotes the Keplerian angular momentum. The horizontal dotted line in the bottom panel means $\partial L/\partial r = 0$, while the vertical lines correspond to the radius of $\partial L/\partial r = 0$.

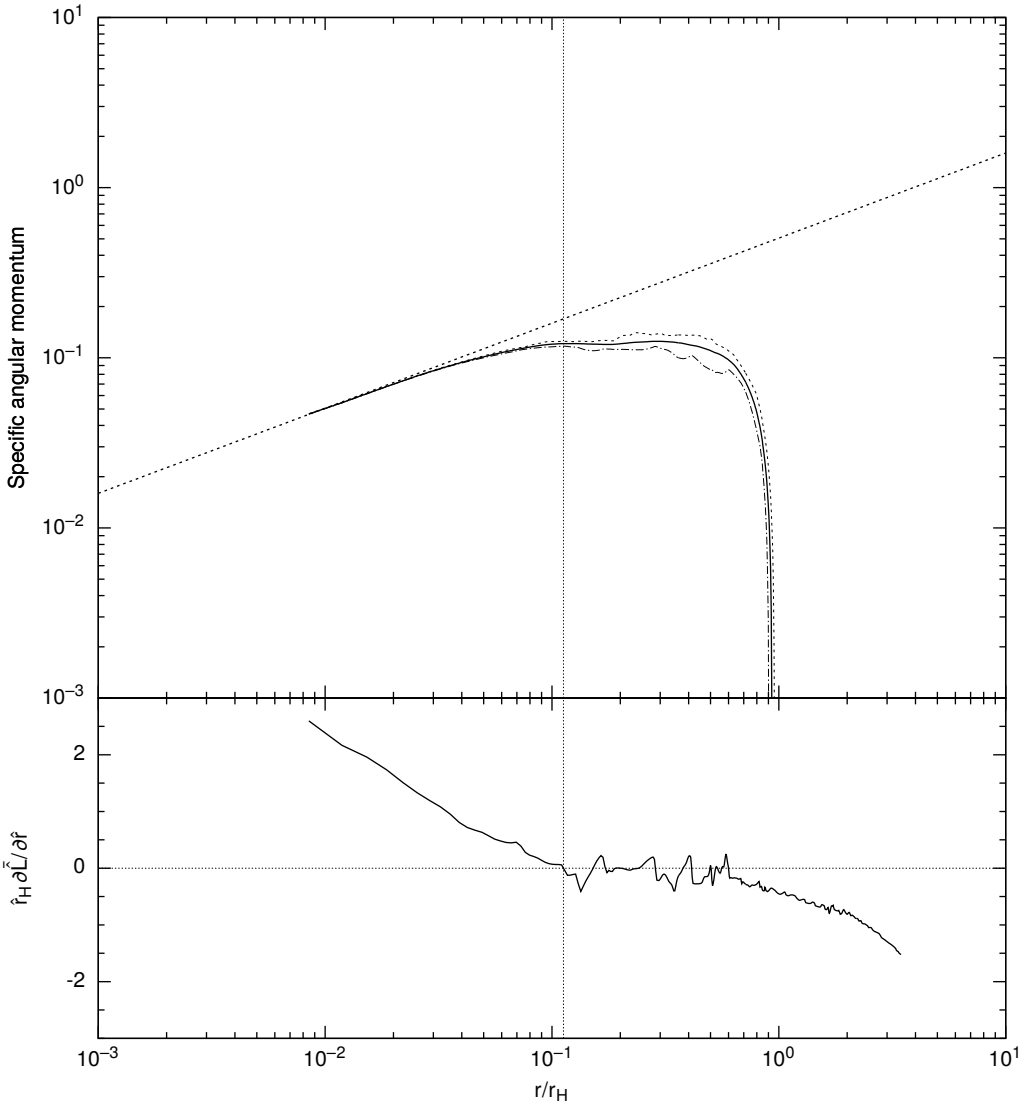

Figure 5.2. Same as in Figure 5.1, but for model with $\hat{r}_{\rm H} = 0.54$.

These values are also averaged in last one orbital period. In these figures, the vertical dotted line denotes the position $\partial L/\partial r = 0$, which is same as the figures of the angular momentum profile (Figs. 5.1 to 5.9). For model with $\hat{r}_{\rm H} = 0.36$ (Figure 5.10), the radial velocity is positive inside the vertical line, and it is negative outside it. Therefore, the angular momentum is excessive in the inner region and not enough to support gas fluid against the gravity of the protoplaent in the outer region. Thus, the gas fluid cannot stay in the outer region. Also, for model with $\hat{r}_{\rm H} = 0.54$, the

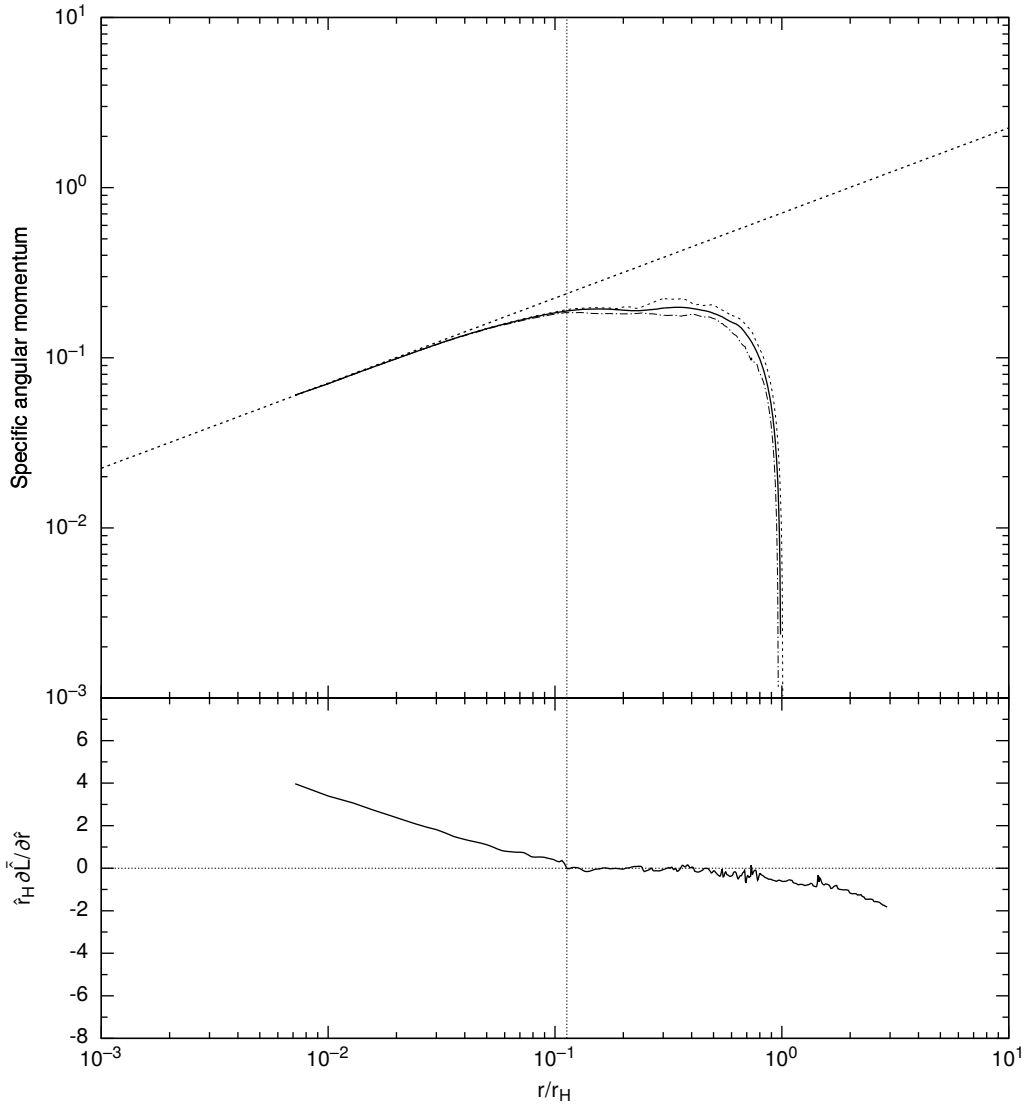

Figure 5.3. Same as in Figure 5.1, but for model with $\hat{r}_{\rm H} = 0.64$.

vertical line divides into the inner and outer region. However, the inward mass flux disappears in the outer region because of the low density. Therefore, the inward mass flux is negligible on the midplane. The fluctuations in the radial velocity (top panel) sharply spreads from the vertical line, while the fluctuation in the radial mass flux increases inside the vertical line. These trends also exist in larger $\hat{r}_{\rm H}$ models (≥ 0.64; Figure 5.12 to 5.18).

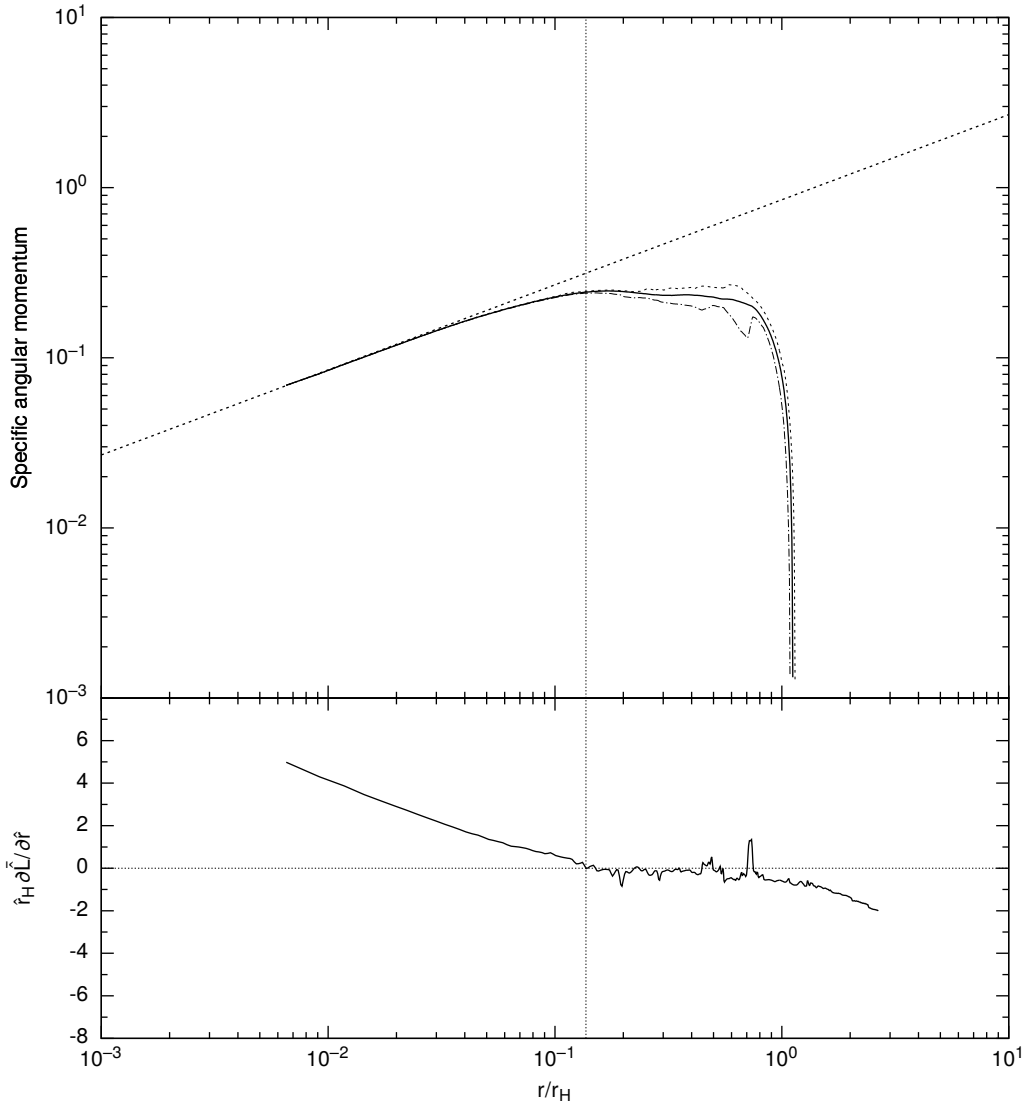

Figure 5.4. Same as in Figure 5.1, but for model with $\hat{r}_{\rm H} = 0.70$.

5.1.3 Density

Radial density profile, which is calculated as

$$\bar{\hat{\rho}}(\hat{r}) = \frac{\int_{-\pi}^{\pi} \int_{0}^{\Delta z} \int_{r-\Delta r/2}^{r+\Delta r/2} \hat{r}\hat{\rho} dr dz d\theta}{\int_{-\pi}^{\pi} \int_{0}^{\Delta z} \int_{r-\Delta r/2}^{r+\Delta r/2} dr dz d\theta} \tag{5.4}$$

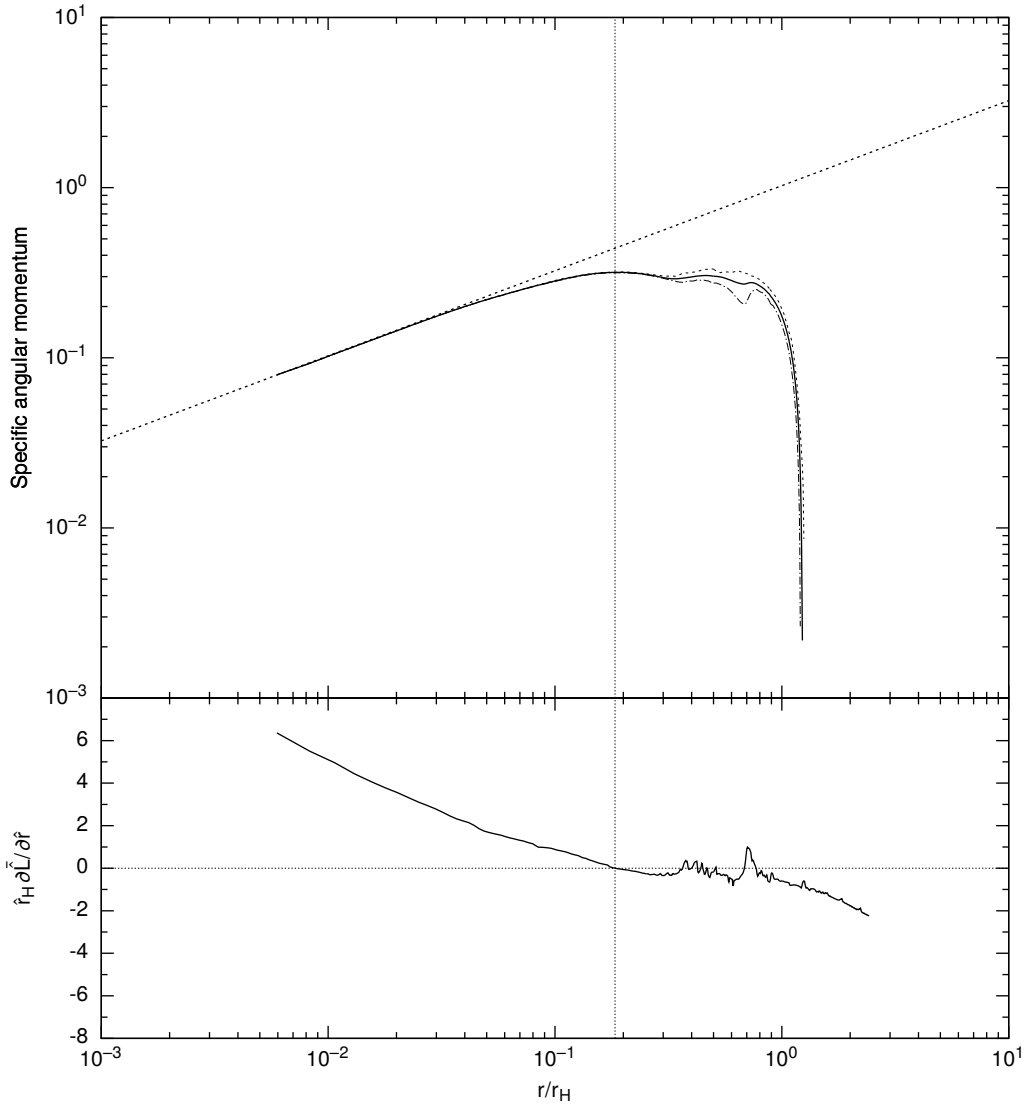

Figure 5.5. Same as in Figure 5.1, but for model with $\hat{r}_{\rm H} = 0.77$.

is shown in Figures 5.19 to 5.27. Each model has the same trend; the density has a peak in the inner Keplerian rotating region and gradually decreases outward. The fluctuations in density profile spread as the distance from the protoplanet increase. This indicates that the fluctuation is excited due to the time variation of the removing mass by the sink cell. A clear boundary between the circumplanetary disk and the turbulent region can not be confirmed in the density profile. Thus, it is concluded that the velocity distribution, not the density distribution should be used to identify

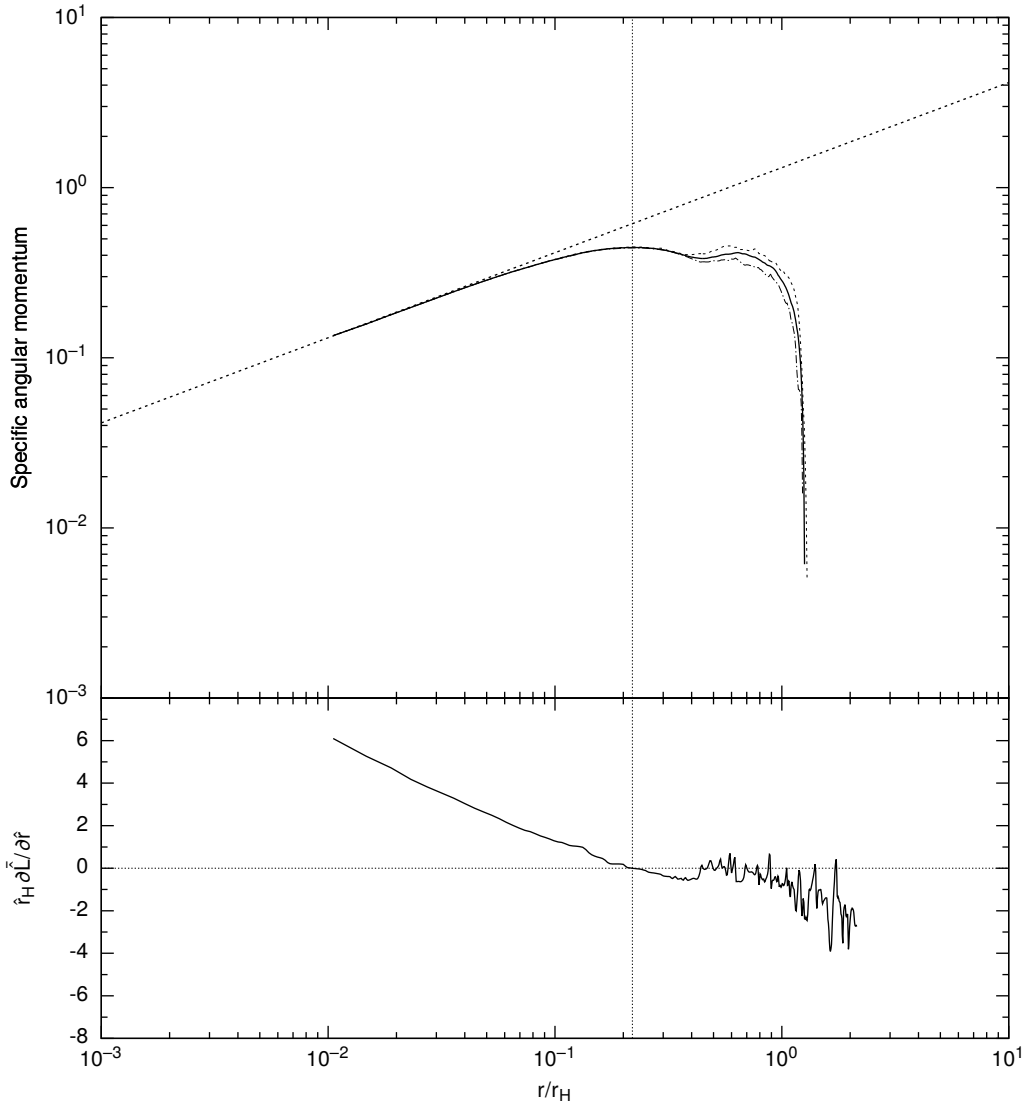

Figure 5.6. Same as in Figure 5.1, but for model with $\hat{r}_{\rm H} = 0.87$.

the circumplanetary disk.

5.2 Stable disk region

Although the convergence of surface density in models with large $\hat{r}_{\rm H}$ was not clearly confirmed in the region far from the protoplanet, the averaged azimuthal velocity on the midplane shows well convergence in all models. In addition, I confirmed that the high density region is highly stable and rarely changes with time. In order to confirm

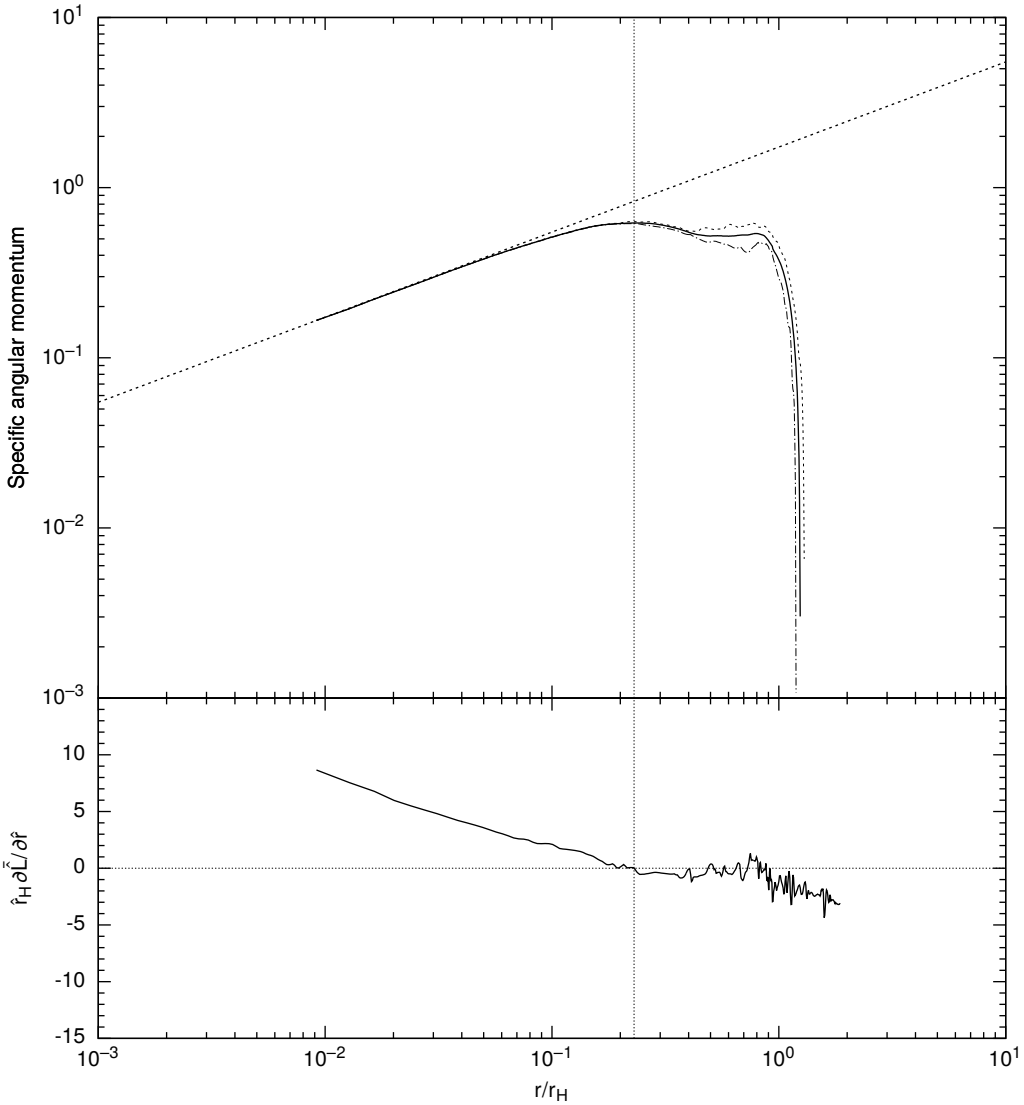

Figure 5.7. Same as in Figure 5.1, but for model with $\hat{r}_{\rm H} = 1.00$.

the radial dependence of the disk stability, the radial distribution of the averaged specific angular momentum which is normalized by the Keplerian angular momentum, and the fluctuations of the averaged specific angular momentum are shown in Figures 5.28 to 5.36. The fluctuation corresponds to the difference between the time averaged values and maximum, or minimum during one orbital period, in which the azimuthal velocity is averaged in the azimuthal direction. In each panel, the vertical dotted line indicates the radius at which the velocity corresponds to 0.95, 0.9, 0.8, 0.7, 0.6, and

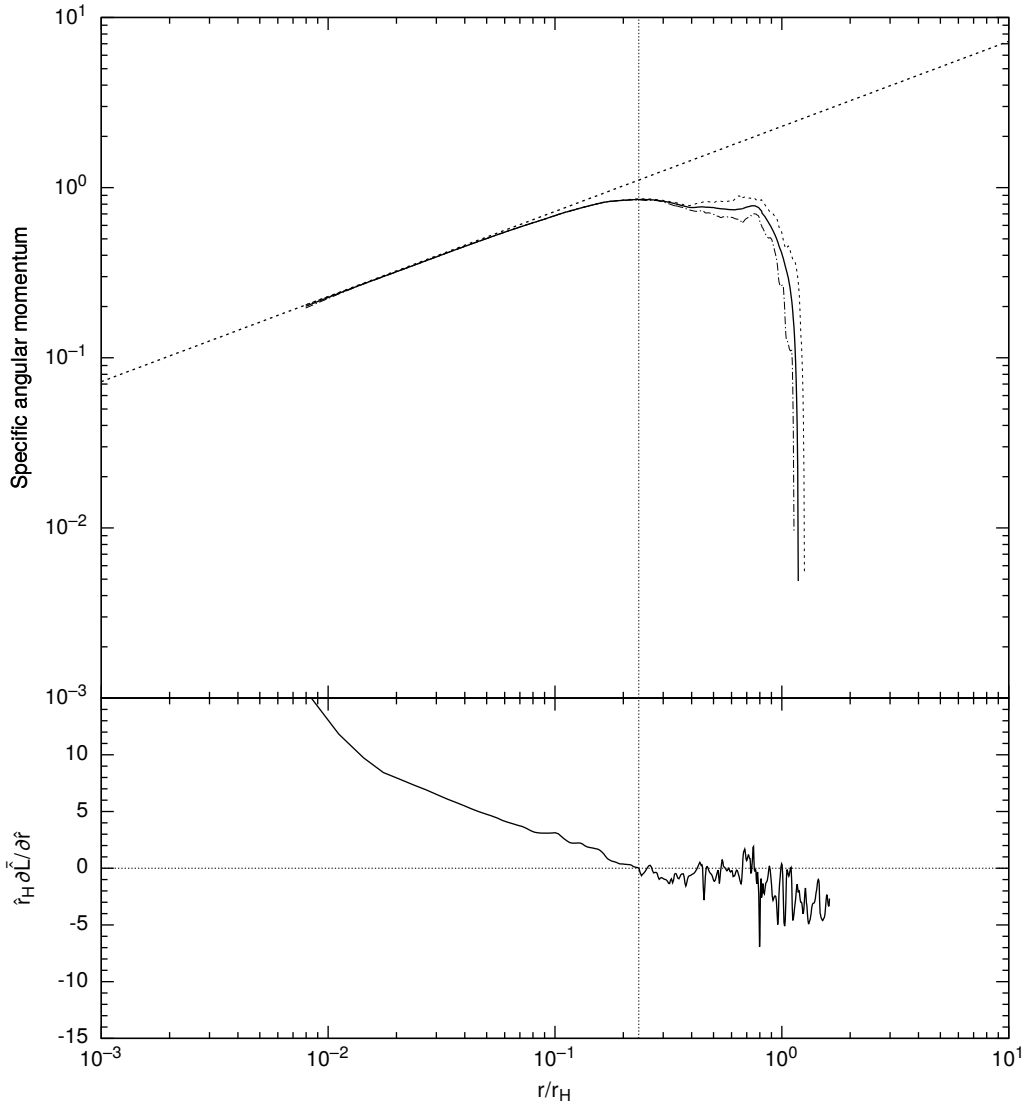

Figure 5.8. Same as in Figure 5.1, but for model with $\hat{r}_{\rm H} = 1.15$.

0.5 times the Keplerian velocity, $v_{\rm Kep}$.

For models with $\hat{r}_{\rm H} = 0.36$ and $\hat{r}_{\rm H} = 0.54$ (Figures 5.28 and 5.29), both the positive and negative fluctuations continue to increase as the normalized animuthal velocity decreases. However, for model with $\hat{r}_{\rm H} = 0.64$, only the positive fluctuation exists and begins to increase at $\sim 0.6 v_{\rm Kep}$. The increase rate of the fluctuation is amplified as the radius increases. Figure 5.31 also shows the moderate increase of the fluctuation, which is apparent in the regoion at $v_\theta \sim 0.95 v_{\rm Kep}$. In addition, for this model,

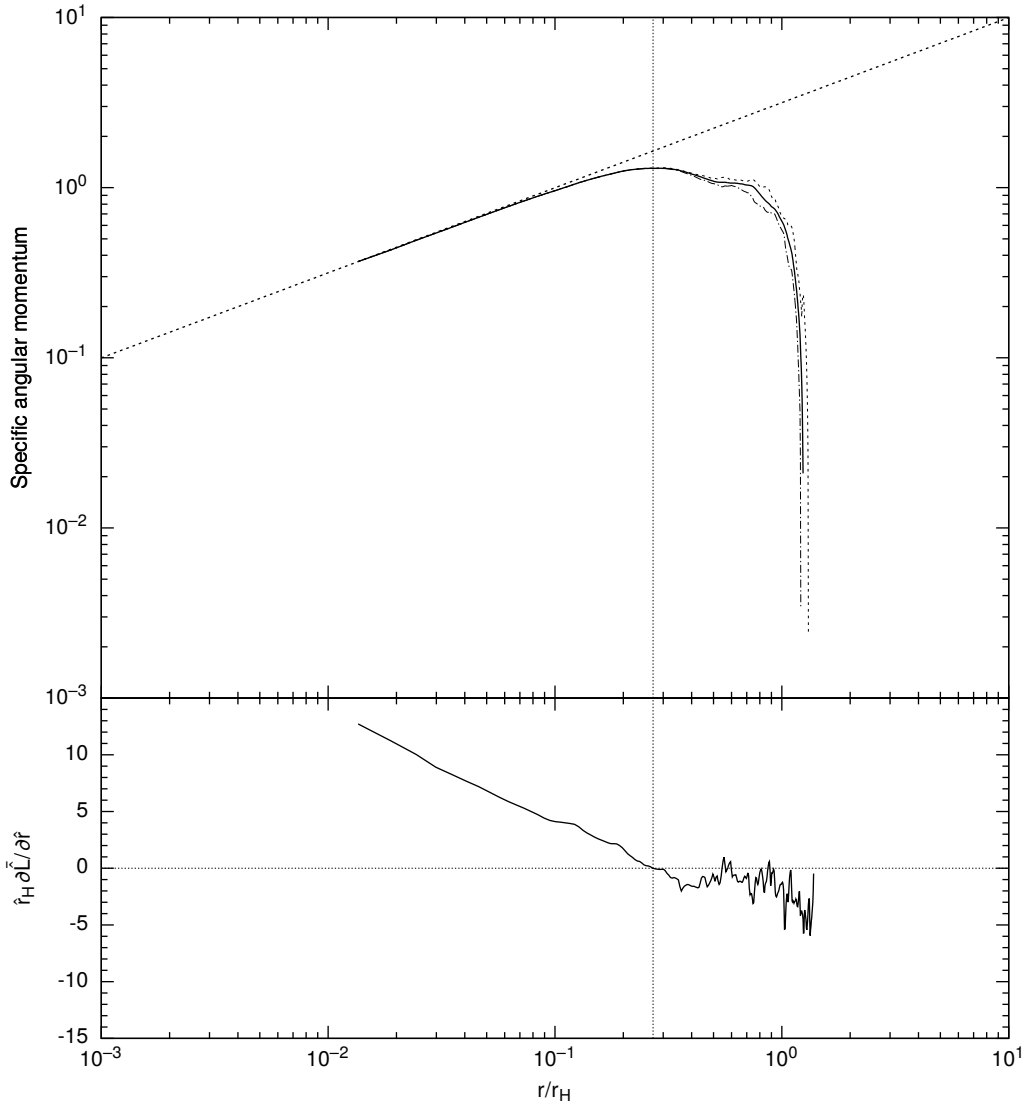

Figure 5.9. Same as in Figure 5.1, but for model with $\hat{r}_{\rm H} = 1.35$.

the fluctuation in the nomarlized azimuthal velocity is rapidly amplified between $0.80 v_{\rm Kep} < v_\theta < 0.50 v_{\rm Kep}$.

For model with $\hat{r}_{\rm H} \geq 0.77$, the region, in which fluctuations increase, can be clearly divided into three regions: the region has (i) an almost Keplerian motion inside the radius $v_\theta = 0.95 v_{\rm Kep}$, (ii) a constant amplitudes of fluctuation from the radii $v_\theta = 0.95 v_{\rm Kep}$ to $v_\theta = 0.50 v_{\rm Kep}$, and (iii) a large increasing fluctuation in the outer region. The constant amplitude section and the outer highly fluctuated regions are

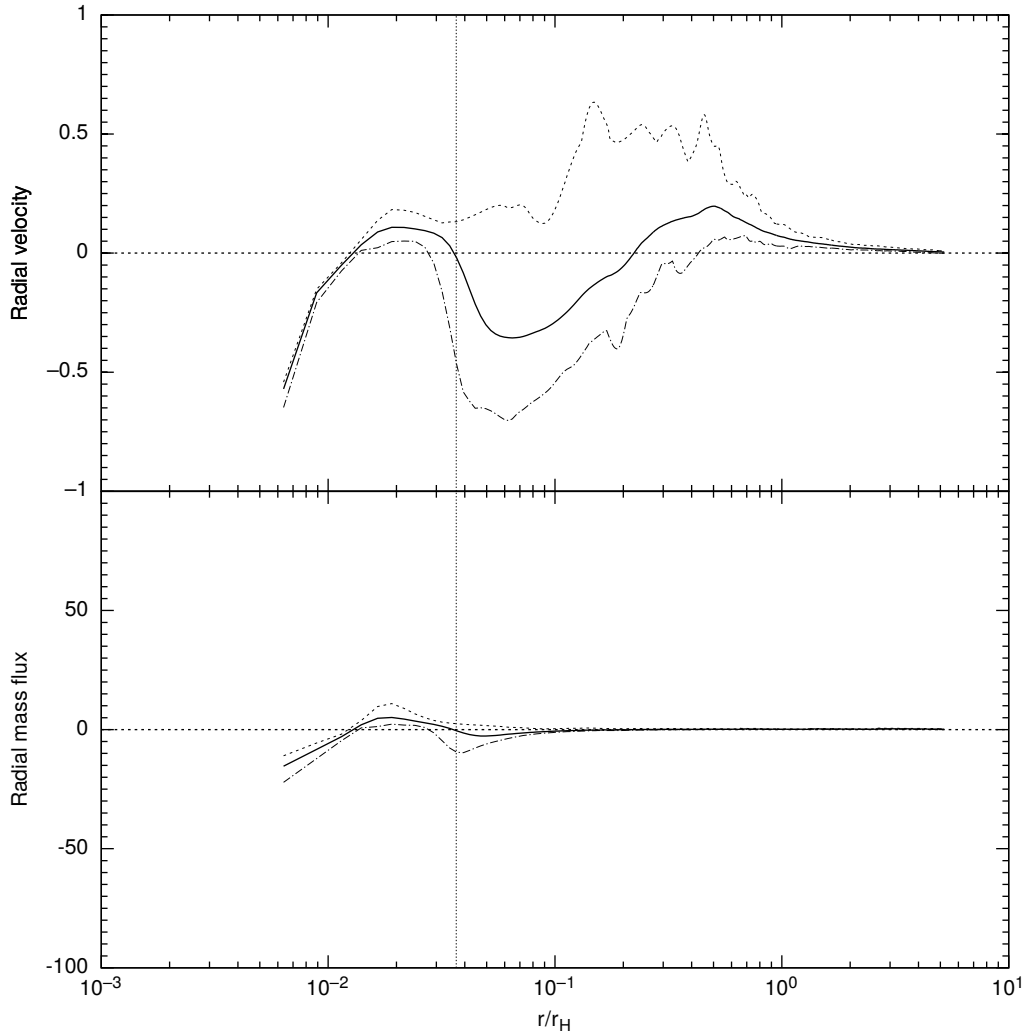

Figure 5.10. Averaged non-dimensional radial velocity and radial mass flux for model with $\hat{r}_{\rm H} = 0.36$. Solid, dashed, and dash-dotted lines are time averaged, maxima and minima of each quantity during one orbital period, respectively. The vertical dotted line is the position of $\partial L/\partial r = 0$ as in Figure 5.1.

generally seen in Figures 5.32, 5.33, 5.34, 5.35, and 5.36. Notably, the outer fluctuated region is clearly seen in the top panel of the figures in which the fluctuation in the outer region is obviously larger than that in the inner region. The transition to the fluctuated region from the stable region occurs in $\hat{r} = 0.3$ to 0.5 approximately.

Thus, the region of radius in the range of $v_\theta = 0.95 v_{\rm Kep}$ to $v_\theta = 0.80 v_{\rm Kep}$ may be able to determine the region which is assumed to be a Keplerian rotating disk. On the other hand, the radius in the range of $v_\theta = 0.70 v_{\rm Kep}$ to $v_\theta = 0.50 v_{\rm Kep}$ may be regarded as the transitional region.

5.3 Scaling

In previous chapter, I showed two types of characteristic radius of the circumplanetary disk. One is a qualitative boundary where the gradient of radial angular momentum becomes zero, which is hereafter described as $\hat{r}_c$. The radius $\hat{r}_c$ corresponds to the outer edge of the circumplanetary disk. This radius is plotted against the normalized Hill radius (i.e., against each model) in Figure 5.37, in which the fitting of $\hat{r}_c$ is also plotted. The fitting formula is described in the caption. In the figure, two triangles are plotted in order to compare the standard models with the different models which have different spatial resolutions. The parameters for models H064R7 ($l_{\rm max} = 7$) and H064R9 ($l_{\rm max} = 9$) are listed in Table 3.2. The triangles located at the upper and lower position correspond to the models with $l_{\rm max} = 7$ and $l_{\rm max} = 9$, respectively. The figure indicates that the higher spatial resolution results in a smaller radius of circumplanetary disk. From this figure we can see that the power law function well traces the simulation result.

Another characteristic radius is defined by the azimuthal velocity normalized by the Keplerian velocity. Figures 5.38, 5.39, 5.40, 5.41, 5.42, and 5.43 show the radii respect to the normalized Hill radius $\hat{r}_{\rm H}$, in which the criteria of normalized velocity is different and has, respectively, $v_\theta / v_{Kep} = 0.95$, 0.9, 0.8, 0.7, 0.6, and 0.5 in each figure. The approximated power-low function is also plotted in these figures. The figures show that the critical radius of each model is well described by the fitting formula. However, some differences between calculation results and fitting formulae are seen especially in models with smaller $\hat{r}_{\rm H}$.

I adopted the radius at $v_\theta / v_{Kep} = 0.80$ (Figure 5.40) as the characteristic ra-

Table 5.1. Circumplanetary disk radius taken from this study and the parameters of planets and their satellite in the solar system. The radii are approximated by the function $0.19279764757795 \times \hat{r}_{\rm H}^{2.36023412285795}$, which is derived from $\bar{v}_\theta(r_{CPD})/v_{Kep} = 0.80$.

Planet	Mass[M_{Jup}]	r_p [AU]	$\hat{r}_{Hill}$	r_{CPD} [km]	Satellite	r_{sat}[km]
Jupiter	5.203	1.00	1.35	1.541×10^7	Himalia	1.146×10^7
Saturn	9.555	0.299	0.78	8.911×10^6	Iapetus	3.56×10^6
Uranus	19.218	0.0457	0.35	3.223×10^6	Oberon	5.84×10^5
Neptune	30.11	0.0540	0.33	4.938×10^6	Nereid	5.513×10^6

dius of the circumplanetary disk, because the simulation results fit well with the power law functions. In addition, this radius agrees well with the radius defined by $\partial L(\hat{r}_c)/\partial r = 0$ (the former one; Figure 5.37). Applying the approximate function for the parameters of present solar system, we can estimate the circumplanetary disk radius of each planet. The estimated radius and orbital radius of an outer regular satellite is summarized in Table 5.1 as a reference for each giant planet. In the cases of Jupiter, Saturn and Neptune, the satellite orbital radius is consistent with the estimated circumplanetary disk radius. On the other hand, for the case of Uranus, $r_{\rm sat}$ is an order of magnitude smaller than the estimated value, which may imply that Uranus had migrated from the inner orbital radius, or the outer satellites are scattered due to the gravitational interaction among the inner satellites.

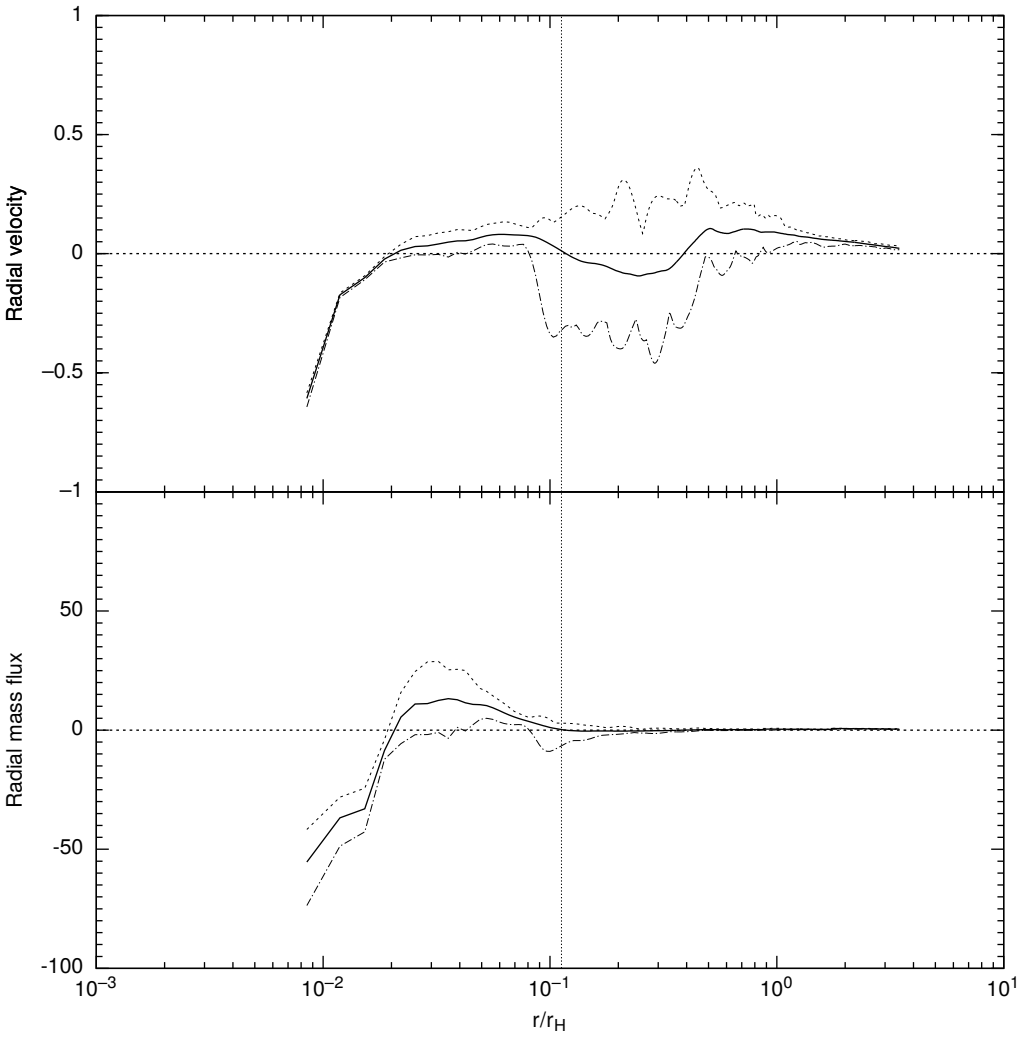

Figure 5.11. Same as Fig. 5.10, but for model with $\hat{r}_{\rm H} = 0.54$.

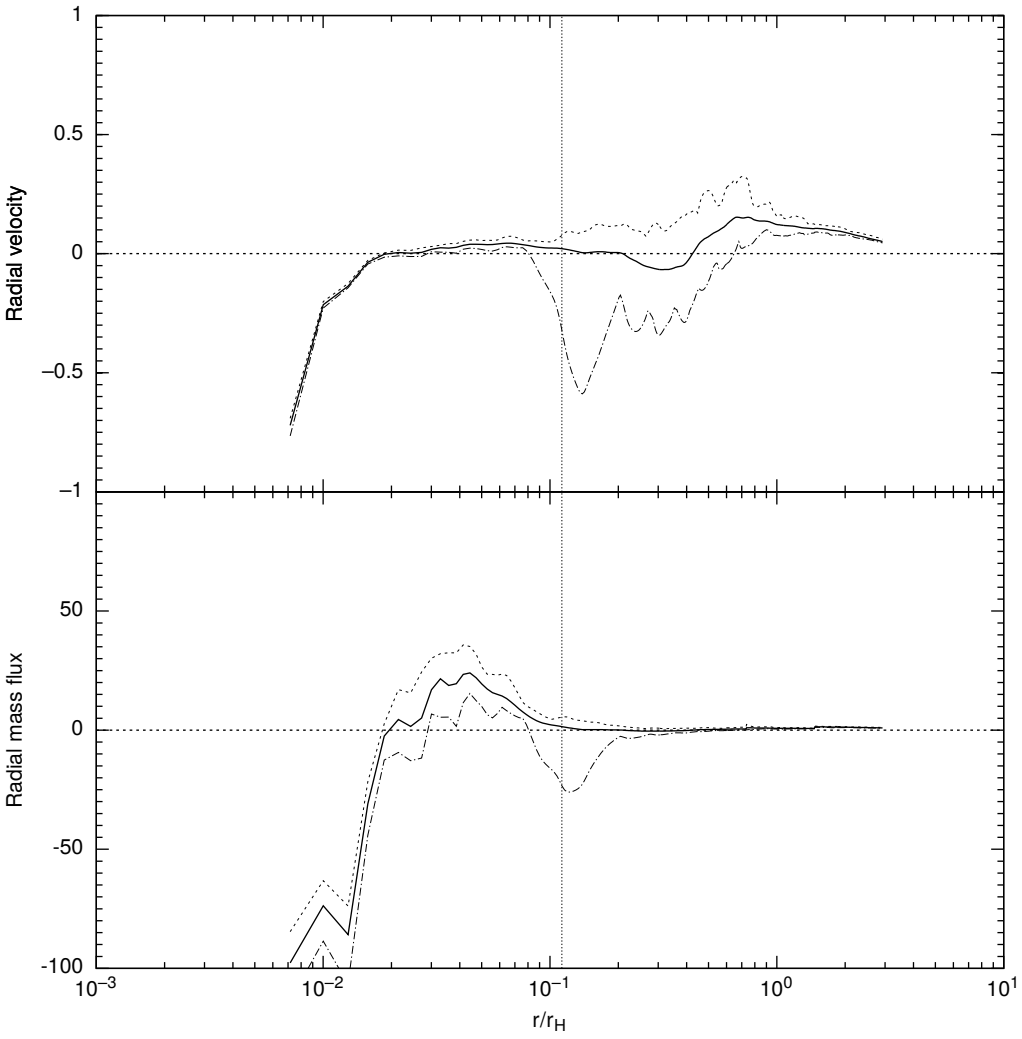

Figure 5.12. Same as Fig. 5.10, but for model with $\hat{r}_{\rm H} = 0.64$.

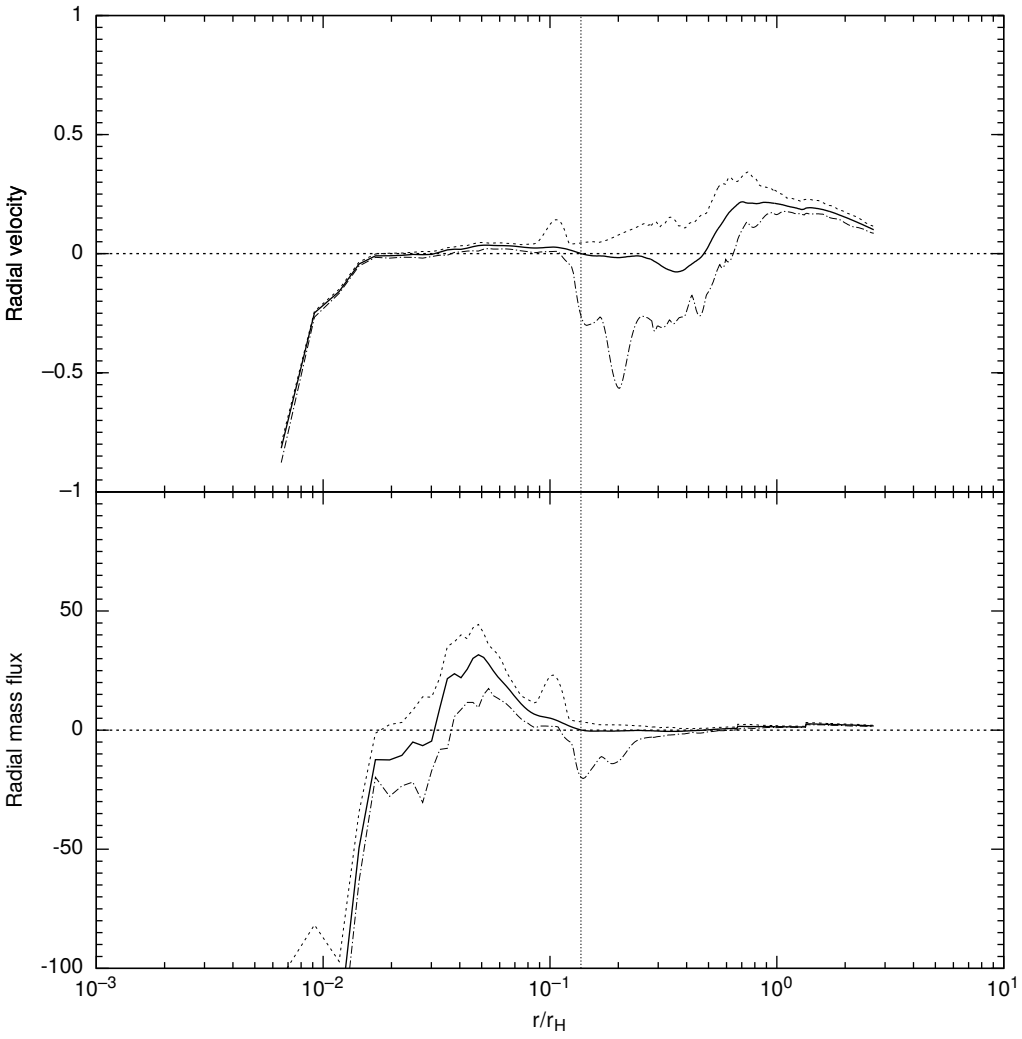

Figure 5.13. Same as Fig. 5.10, but for model with $\hat{r}_{\rm H} = 0.70$.

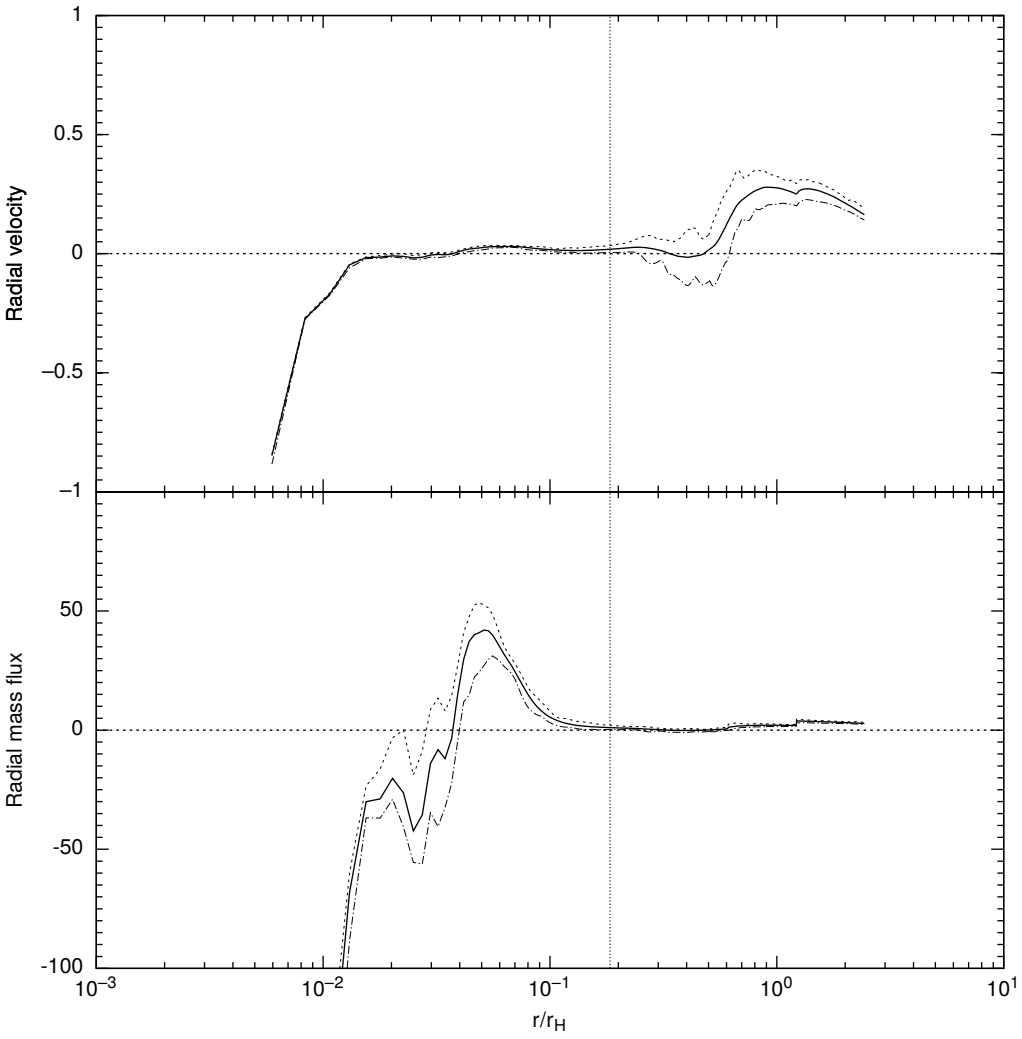

Figure 5.14. Same as Fig. 5.10, but for model with $\hat{r}_{\rm H} = 0.77$.

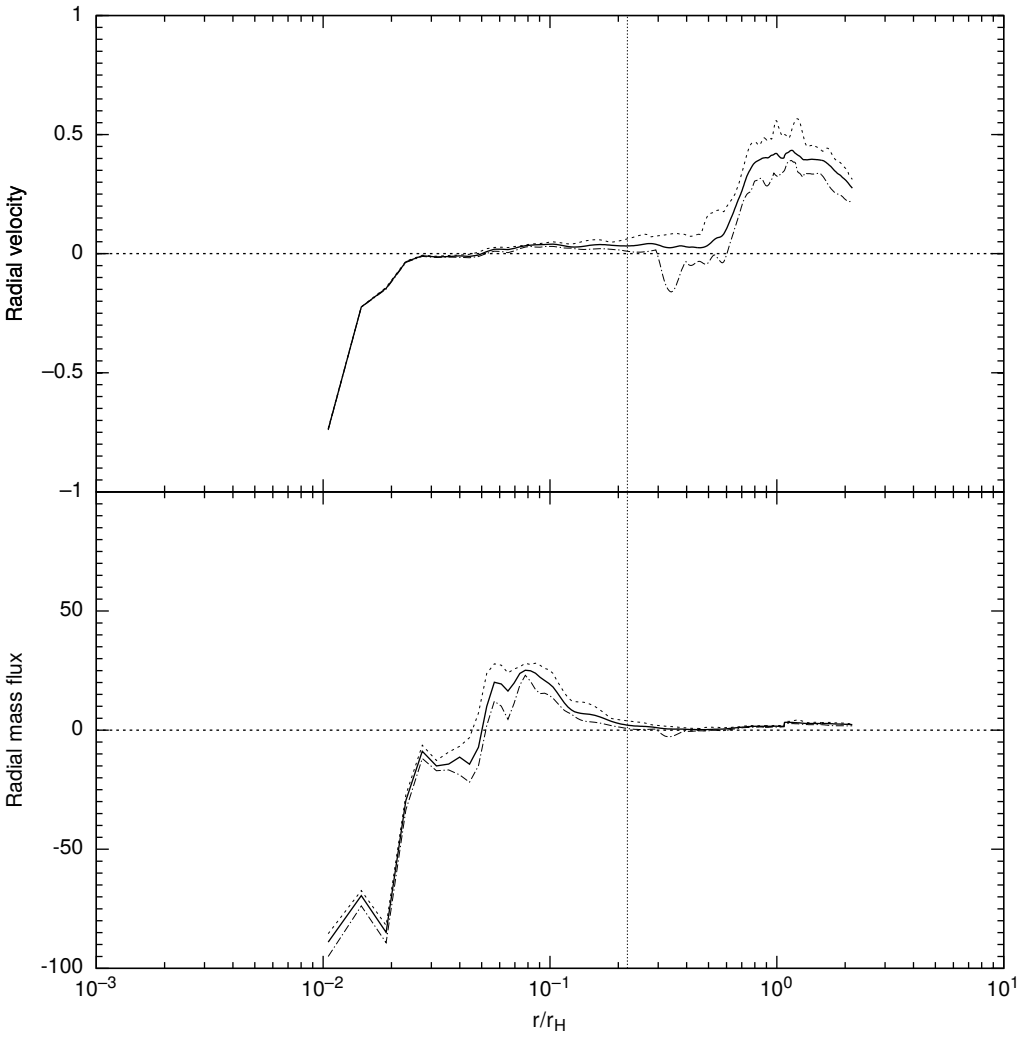

Figure 5.15. Same as Fig. 5.10, but for model with $\hat{r}_{\rm H} = 0.87$.

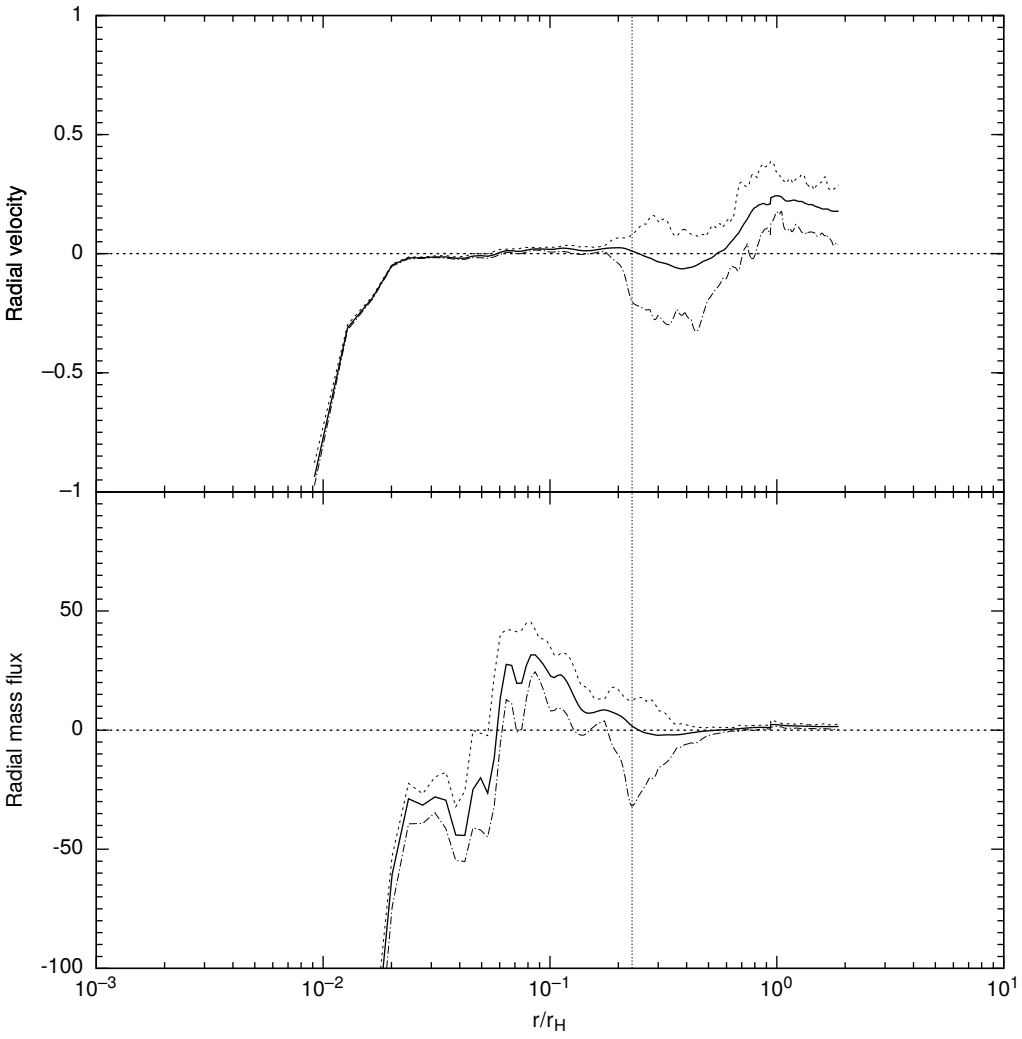

Figure 5.16. Same as Fig. 5.10, but for model with $\hat{r}_{\rm H} = 1.00$.

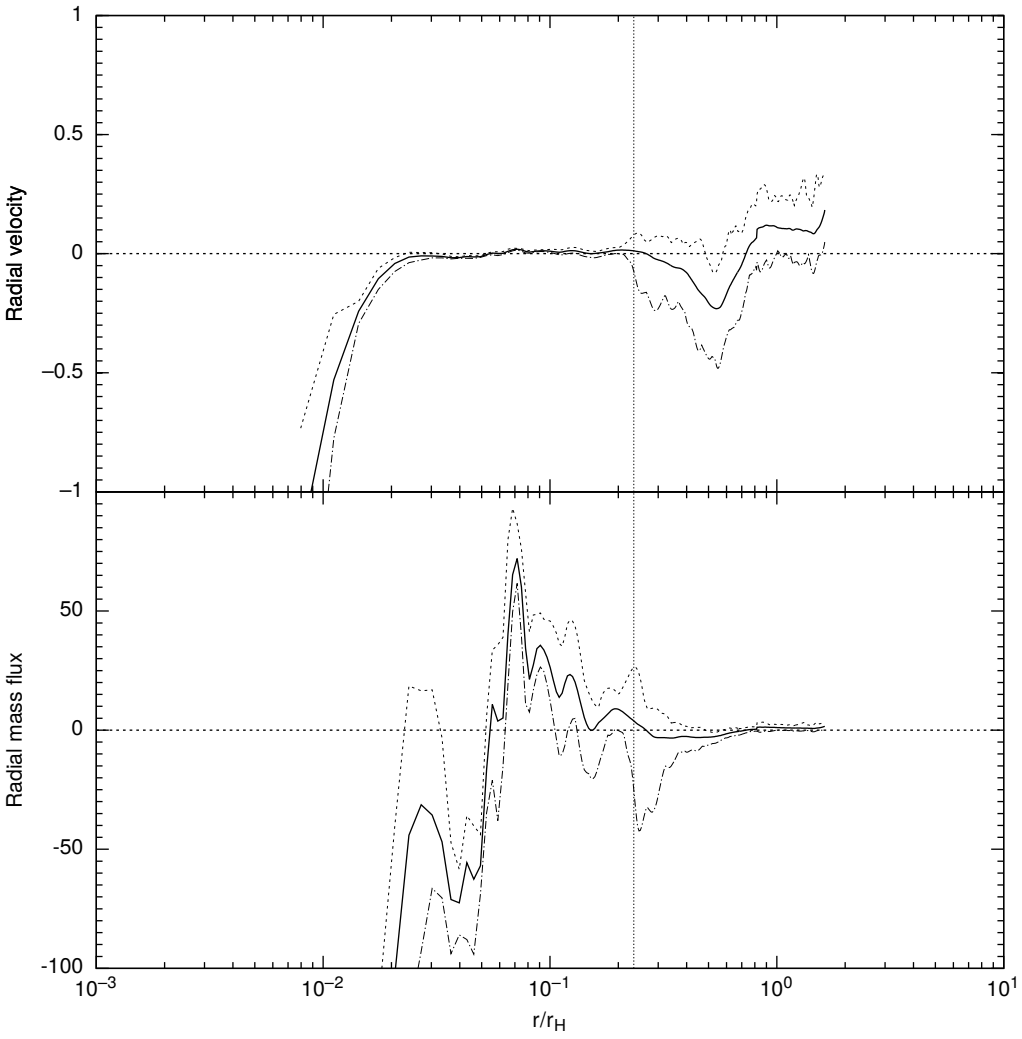

Figure 5.17. Same as Fig. 5.10, but for model with $\hat{r}_{\rm H} = 1.15$.

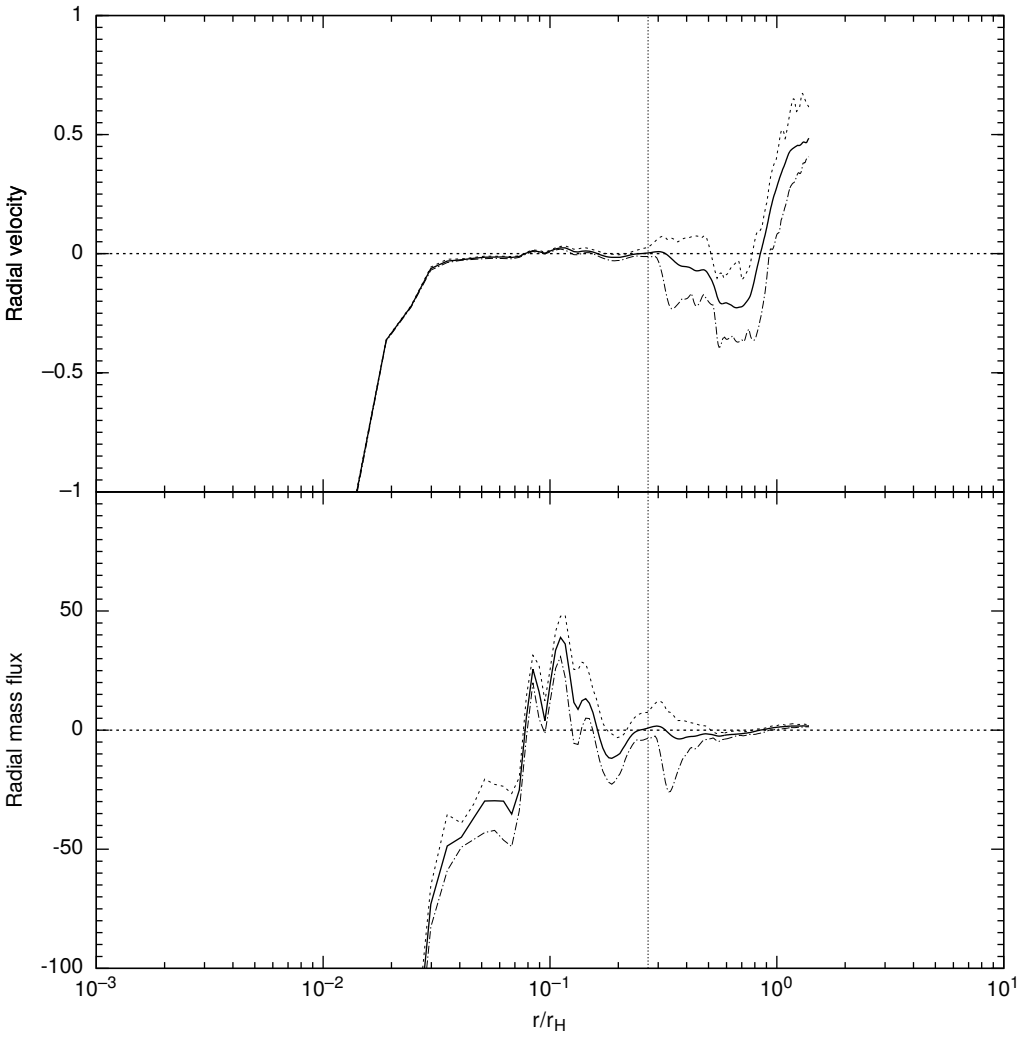

Figure 5.18. Same as Fig. 5.10, but for model with $\hat{r}_{\rm H} = 1.35$.

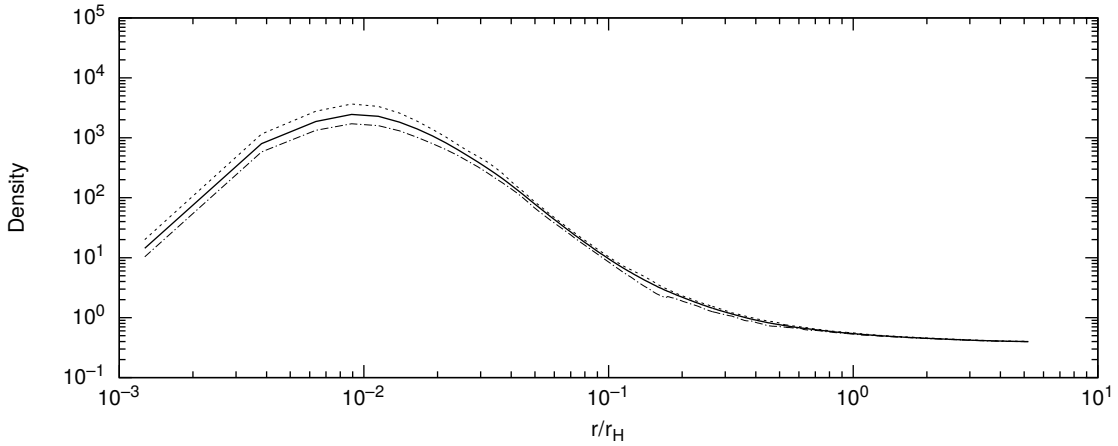

Figure 5.19. Radial profile of averaged density for model with $\hat{r}_{\rm H} = 0.36$. The solid, dashed, and dash-dotted line denotes time averaged, maxima, and minima during one orbital period after the steady state is realized around the protoplanet, respectively.

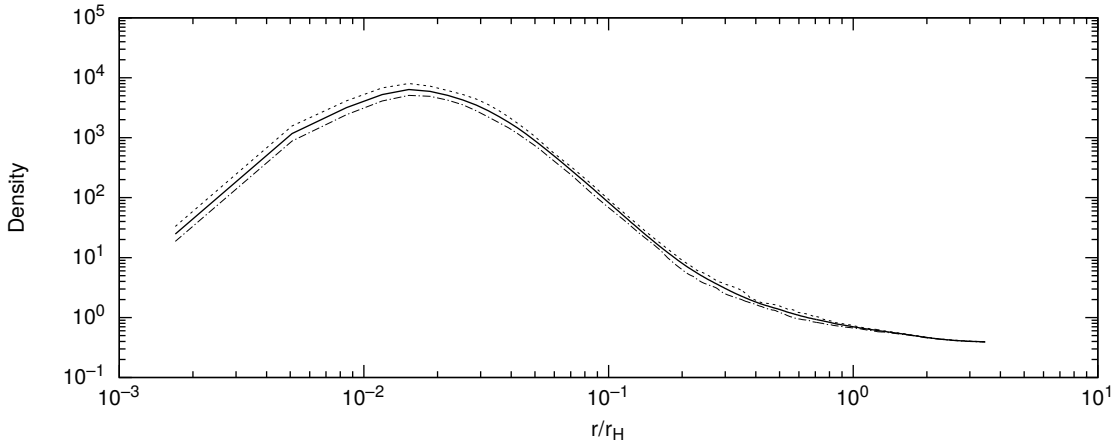

Figure 5.20. Same as in Fig. 5.19, but for model with $\hat{r}_{\rm H} = 0.54$.

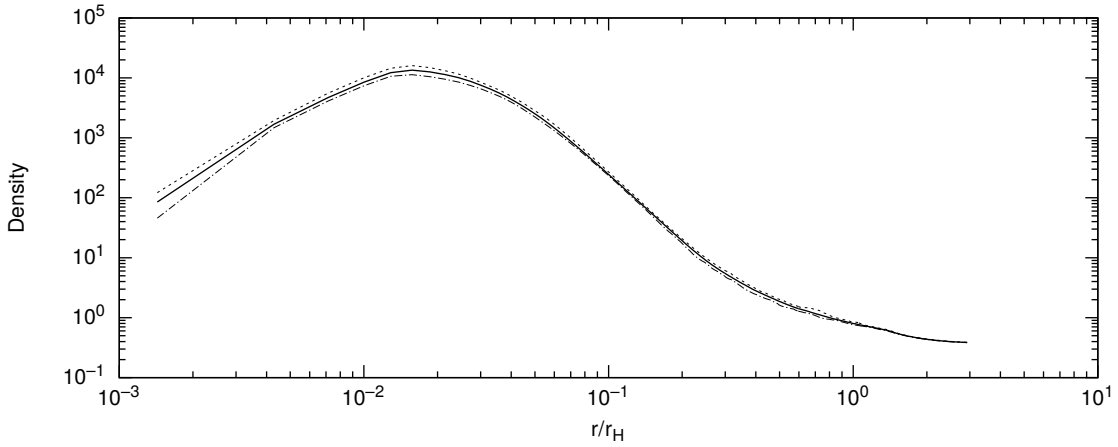

Figure 5.21. Same as in Fig. 5.19, but for model with $\hat{r}_{\rm H} = 0.64$.

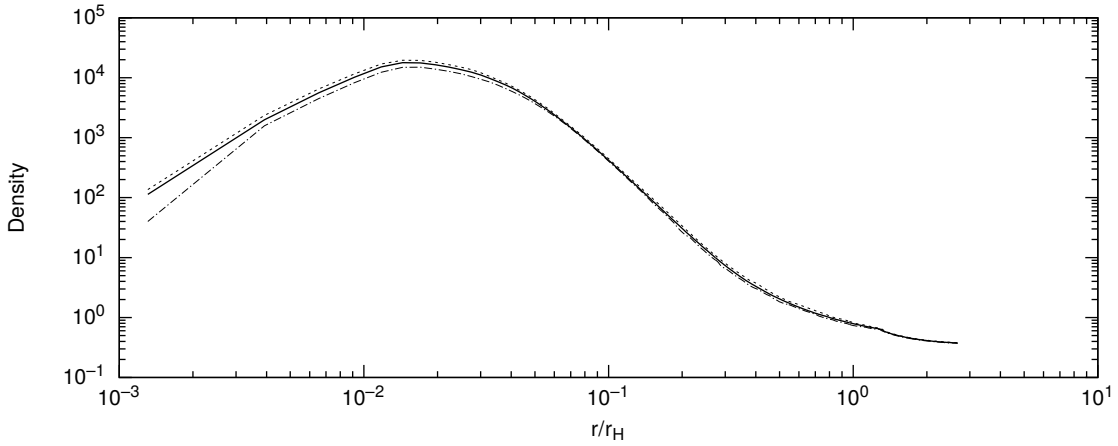

Figure 5.22. Same as in Fig. 5.19, but for model with $\hat{r}_{\rm H} = 0.70$.

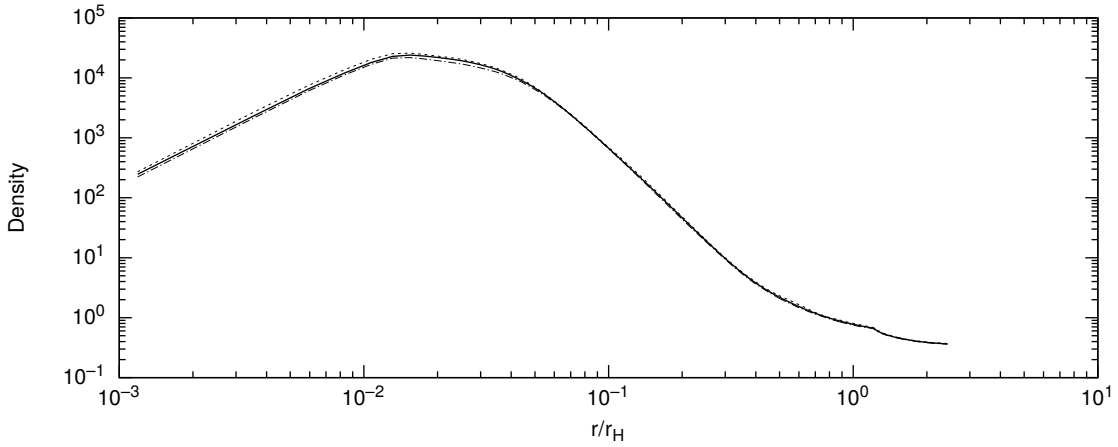

Figure 5.23. Same as in Fig. 5.19, but for model with $\hat{r}_{\rm H} = 0.77$.

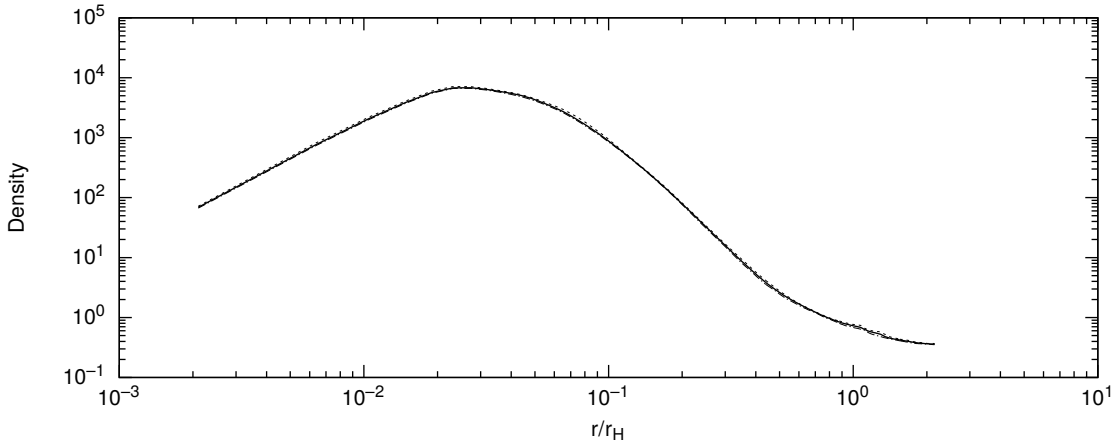

Figure 5.24. Same as in Fig. 5.19, but for model with $\hat{r}_{\rm H} = 0.87$.

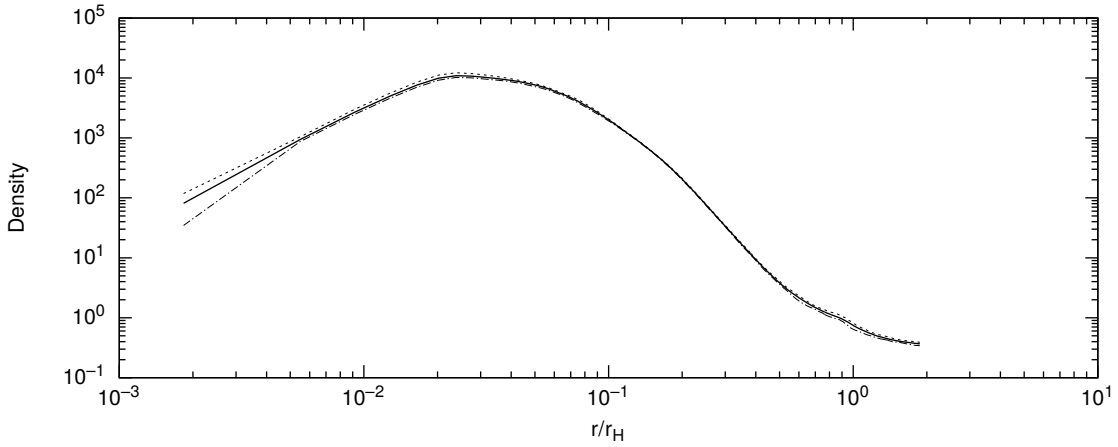

Figure 5.25. Same as in Fig. 5.19, but for model with $\hat{r}_{\rm H} = 1.00$.

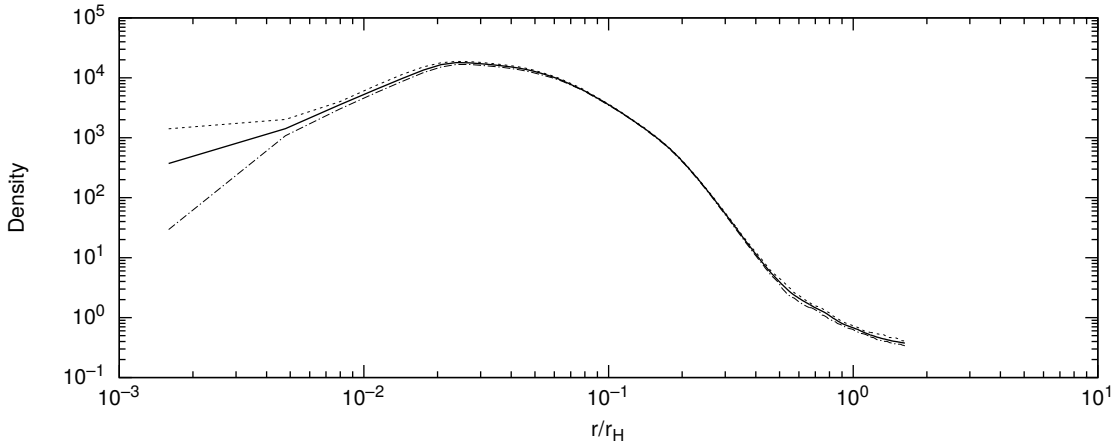

Figure 5.26. Same as in Fig. 5.19, but for model with $\hat{r}_{\rm H} = 1.15$.

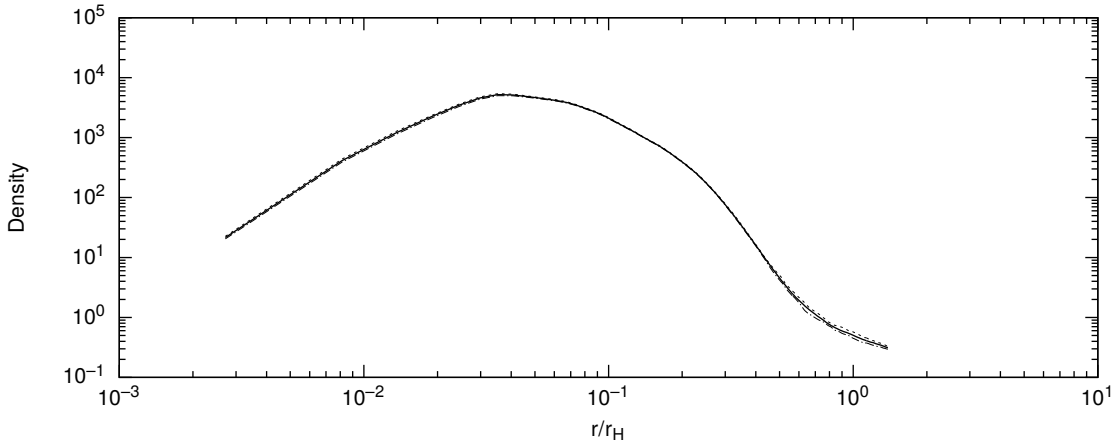

Figure 5.27. Same as in Fig. 5.19, but for model with $\hat{r}_{\rm H} = 1.35$.

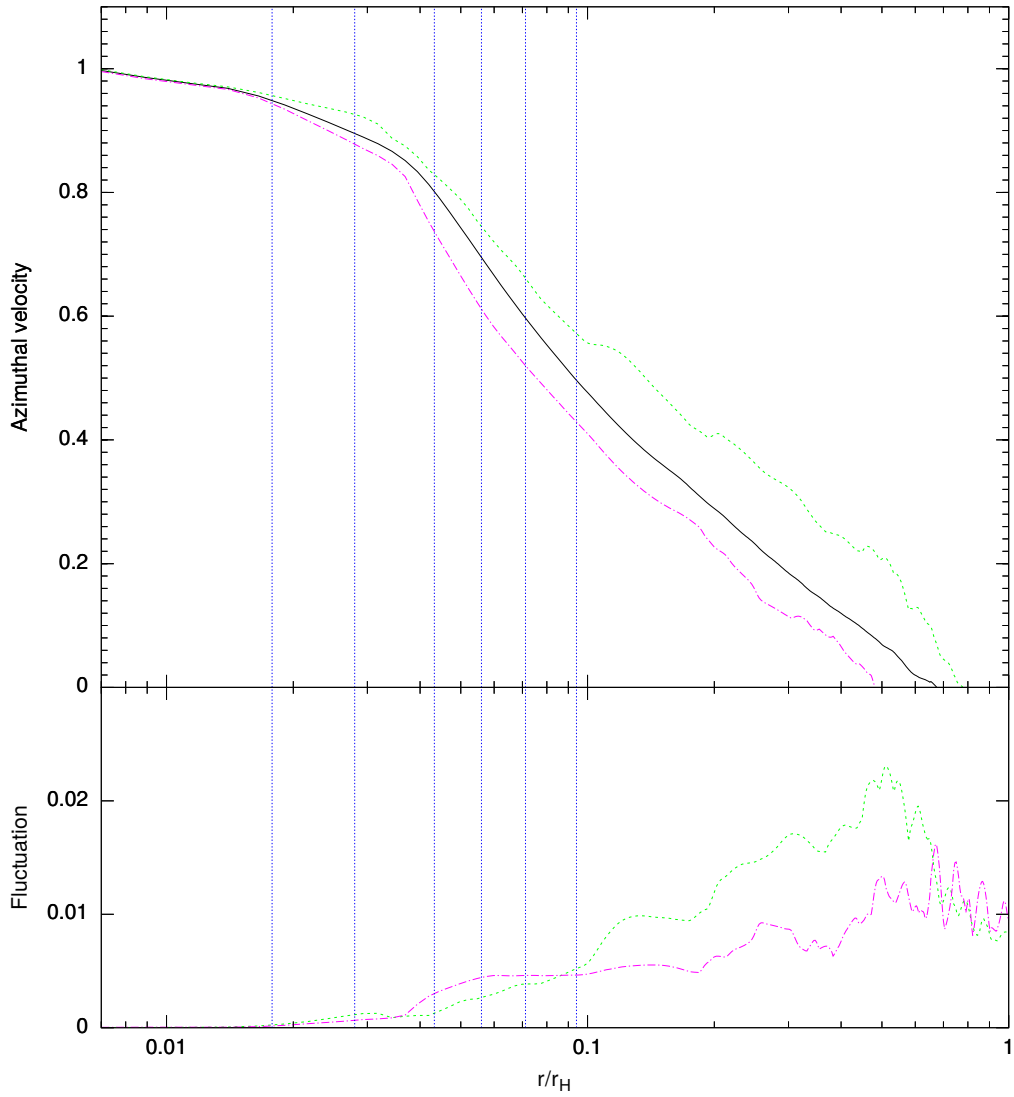

Figure 5.28. Time averaged radial profile of the azimuthal velocity for model with $\hat{r}_{\rm H} = 0.36$ normalized by the Keplerian angular velocity. The profiles are also averaged in the azimuthal direction during one orbital period.

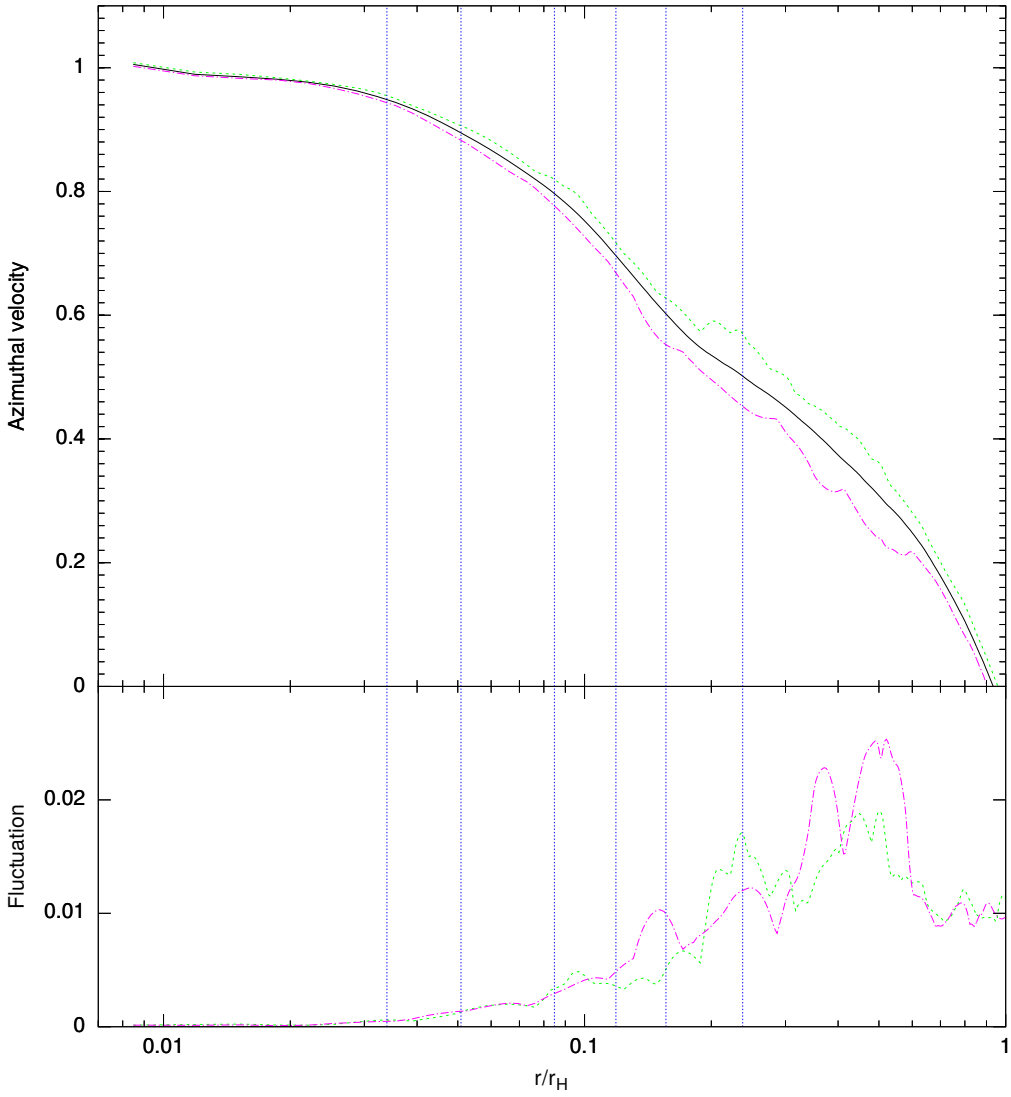

Figure 5.29. Same as in Figure 5.28, but for model with $\hat{r}_{\rm H} = 0.54$.

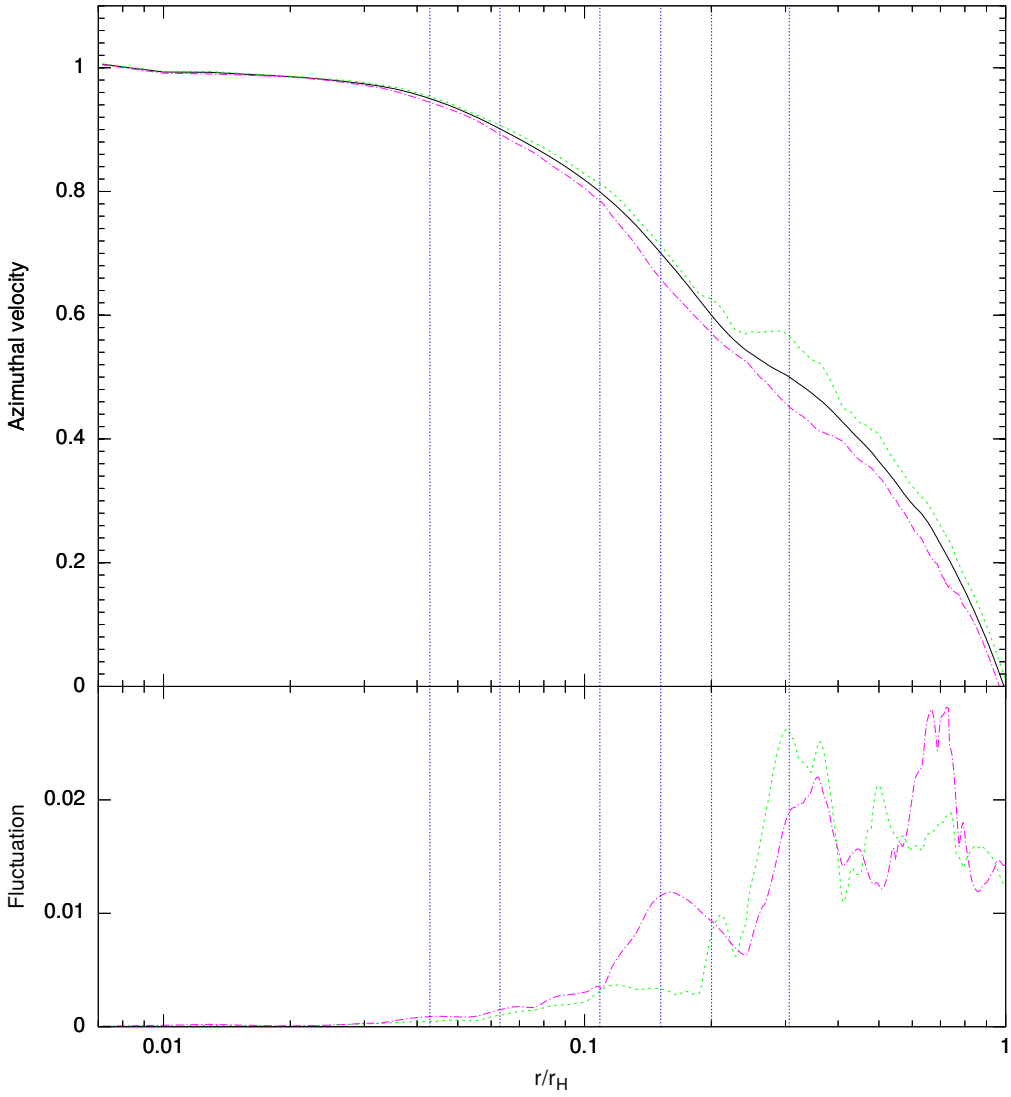

Figure 5.30. Same as in Figure 5.28, but for model with $\hat{r}_{\rm H} = 0.64$.

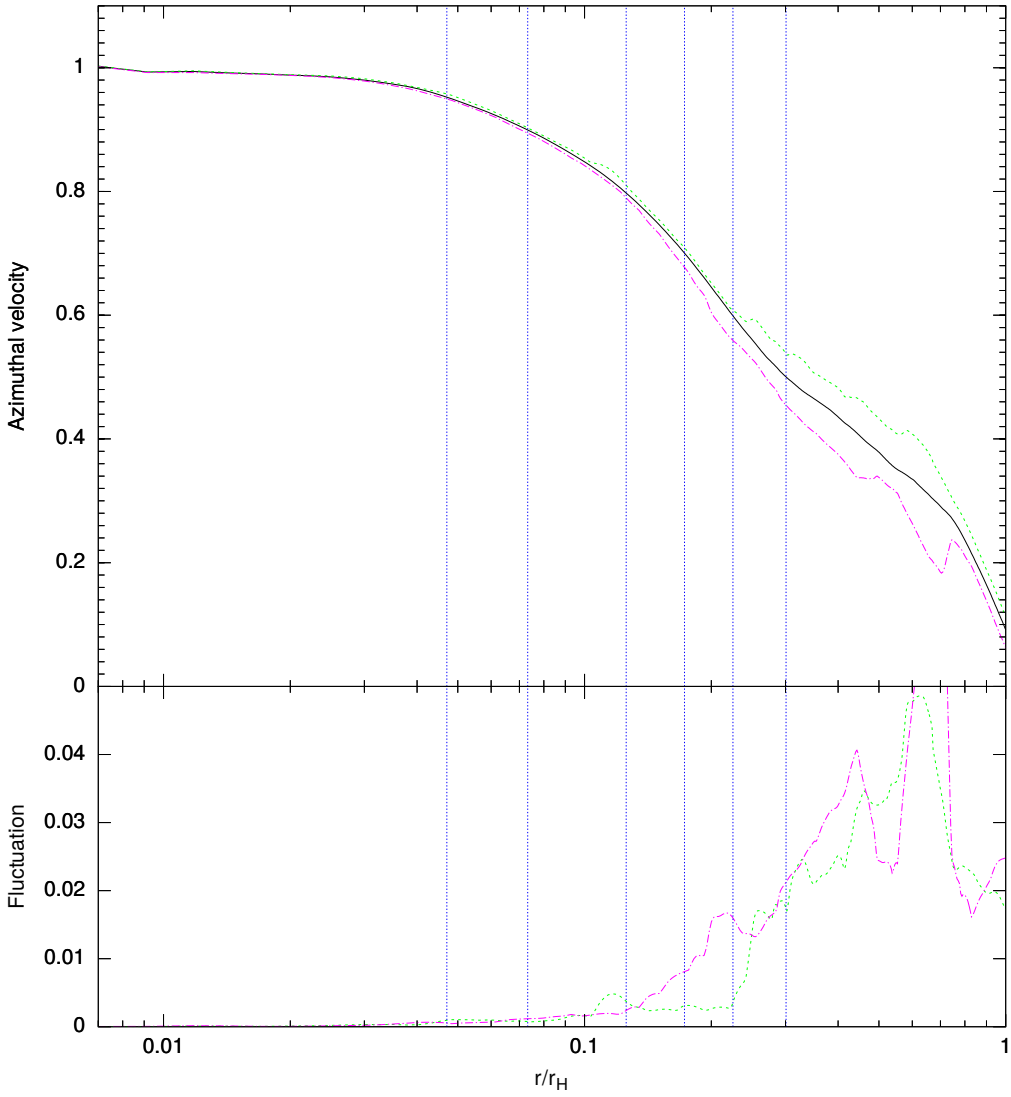

Figure 5.31. Same as in Figure 5.28, but for model with $\hat{r}_{\rm H} = 0.70$.

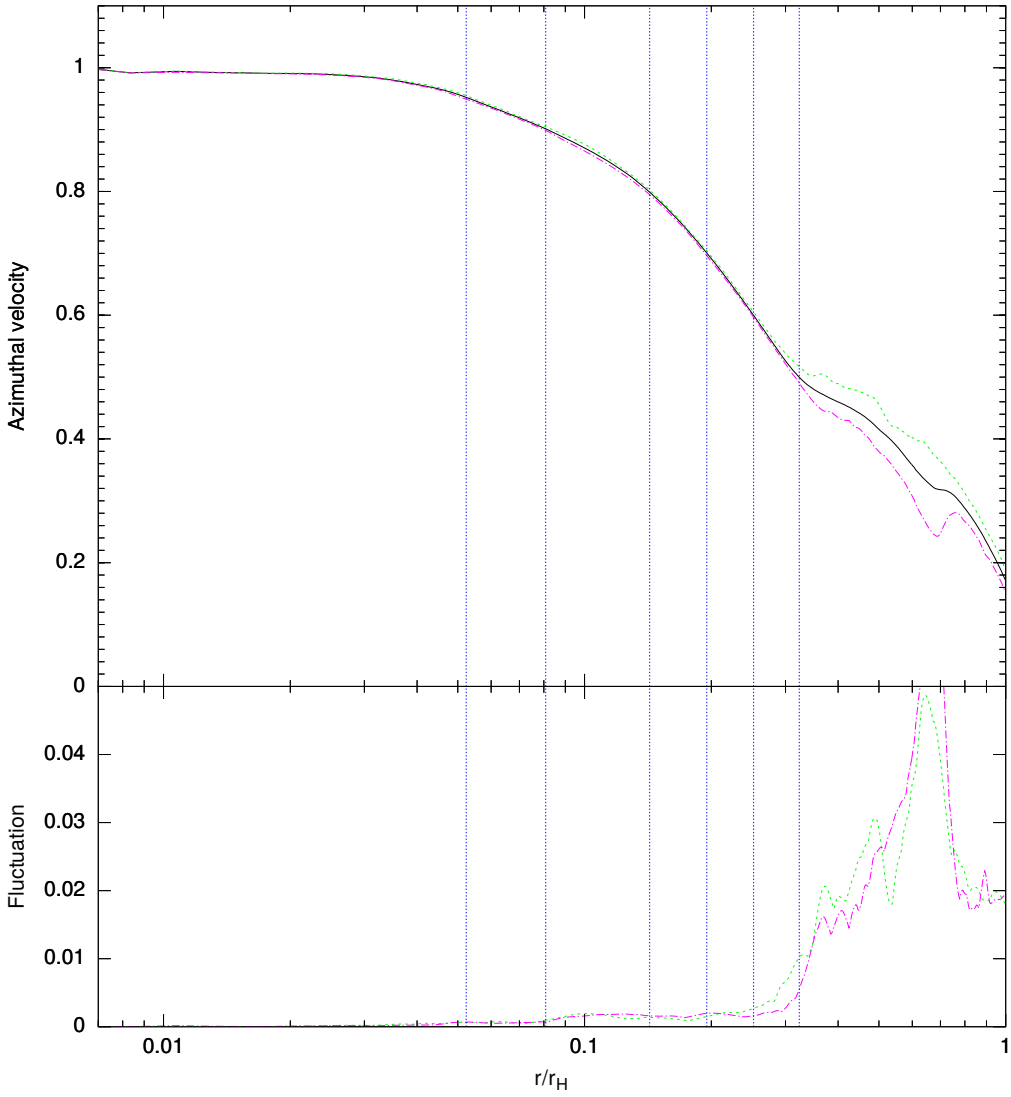

Figure 5.32. Same as in Figure 5.28, but for model with $\hat{r}_{\rm H} = 0.77$.

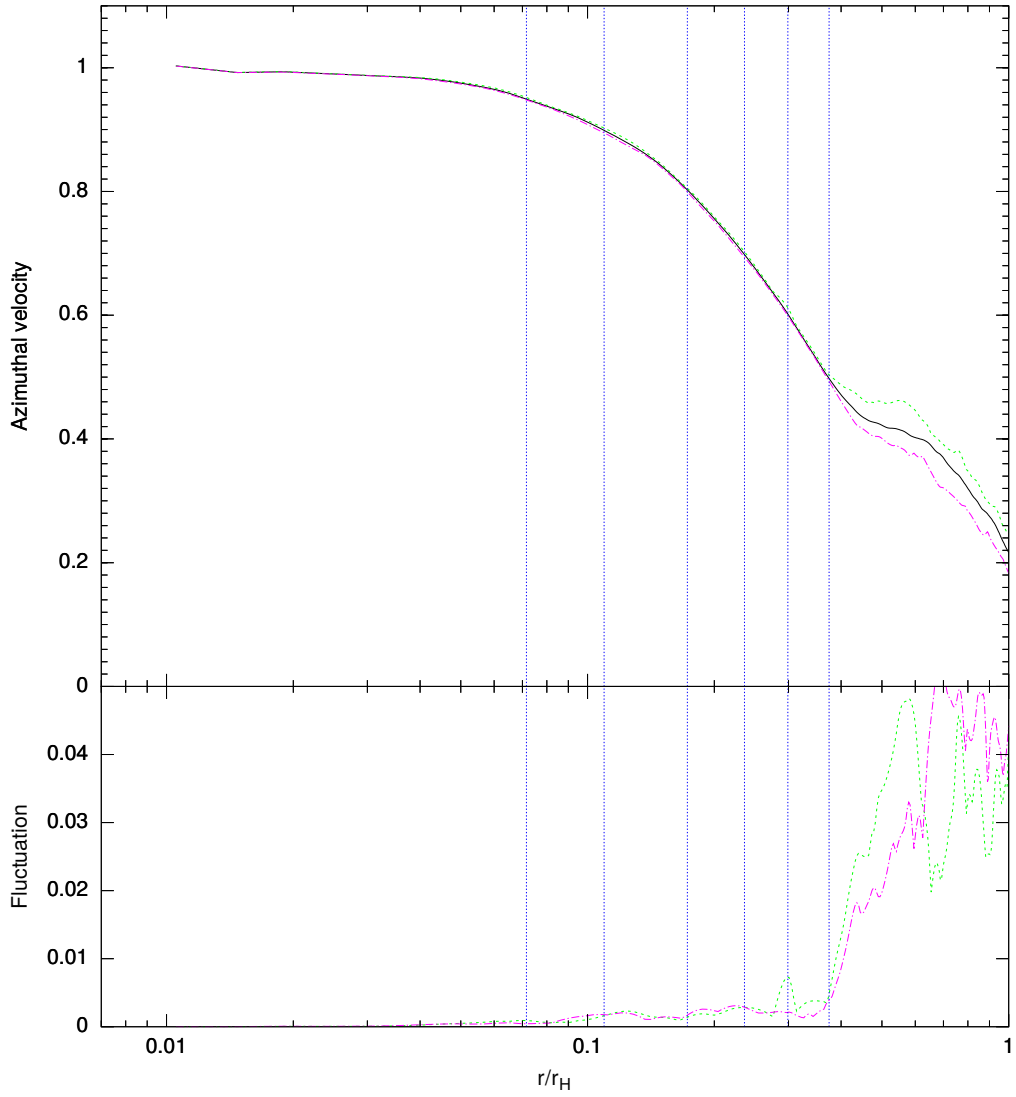

Figure 5.33. Same as in Figure 5.28, but for model with $\hat{r}_{\rm H} = 0.87$.

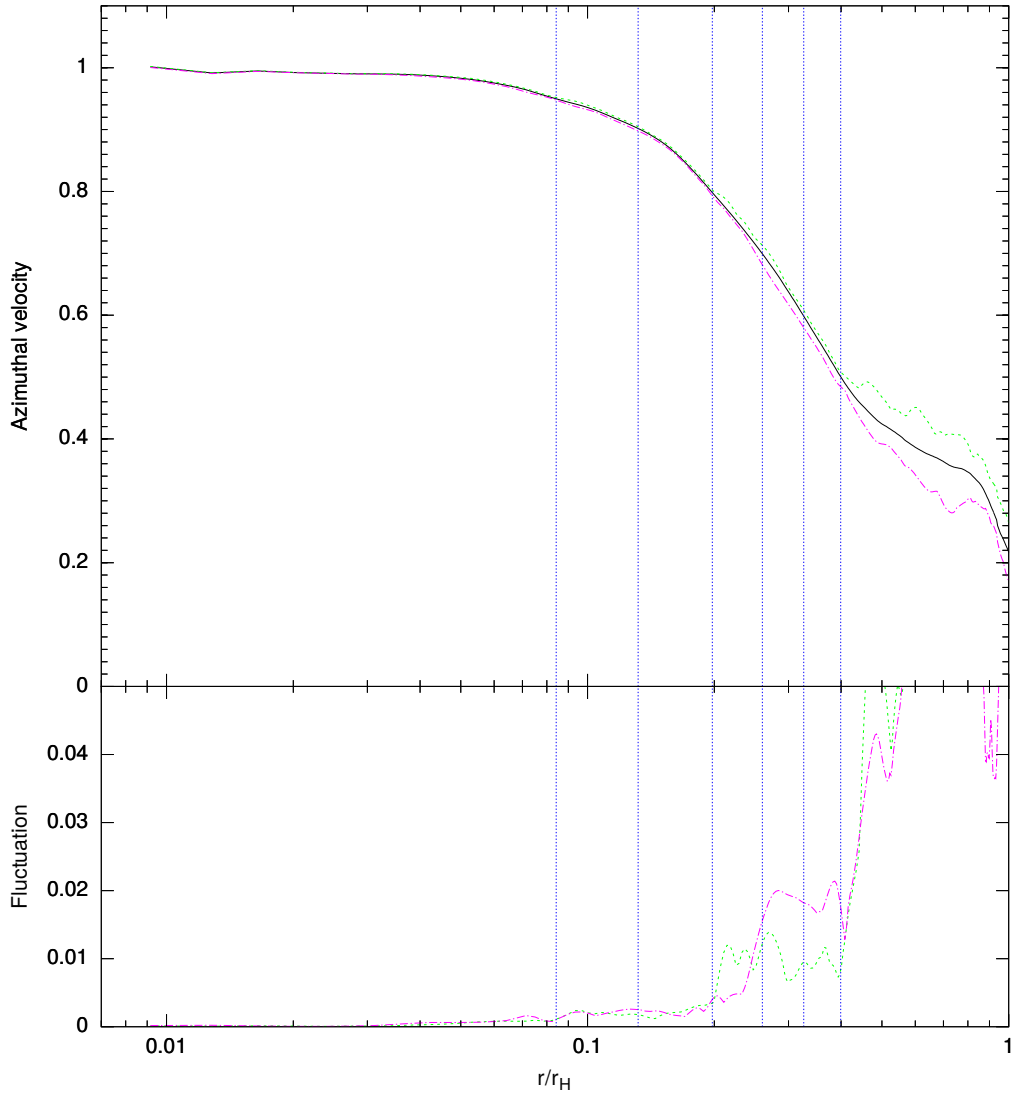

Figure 5.34. Same as in Figure 5.28, but for model with $\hat{r}_{\rm H} = 1.00$.

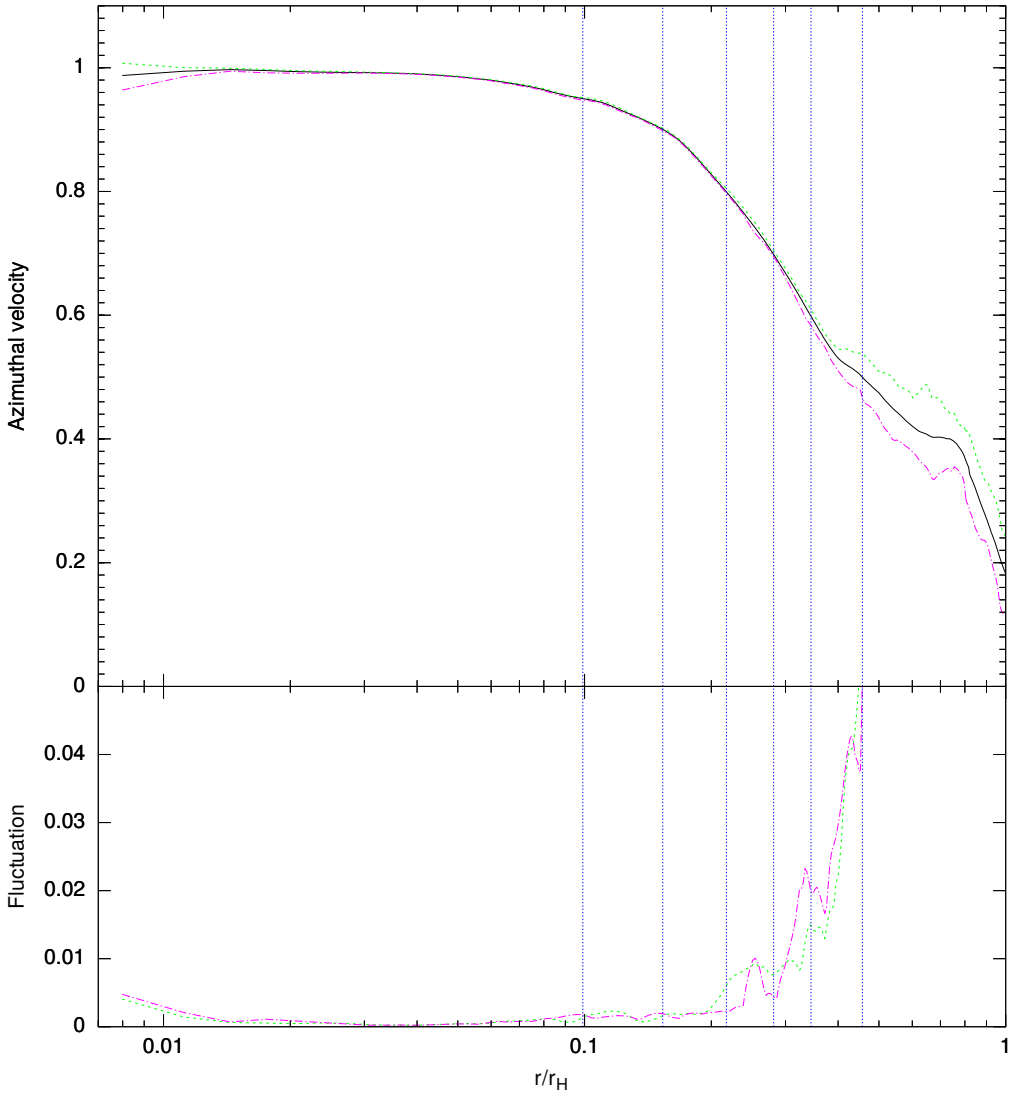

Figure 5.35. Same as in Figure 5.28, but for model with $\hat{r}_{\rm H} = 1.1465$.

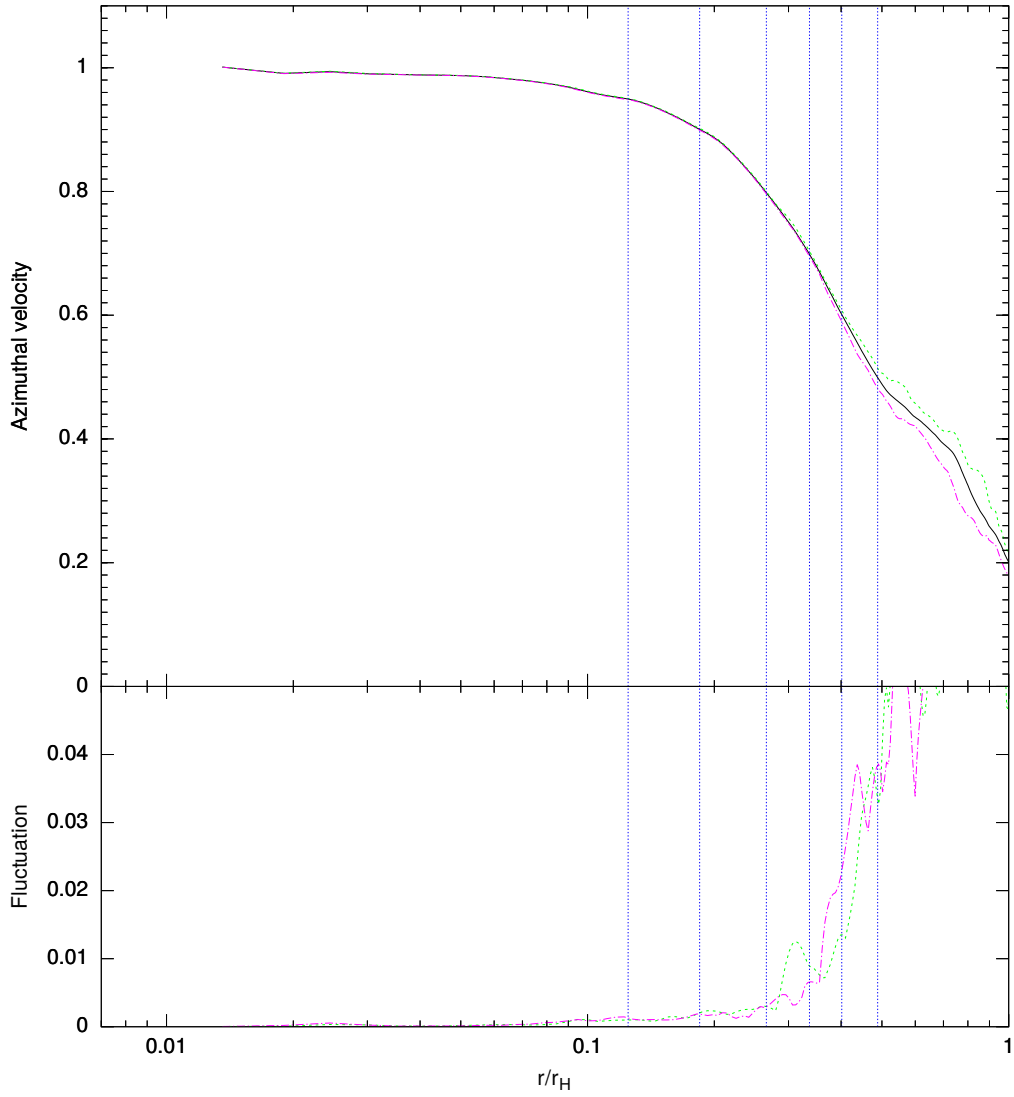

Figure 5.36. Same as in Figure 5.28, but for model with $\hat{r}_{\rm H} = 1.35$.

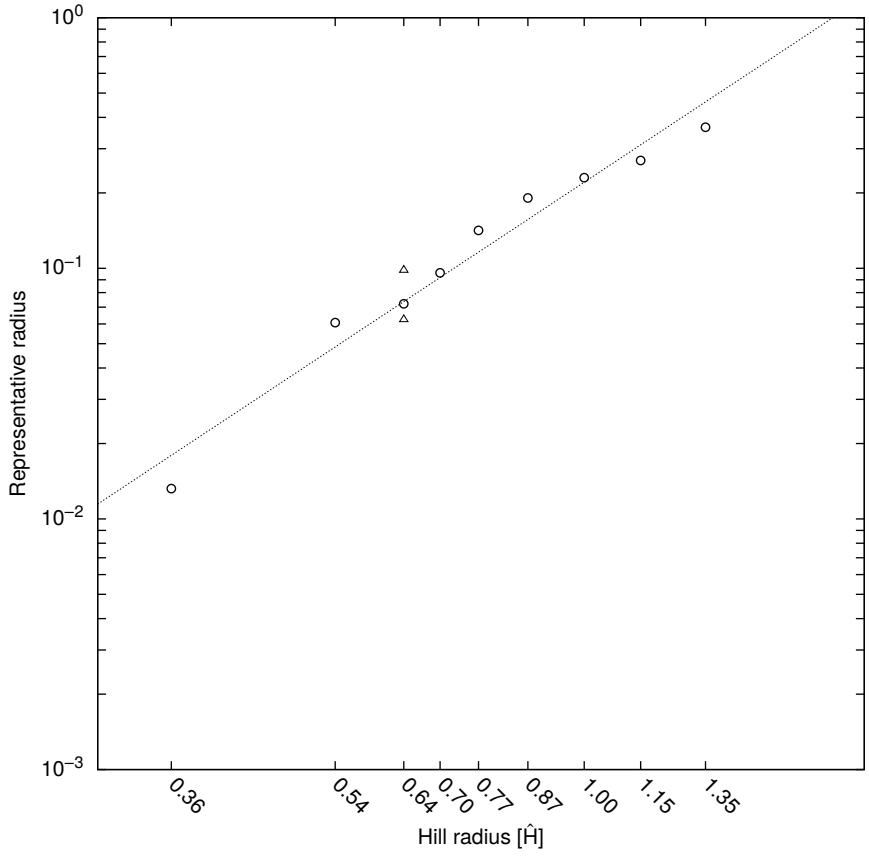

Figure 5.37. Characteristic radius $\hat{r}_{\rm c}$ defined by $\partial L(\hat{r}_{\rm c})/\partial r = 0$ and the approximate power function $0.220601174193696 \times \hat{r}_{\rm H}^{2.456401012428390}$. The circles are for the standard models described in the previous chapter, while the triangles are for the models with different spatial resolutions for models with $\hat{r}_{\rm H} = 0.64$. The higher one corresponds to $l_{\rm max} = 7$ and the lower corresponds to $l_{max} = 9$. The standard model has $l_{\rm max} = 8$.

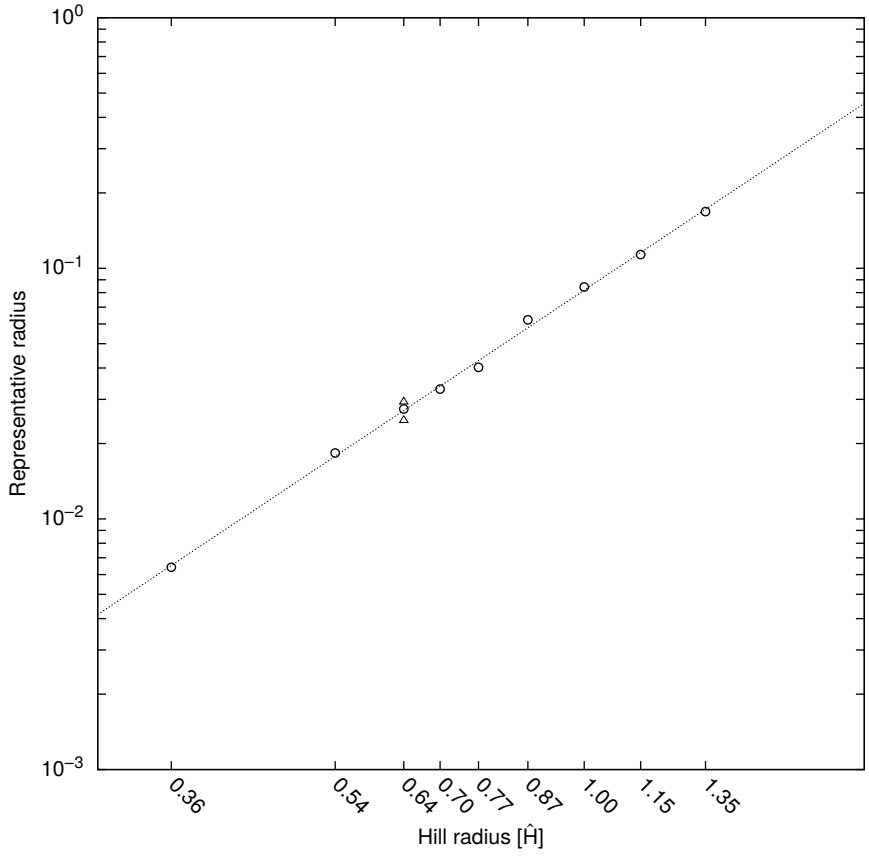

Figure 5.38. Circumplanetary disk radius defined by $v_\theta = 0.95\ v_{\rm Kep}$ and the approximate power function $0.0818096341041719 \times \hat{r}_{\rm H}^{2.47570857114876}$. The velocities are averaged in the azimuthal direction during one Keplerian orbit. The circles are for the standard models shown in the previous chapter, while the triangles are models with different resolutions for $\hat{r}_{\rm H} = 0.64$. The higher one corresponds to $l_{\rm max} = 7$ and the lower corresponds to $l_{\rm max} = 9$. The standard model has $l_{max} = 8$.

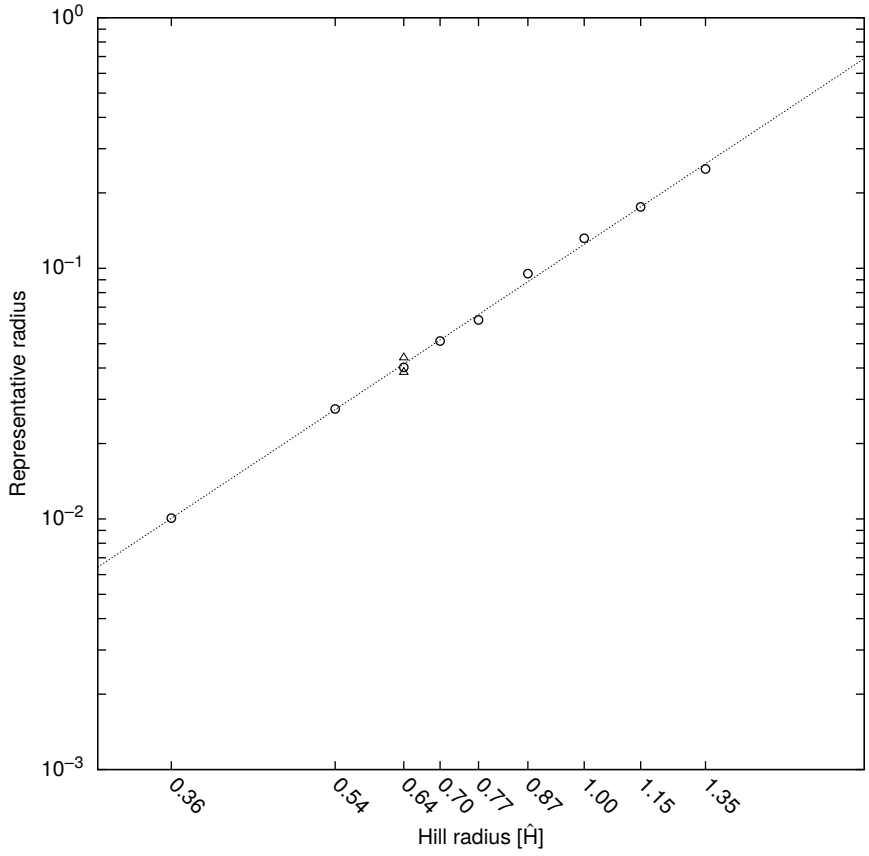

Figure 5.39. Circumplanetary disk radius defined by $v_\theta = 0.90\ v_{\rm Kep}$ and the approximate power function $0.124645062905014 \times \hat{r}_{\rm H}^{2.46384577422025}$. The velocities are averaged in the azimuthal direction during one Keplerian orbit. The circles are for the standard models shown in the previous chapter, while the triangles are models with different resolutions for $\hat{r}_{\rm H} = 0.64$. The higher one corresponds to $l_{\rm max} = 7$ and the lower corresponds to $l_{\rm max} = 9$. The standard model has $l_{max} = 8$.

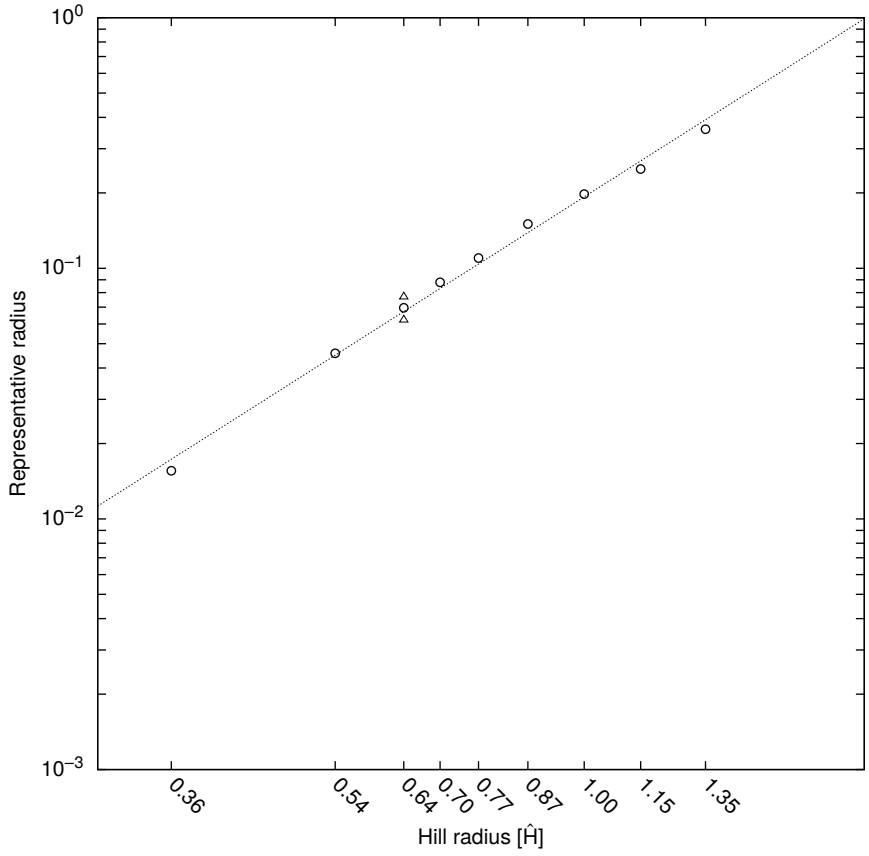

Figure 5.40. Circumplanetary disk radius defined by $v_\theta = 0.80\ v_{\rm Kep}$ and the approximate power function $0.19279764757795 \times \hat{r}_{\rm H}^{2.36023412285795}$. The velocities are averaged in the azimuthal direction during one Keplerian orbit. The circles are for the standard models shown in the previous chapter, while the triangles are models with different resolutions for $\hat{r}_{\rm H} = 0.64$. The higher one corresponds to $l_{\rm max} = 7$ and the lower corresponds to $l_{\rm max} = 9$. The standard model has $l_{max} = 8$.

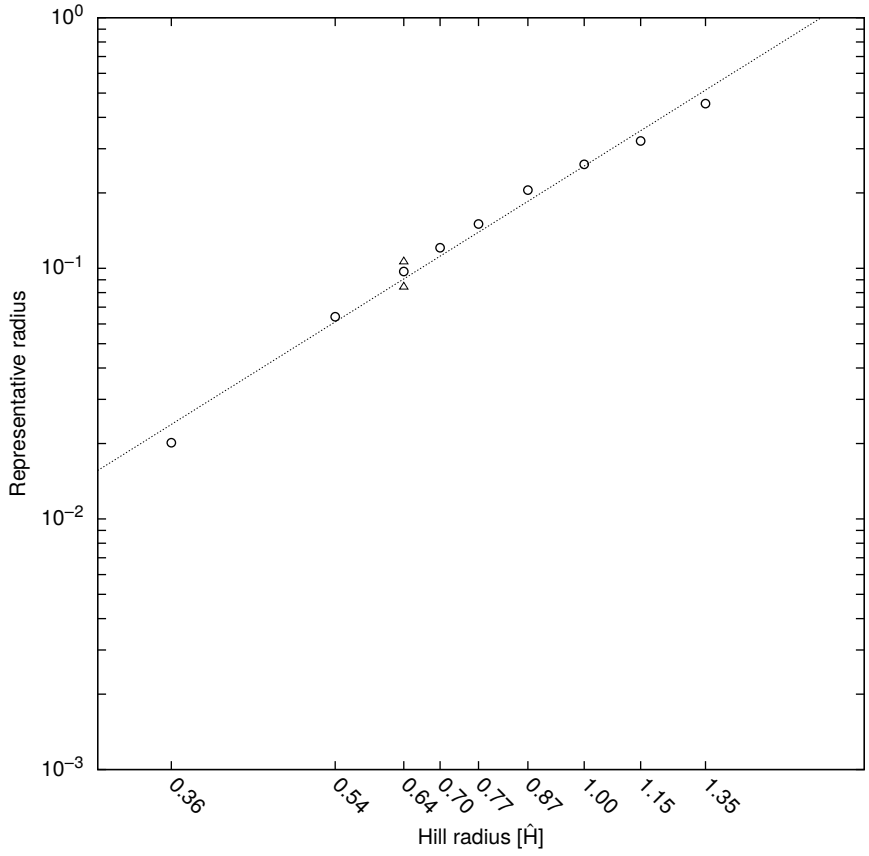

Figure 5.41. Circumplanetary disk radius defined by $v_\theta = 0.70\ v_{\rm Kep}$ and the approximate power function $0.255911907609848 \times \hat{r}_{\rm H}^{2.32377074546421}$. The velocities are averaged in the azimuthal direction during one Keplerian orbit. The circles are for the standard models shown in the previous chapter, while the triangles are models with different resolutions for $\hat{r}_{\rm H} = 0.64$. The higher one corresponds to $l_{\rm max} = 7$ and the lower corresponds to $l_{\rm max} = 9$. The standard model has $l_{max} = 8$.

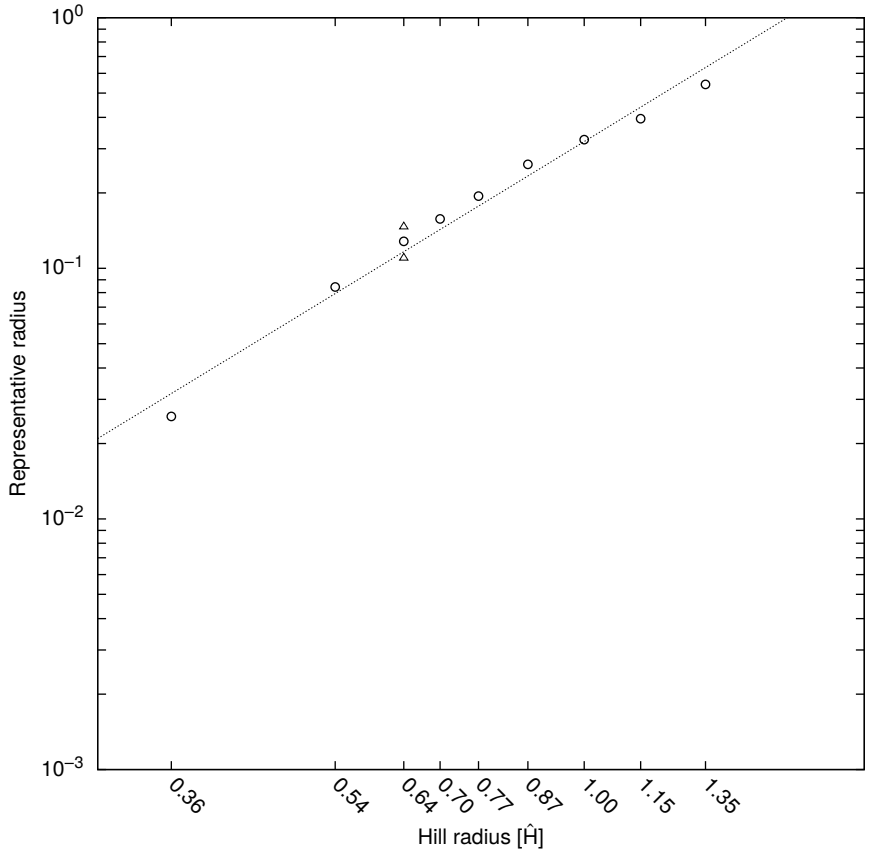

Figure 5.42. Circumplanetary disk radius defined by $v_\theta = 0.60\ v_{\rm Kep}$ and the approximate power function $0.32030581052405 \times \hat{r}_{\rm H}^{2.26593189336104}$. The velocities are averaged in the azimuthal direction during one Keplerian orbit. The circles are for the standard models shown in the previous chapter, while the triangles are models with different resolutions for $\hat{r}_{\rm H} = 0.64$. The higher one corresponds to $l_{\rm max} = 7$ and the lower corresponds to $l_{\rm max} = 9$. The standard model has $l_{max} = 8$.

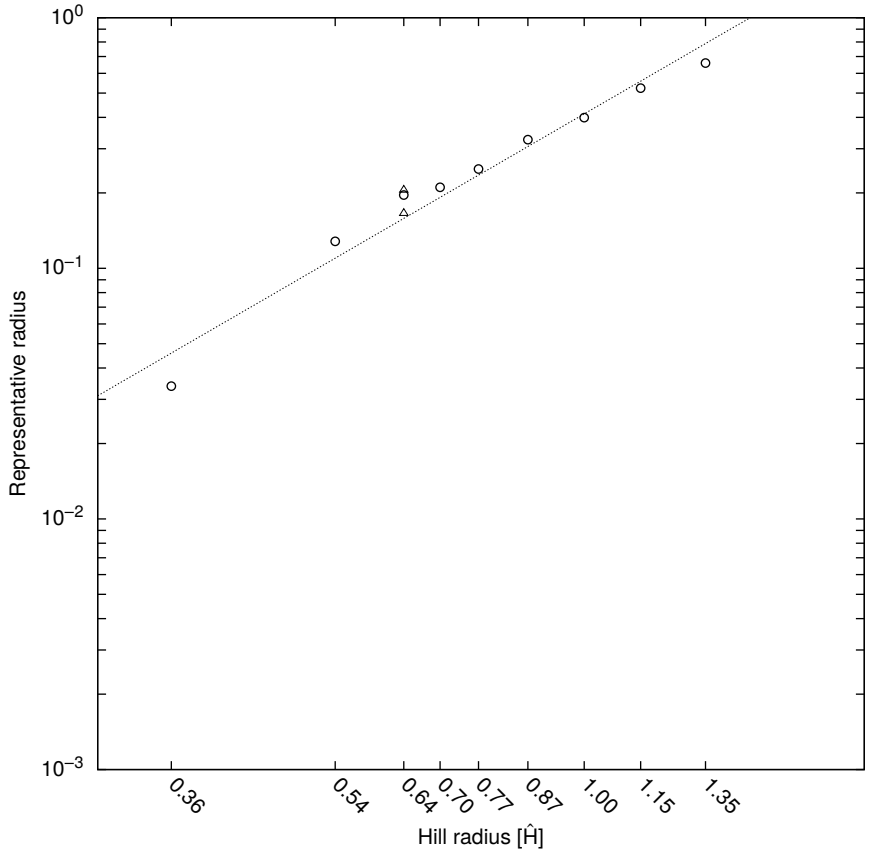

Figure 5.43. Circumplanetary disk radius defined by $v_\theta = 0.50\ v_{\mathrm{Kep}}$ and the approximate power function $0.413212053413054 \times \hat{r}_{\mathrm{H}}^{2.15122957176898}$. The velocities are averaged in the azimuthal direction during one Keplerian orbit. The circles are for the standard models shown in the previous chapter, while the triangles are models with different resolutions for $\hat{r}_{\mathrm{H}} = 0.64$. The higher one corresponds to $l_{\max} = 7$ and the lower corresponds to $l_{\max} = 9$. The standard model has $l_{max} = 8$.

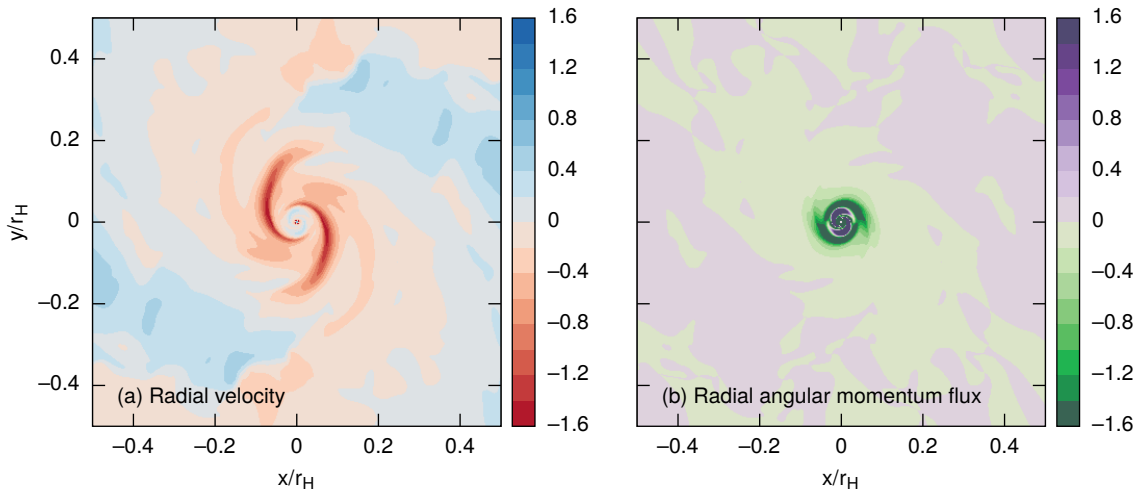

Figure 5.44. Radial velocity (left) and angular momentum advection in the radial direction (right) for model with $\hat{r}_{\rm H} = 0.36$. Gas outflowing and inflowing regions are divided. There exists a boundary from which the disk mass is transferred.

5.4 Radial velocity distributions

As a reference, two-dimensional distribution of the radial velocity and radial angular momentum advection on the mid-plane are shown in Figures 5.44, 5.45 and 5.46 with color. In the figure, we can see clear spirals near the protoplanet. In the outer edge of the spirals in the circumplanetary disk, an interface between outgoing and inflowing flows, which corresponds to the radii shown in Figure 5.37. However, the outer turbulent region varies with time, thus I cannot easily acquire qualitative information from simulation results in the radial velocity profiles.

5.5 Vortex filaments in small Hill radius models

Figure 5.47 shows the vertical velocity component for model with $r_{\rm H}$= 0.64 on the plane of different altitudes. The altitude of panel (a), $z = 0.0037$, corresponds to the lowest cell of the sixth grid. Therefore, compared with other panels, the distribution of velocities are flat, which indicates the gas fluid on the plane does not have a

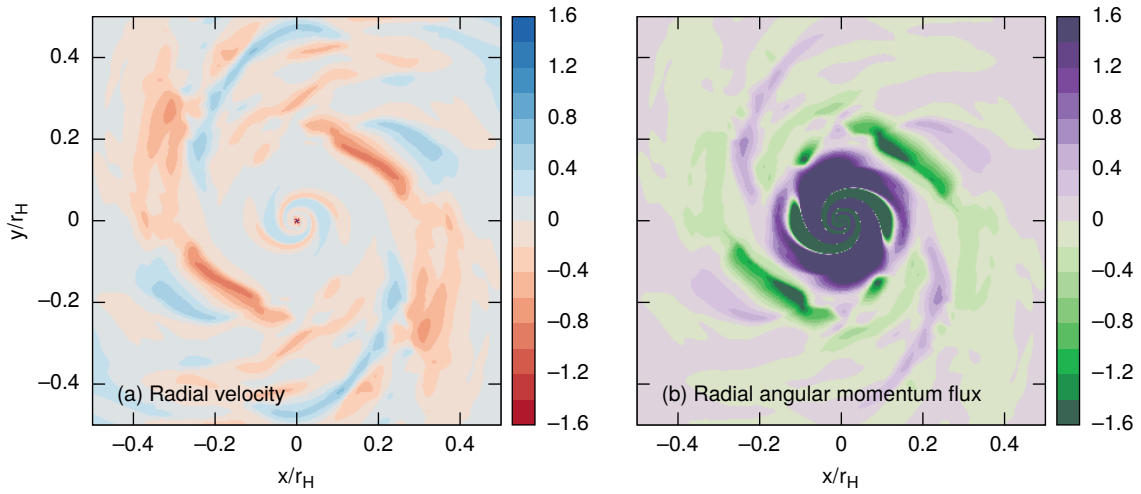

Figure 5.45. Radial velocity (left) and angular momentum advection in the radial direction (right) for model with $\hat{r}_{\rm H} = 0.64$. Gas outgoing velocity fields is confirmed in the disk outer region, and the outgoing velocity region connects to spiral arms. The inflow and outflow are compartmented.

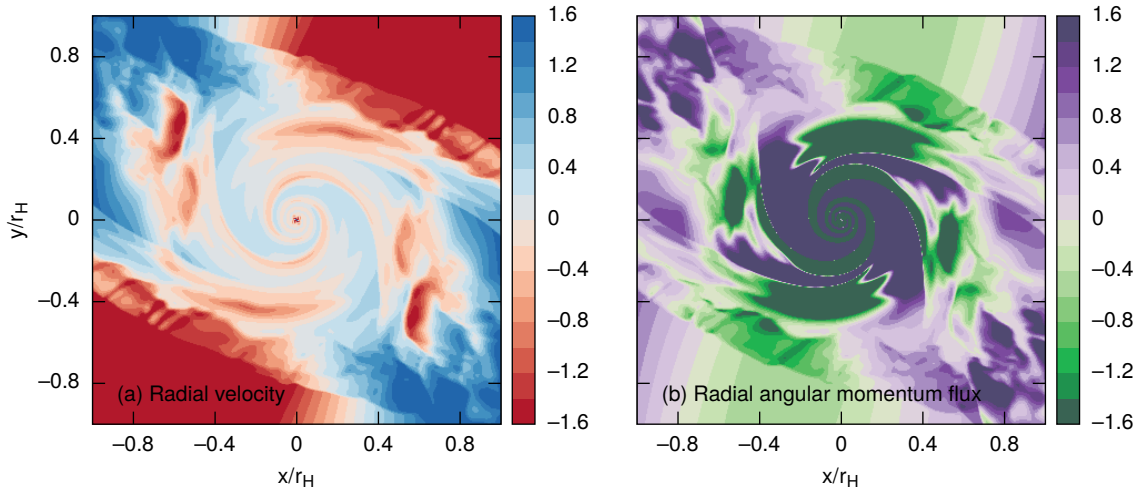

Figure 5.46. Radial velocity (left) and angular momentum advection in the radial direction (right) for model with $\hat{r}_{\rm H} = 1.35$. The disk arm is elongated to near the outer shock surface which is formed by the global flow.

significantly large vertical velocity component in the z-direction.

Around $z = 0.2$, two pairs of positive and negative velocity lines can be observed and are advected toward the directions of circumplanetary disk's shear flow. The lines imply that a vortex tube lies between them. The vortex is clearly seen in Figure 5.48, which shows x–z slices of the density with color and in-plane component of the velocity field with arrows for $y = 0.0, -0.5, -1.0, -5.0$, and -10.0. The vortex is strong, hence it makes the gas density lower than the surrounding environment (Figure 5.48[a]–[c]). However, the vortex diffuses in the region far from the protoplanet and finally disappears.

Source of the vortex tubes is necessarily associated with the meridional circulation around the protoplanet. Figure 5.48(a) indicates that this circulation is generated by the interaction between the shock surface and the outflow from the outer edge of circumplanetary disk. Such circulations are a consequence of gas flow around circumplanetary disk, because such shock surface and outflow generally exist around a protoplanet embedded in the protoplanetary disk. However, the strong vortex is not always formed.

Figure 5.49, which plots a smaller Hill radius model $r_{\rm H} = 0.36$, shows that the same vortex exists slightly inside the Hill region. However, this vortex is weak and the tube-like low density region is not clear. In addition, it dissipates rapidly (Figure 5.49[b]). On the other hand, for a large Hill radius model $r_{\rm H} = 1.15$ (Figure 5.50), a strong meridional circulation is excited, while it's structure is compressed toward the z-direction. Thus, the circulation cannot produce a stable vortex. Among the models, the distance of the circulation center from the protoplanet is approximately equal to $r_{\rm H}$. On the contrary, the shock surfaces are always located in the region much far from the protoplanet, i.e. $x > 1.0$. Note that the shape of shock surfaces for the larger Hill radius models differs from those of the smaller Hill radius models.

These characteristics indicate that flows in the vicinity of planets change qualitatively as the Hill radius increases (or the protoplanet grows), which implies that the mass distributions and the accretion of the angular momentum onto the circumplanetary disk surface rapidly changes according to the increment of the Hill radius or the mass of the protoplanet.

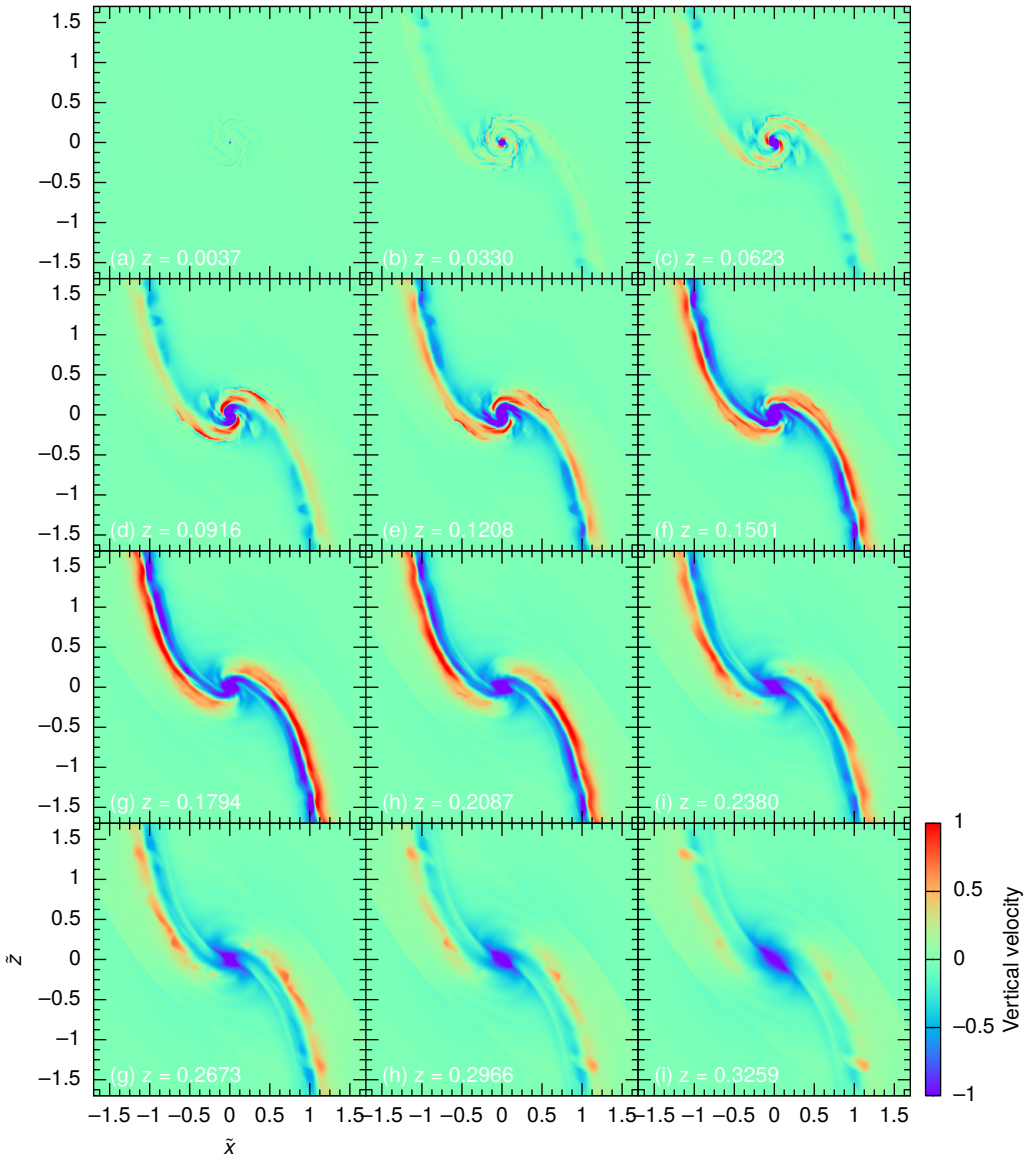

Figure 5.47. Vertical component of gas velocity on the plane of different altitudes for model with r_{H}= 0.64.

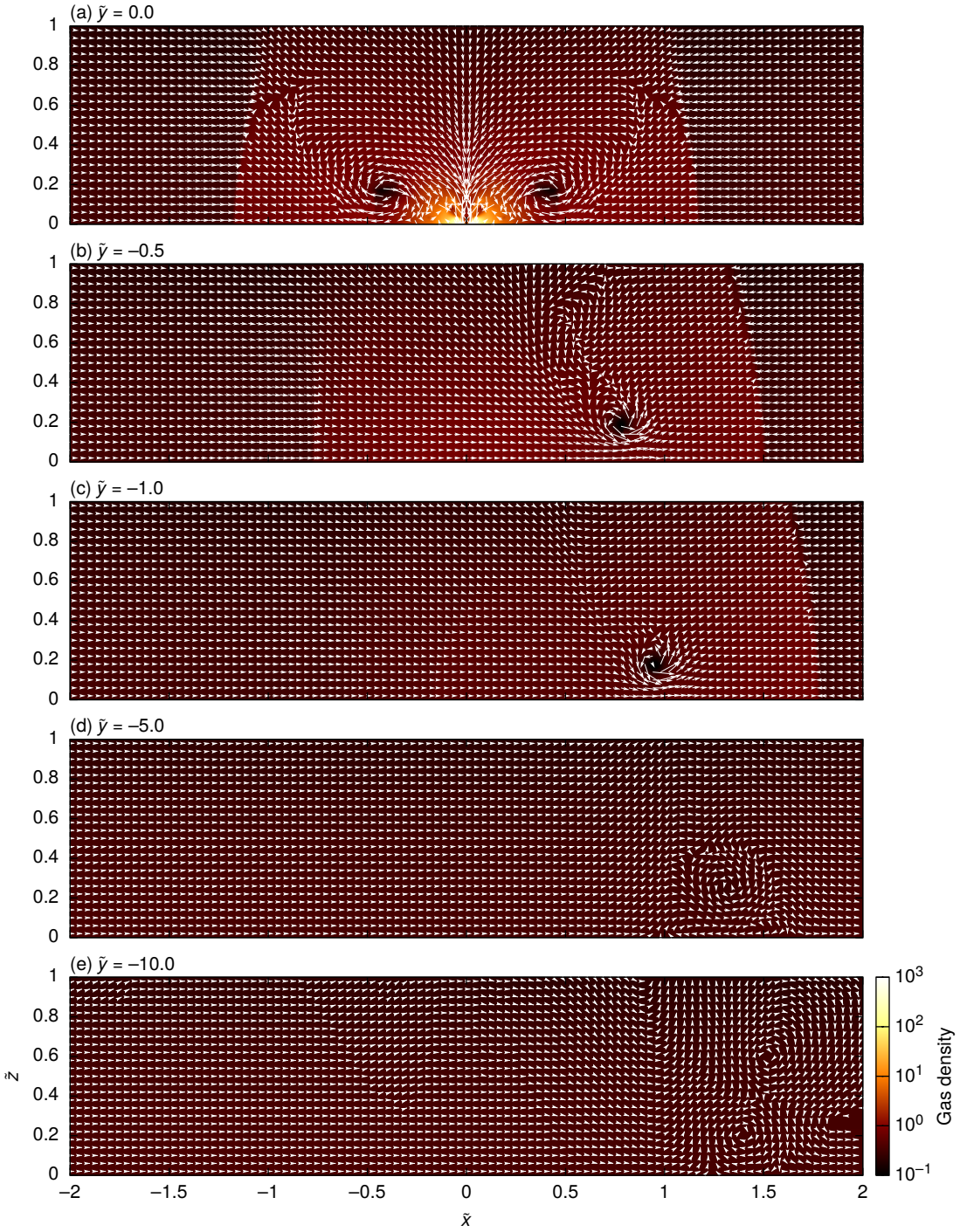

Figure 5.48. The $y = 0.0, -0.5, -1.0, -5.0$, and -10.0 cross section are plotted. Density (color) and velocity (arrows) distributions on the y=constant plane for model with $\hat{r}_{\rm H} = 0.64$

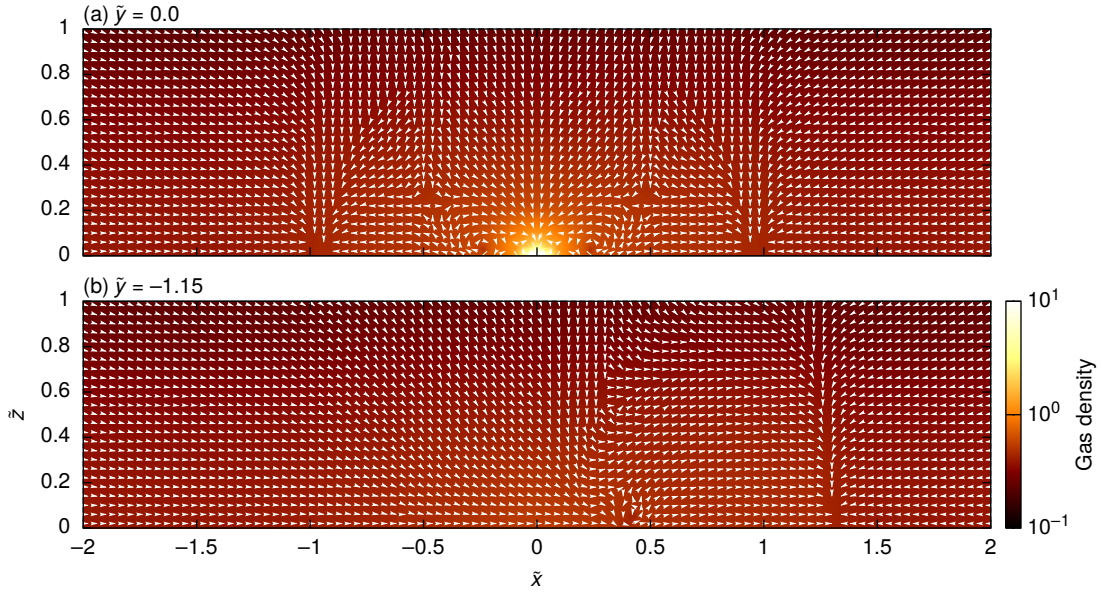

Figure 5.49. The $y = 0.0$ and -0.36 cross section are plotted. Density (color) and velocity (arrows) distributions on the y=constant plane for model with $\hat{r}_{\rm H} = 0.36$

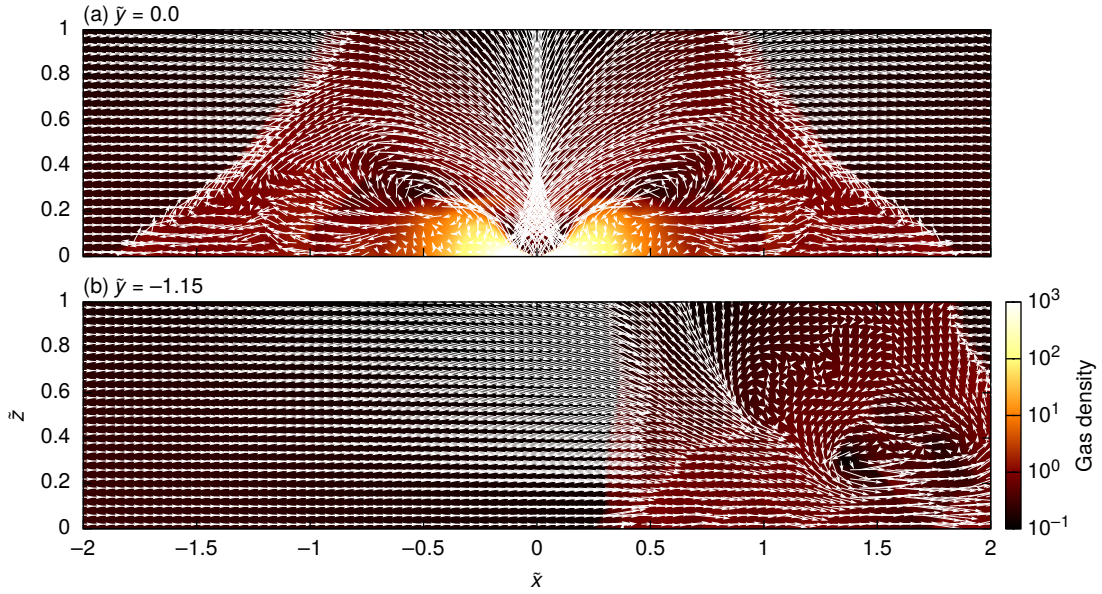

Figure 5.50. The $y = 0.0$ and -1.15 cross section are plotted. Density (color) and velocity (arrows) distributions on the y=constant plane for model with $\hat{r}_{\rm H} = 1.15$

Chapter 6

Summary

Circumplanetary disks are assumed to have important information about an accreting or growing planet and satellite formation. In this study, I performed local three-dimensional hydrodynamic simulations around accreting planet embedded in a protoplanetary disk with a parameter of non-dimensional Hill radius in the range of $\hat{r}_{\rm H} = 0.36$ to 1.35. I adopted an isothermal equation of state to the simulations.

The nested grid method has been used to resolve the structure of the circumplanetary disk, in which the cell width of the finest grid is 2^8 times smaller than that of the root grid. Thus, I could resolve a length comparable to the present Jovian radius. In addition, the finest grid was sufficiently large and includes both the forming circumplanetary disk and the protoplanet itself. Thus, I also could removed boundary effects of the grid in this simulations. I used non-dimensionalized equations and adopted only a single parameter of non-dimensional Hill radius. I defined the origin of local Cartesian coordinate as the position of protoplanet and calculated a quadrant region because of symmetries of the equations. I developed a new sink method to correctly estimate the properties of circumplanetary disk. I imposed two sink cells in the finest grid. I assumed the gas onto the sink cell rapidly accretes onto the protostar, and removed the gas from the computational domain. I also imposed a threshold density of the sink cells, which is dynamically determined every numerical timestep. The greatest merit of the sink method newly adopted in this study is that an equilibrium state is realized inside the Hill radius. Thus, with this method, the distribution of time and azimuthally averaged physical quantities converged near the planet. After the convergence, I can identify the Keplerian rotating circumplanetary

disk formed in the vicinity of the protoplanet and assumed it as a snapshot of forming circumplanetary disk, because the timescale for the converge from initial condition is comparable to an orbital period and is much shorter than the growth timescale of the protoplanet.

In the simulations, after a steady state is accomplished, physical quantities still oscillates with time and their amplitudes depend on the distance from the origin or protoplanet. The density and the surface density strongly oscillate in the inner disk region, and the oscillation may be caused by the treatment of sink cells. However, the amplitudes of oscillation in the averaged specific angular momentum decrease in the inner disk region. The large Hill radius models $\hat{r}_{\rm H} \geq 0.77$ indicate that the stable and unstable (or turbulent) regions are clearly divided and there exists a threshold radius above which the physical quantities strongly oscillates. The threshold radius, which coincides with a weak shock surface, correspond to the outer edge of the circumplanetary disk. This predicts qualitative change of the circumplanetary disk radius as a function of protoplanet's mass, because the threshold radius changes as the Hill parameter varies.

I also investigated the radial dependence of the azimuthal velocity normalized by the Keplerian velocity and found that the radius of circumplanetary disks is approximately proportional to $\hat{r}_{\rm H}^{2.4}$. I estimated the size of the circumplanetary disk using the mass of giant planets in our solar system using the fitting formula derived from this study, and confirmed that my result is consistent with the satellites of Jupiter, Saturn, and Neptune, but is not consistent with those of Uranus. Thus, we may need a special attention to consider the formation of Uranus and its satellite system.

Acknowledgements

Foremost, I wish to thank my supervisor, Associate Professor Shigeo Yoshida, for many supports to perform my researchs and for seminars to my study. I am grateful to Associate Professor Masahiro Machida. He provided me an opportunity to start this research and has been supporting. I am also thankful to Professor Minoru Sekiya for his encouragement and comments. I would also like to thank Assistant Professor Kensuke Nakajima for his continuous encouragement and advice. I also wish to thank my colleagues of Dynamics of the Earth's Interior Group at Kyushu University, and the Professor Masao Nakada.

Bibliography

Ayliffe, B. A. & Bate, M. R., 2009. Circumplanetary disc properties obtained from radiation hydrodynamical simulations of gas accretion by protoplanets, *Monthly Notices of the Royal Astronomical Society*, **397**, 657–665.

Bate, M. R., 1998. Collapse of a Molecular Cloud Core to Stellar Densities: The First Three-dimensional Calculations, *The Astrophysical Journal Letters*, **508**, L95–L98.

Casassus, S., Marino, S., Pérez, S., Roman, P., Dunhill, A., Armitage, P. J., Cuadra, J., Wootten, A., van der Plas, G., Cieza, L., Moral, V., Christiaens, V., & Montesinos, M., 2015. Accretion Kinematics through the Warped Transition Disk in HD142527 from Resolved CO(6-5) Observations, *The Astrophysical Journal*, **811**, 92.

Caselli, P., Walmsley, C. M., Zucconi, A., Tafalla, M., Dore, L., & Myers, P. C., 2002. Molecular Ions in L1544. I. Kinematics, *The Astrophysical Journal*, **565**, 331–343.

D'Angelo, G., Henning, T., & Kley, W., 2003. Thermohydrodynamics of Circumstellar Disks with High-Mass Planets, *The Astrophysical Journal*, **599**, 548–576.

Fukagawa, M., Hayashi, M., Tamura, M., Itoh, Y., Hayashi, S. S., Oasa, Y., Takeuchi, T., Morino, J.-i., Murakawa, K., Oya, S., Yamashita, T., Suto, H., Mayama, S., Naoi, T., Ishii, M., Pyo, T.-S., Nishikawa, T., Takato, N., Usuda, T., Ando, H., Iye, M., Miyama, S. M., & Kaifu, N., 2004. Spiral Structure in the Circumstellar Disk around AB Aurigae, *The Astrophysical Journal Letters*, **605**, L53–L56.

Gressel, O., Nelson, R. P., Turner, N. J., & Ziegler, U., 2013. Global hydromagnetic simulations of a planet embedded in a dead zone: Gap opening, gas accretion, and formation of a protoplanetary jet, *The Astrophysical Journal*, **779**(1), 59.

Ikoma, M., Nakazawa, K., & Emori, H., 2000. Formation of Giant Planets: Dependences on Core Accretion Rate and Grain Opacity, *The Astrophysical Journal*, **537**,

1013–1025.

Kley, W., D'Angelo, G., & Henning, T., 2001. Three-dimensional Simulations of a Planet Embedded in a Protoplanetary Disk, *The Astrophysical Journal*, **547**, 457–464.

Larson, R. B., 1969. Numerical calculations of the dynamics of collapsing proto-star, *Monthly Notices of the Royal Astronomical Society*, **145**, 271.

Lubow, S. H., Seibert, M., & Artymowicz, P., 1999. Disk Accretion onto High-Mass Planets, *The Astrophysical Journal*, **526**, 1001–1012.

Machida, M. N., 2009. Thermal effects of circumplanetary disc formation around proto-gas giant planets, *Monthly Notices of the Royal Astronomical Society*, **392**(2), 514–524.

Machida, M. N., Kokubo, E., Inutsuka, S. I., & Matsumoto, T., 2008. Angular momentum accretion onto a gas giant planet, *Astrophysical Journal*, **685**(2), 1220–1236.

Machida, M. N., Kokubo, E., Inutsuka, S.-i., & Matsumoto, T., 2010. Gas accretion onto a protoplanet and formation of a gas giant planet, *Monthly Notices of the Royal Astronomical Society*.

Masunaga, H. & Inutsuka, S.-i., 2000. A Radiation Hydrodynamic Model for Protostellar Collapse. II. The Second Collapse and the Birth of a Protostar, *The Astrophysical Journal*, **531**, 350–365.

Matsumoto, T. & Hanawa, T., 2003. Fragmentation of a molecular cloud core versus fragmentation of the massive protoplanetary disk in the main accretion phase, *Astrophysical Journal*, **595**(2), 913–934.

Miyoshi, K., Takeuchi, T., Tanaka, H., & Ida, S., 1999. Gravitational interaction between a protoplanet and a protoplanetary disk. i. local three-dimensional simulations, *Astrophysical Journal*, **516**(1), 451–464.

Mizuno, H., 1980. Formation of the giant planets, *Progress of Theoretical Physics*, **64**(2), 544–557.

Mizuno, H., Nakazawa, K., & Hayashi, C., 1978. Instability of a gaseous envelope surrounding a planetary core and formation of giant planets, *Progress of Theoretical Physics*, **60**(3), 699–710.

Morbidelli, A., SzulÃągyi, J., Crida, A., Lega, E., Bitsch, B., Tanigawa, T., & Kanagawa, K., 2014. Meridional circulation of gas into gaps opened by giant planets in

three-dimensional low-viscosity disks, *Icarus*, **232**, 266–270.

Roe, P. L., 1981. Approximate riemann solvers, parameter vectors, and difference-schemes, *Journal of Computational Physics*, **43**(2), 357–372.

Sallum, S., Follette, K. B., Eisner, J. A., Close, L. M., Hinz, P., Kratter, K., Males, J., Skemer, A., Macintosh, B., Tuthill, P., Bailey, V., Defrère, D., Morzinski, K., Rodigas, T., Spalding, E., Vaz, A., & Weinberger, A. J., 2015. Accreting protoplanets in the LkCa 15 transition disk, *Nature*, **527**, 342–344.

Szulágyi, J., 2017. Effects of the planetary temperature on the circumplanetary disk and on the gap, *The Astrophysical Journal*, **842**(2), 103.

Tanigawa, T. & Watanabe, S.-i., 2002. Gas Accretion Flows onto Giant Protoplanets: High-Resolution Two-dimensional Simulations, *The Astrophysical Journal*, **580**, 506–518.

Tanigawa, T., Ohtsuki, K., & Machida, M. N., 2012. Distribution of accreting gas and angular momentum onto circumplanetary disks, *The Astrophysical Journal*, **747**(1), 47.

Toomre, A., 1964. On the gravitational stability of a disk of stars, *The Astrophysical Journal*, **139**, 1217–1238.